ELECTRICAL AND OPTICAL PROPERTIES OF SPUTTERED pCdTe-nCdSe HETEROJUNCTIONS

by

KOK WAI CHEAH

A thesis submitted for the

Degree of Doctor of Philosophy

in the University of London

Department of Electrical Engineering

Imperial College of Science and Technology

London, SW7

Acknowledgement

I would like to thank Dr. D.W.G. Ballentyne very much for his supervision and invaluable advice. I am also grateful to Professor J.C. Anderson in instrumenting the financial assistance of the Clothworkers' Bursary to whom I am also indebted. Many thanks to Mr. S. Kimmins in making his T.S.C. equipment available and assisting throughout the experiments. Also my gratitude to all those on levels 7 and 3 of the Electrical Engineering department who have assisted me during the course of the research.

Finally, my thanks are also due to Miss C.D.M. Collins for typing this thesis.

ABSTRACT

The electrical and optical properties of pCdTe-nCdSe heterojunction fabricated by sputtering were investigated. The primary aim of the work was to find out if it was feasible to make a double thin film heterojunction solar cell. It was found, however, that the junction characteristic is dominated by interface states. Tunnelling through the junction barrier is found to be the factor limiting the current and the junction capacitance has a complex dependent of frequency with a low pass filter characteristic. In general, theoretical predictions agree reasonably well with the experimental results. From the scanning electron micrograph, columnar crystallites are observed showing very few grain boundaries transversing the paths of the carriers. This structure implies that grain boundary effects are not significant and no such effects are experimentally observed. The photovoltage is low due to the tunnelling current, hence the heterojunction solar cell is not likely to be competitive with commercially available solar cells in its present form. In order to increase the photovoltage the interface state density must be reduced and the trapped charge significantly reduced in the interface region.

CONTENTS

		Page No.
Acknowledgements		2
Abstract		3
List of Principal Symbols		7
CHAPTER 1:	INTRODUCTION	9
1.1	HISTORICAL SURVEY OF HETEROJUNCTION DEVICES	9
1.2	APPLICATIONS OF HETEROJUNCTIONS	9
1.3	BRIEF SURVEY OF THE PHYSICAL PROPERTIES OF HETEROJUNCTIONS	11
1.3.1	Abrupt Heterojunctions	11
1.3.2	Graded Heterojunctions	17
1.4	AIMS	17
CHAPTER 2:	HETEROJUNCTION THEORY	19
2.1	DEFINITION	19
2.2	p-n ANISOTYPE HETEROJUNCTION THEORY - ANDERSON'S THEORY	20
2.3	THE EFFECT OF INTERFACE STATES ON THE CHARACTERISTICS OF HETEROJUNCTIONS	23
2.3.1	The Origin of Interface States	23
2.3.2	Space Charge Region at the Interface	26
2.3.3	Junction Capacitance	36
2.3.4	The A.C. Field Effect	40
2.3.5	Transport Mechanisms	45

		Page No.
2.4	THE THIN FILM HETEROJUNCTION	51
	2.4.1 Thin Film Effect	51
	2.4.2 Junction Characteristic of Thin Film Heterojunctions	57
2.5	SUMMARY	60
CHAPTER 3:	SPUTTERING AND SPUTTERED FILMS	61
3.1	DEFINITION	61
3.2	HISTORICAL REVIEW	61
3.3	THEORY OF SPUTTERING	62
3.4	SPUTTERING CONDITION	63
3.5	DEPOSITION RATE	66
3.6	R.F. SPUTTERING	67
3.7	SPUTTERED FILMS	67
	3.7.1 Adhesion of Sputtered Films	67
	3.7.2 Contamination of the Sputtered Films	68
	3.7.3 Properties of Sputtered Films	69
CHAPTER 4:	PROPERTIES OF CADMIUM TELLURIDE AND CADMIUM SELENIDE - RESUME	71
4.1	CRYSTAL STRUCTURES	71
	4.1.1 Cadmium Telluride	71
	4.1.2 Cadmium Selenide	73
4.2	ELECTRICAL AND OPTICAL PROPERTIES	75
	4.2.1 Cadmium Telluride	75
	4.2.2 Cadmium Selenide	77

		Page No.
4.3	THIN FILM CADMIUM TELLURIDE AND CADMIUM SELENIDE	77
	4.3.1 Cadmium Telluride	78
	4.3.2 Cadmium Selenide	78
4.4	pCdTe-nCdSe HETEROJUNCTIONS	81
CHAPTER 5:	EXPERIMENTAL PROCEDURES AND DEVICE FABRICATION	84
5.1	PREPARATION PROCEDURE	
	5.1.1 Sputtering System	84
	5.1.2 Sputtering Procedure	86
	5.1.3 Substrate and Contacts	86
5.2	EXPERIMENTAL PROCEDURE	88
	5.2.1 Current-Voltage Measurement	88
	5.2.2 Capacitance Measurement	90
	5.2.3 Photovoltaic Measurement	90
	5.2.4 Thermally Stimulated Current Measurement	91
CHAPTER 6:	RESULTS AND DISCUSSION	94
6.1	ELECTRICAL RESULTS	94
	6.1.1 D.C. Current-Voltage Results	94
	6.1.2 A.C. Current-Voltage Results	103
	6.1.3 Capacitance-Frequency Measurement Results	111
6.2	PHOTOVOLTAIC RESULTS	114
6.3	THERMALLY STIMULATED CURRENT RESULTS	128
6.4	MICROSTRUCTURE OF THE HETEROJUNCTION FILM	137
6.5	DISCUSSION	137
CHAPTER 7:	CONCLUSIONS	148
References		152

LIST OF PRINCIPAL SYMBOLS

a	area of device
C	capacitance
E_c	conduction band edge (lower)
E_v	valence band edge (top)
ΔE_c	difference in conduction band edge energies
ΔE_v	difference in valence band edge energies
E_F	Fermi energy level of a semiconductor
E_t	energy level of the trap below (above) the conduction (valence) band edge
E_g	energy band gap
e	electron)
h	hole)) also used as asubscript with the same meaning
$\hbar$	Planck's constant, $h/2\pi$
I	current
J	current density
k	Boltzmann constant
L_D	Debye (diffusion) length
m	rest mass of carrier
m^*	effective mass of carrier
n_o	intrinsic electron concentration in a semiconductor
n_b	electron concentration in an n-type semiconductor
N_D	donor concentration in a semiconductor
N_A	acceptor concentration in a semiconductor
N_t	trap density in a semiconductor

F	electric field
p_b	hole concentration of a p-type semiconductor
q	electric charge of a carrier (electron or hole)
T	temperature
Q	total charge
Z	impedance
W	Junction width
V	voltage
V_a	applied voltage
V_D	built-in voltage
ε_o	relative dielectric permittivity of free space
ε	dielectric constant
λ	lattice constant
μ	the mobility of a carrier (electron or hole)
ω	frequency
ν_{th}	thermal electronic velocity
ϕ	work function of a semiconductor
χ	electron affinity of a semiconductor
ψ	dimensionless potential
$\bar{\varepsilon}$	dimensionless field
ρ	charge density
ϕ_m	electric dipole

Subscripts

1,2	denote wide-gap and narrow-gap semiconductors, respectively
o	denotes the interface
a	applied voltage

CHAPTER 1

INTRODUCTION

1.1 HISTORICAL SURVEY ON HETEROJUNCTION DEVICES

Active research on heterojunctions increased markedly in 1956 when Kroemer suggested the possibility of an isotype heterojunction exhibiting high injection efficiency. In the following years GaAs-Ge heterojunctions became the most widely investigated (Milnes and Feucht, 1972). II-VI compound heterojunctions were not investigated until 1970 in this laboratory (Private Communication 1970). The work was initiated both from an interest in the fundamental structure of II-VI heterojunctions and also to assess their potential for application in solar cells.

1.2 APPLICATION OF HETEROJUNCTIONS

Heterojunctions are found mainly in two types of applications utilising (a) their electrical characteristics or (b) their optoelectronic properties. Due to the difference in the electron affinities of the two materials forming the heterojunction, potential barriers are formed both in conduction and valence bands. This property enabled the heterojunction to be used in case (a) in the isotype heterojunction, as a unidirectional emitter or a high speed rectifier; whilst anisotype junction has been used as the emitter-base junction of a transistor (Tansley, 1971).

Difference in band gap also gives rise to the so-called window effect when the junction is illuminated with light. The effect arises due to the fact that low* energy photons incident normally onto the heterojunction surface pass through the junction region unabsorbed, whereas high† energy photons are absorbed on the surface and subsequently recombine without contributing to the photocurrent. Thus,photons with energies within the band gaps of the heterojunction are absorbed at the interface where the existing electrostatic field separates the electron-hole pairs generated. Practically, the window effect can be applied in case (b) as it allows heterojunctions to be used as band-pass filter photodetectors, and solar cells. (Tansley, 1971).

The success of these applications, however, is not altogether inspiring, because the problem of traps and recombination at the interface are unpredictable. Also, the polycrystalline nature of the materials, when thin films are used, complicates the problem still further and affects the consistency of the properties of fabricated junctions, a problem when they are to be made commercially. Also this unpredictability in the properties of practical junctions has lead to heterojunction theories, which fail to describe the heterojunction behaviour with any degree of precision.

---

*low here implied photon energy lower than the heterojunction band gaps

†high here implied photon energy higher than the heterojunction band gaps.

1.3 BRIEF SURVEY OF THE PHYSICAL PROPERTIES OF HETEROJUNCTIONS

1.3.1 Abrupt Heterojunctions

The detailed theory of the abrupt heterojunction was proposed in 1960 by Anderson and his approach still forms the basis of much present day thought on the subject. Major modifications include tunnelling and recombination through traps (Dolega 1963, Riben and Feucht, 1966a and 1966b).

Anderson's model (Milnes and Feucht, 1972) is an extension of the theory which has been applied for decades in the p-n homojunction, modified by the fact that the junction is formed by two different materials. Anderson (1960) has tried to overcome the problem of the interface by introducing a transmission coefficient, X, in the current-voltage relation:

$$I = A \exp\left[- q V_{A2}/kT\right] \left[\exp(q V_2/kT) - \exp(-qV_1/kT)\right] \qquad (1.1)$$

where

$$A = X\, a\, qN_{A2}\, (D_p/\tau_p)^{\frac{1}{2}}$$

and

D_p = diffusion constant

τ_p = life time of the carrier

However, this transmission coefficient X is an empirical constant. The theory has also neglected the effect of interface states, and assumed the dominant transport mechanism is of a thermal emission type (see fig. 1.1a).

Fig. 1.1a to b shows six possible transport mechanisms in anisotype (n-p) heterojunction. Fig. 1.1a is the emission model used by Anderson (1960). Here Perlman and Feucht (1966) have included the formation of spike barrier and notch by using the Schottky emission method. However, the magnitude of current predicted by this model is still too small and their approach is unable to describe the current-voltage characteristic satisfactorily. Fig. 1.1b gives a model proposed by Redikel et al. (1964) where holes tunnelled through the spike from the valence band of the wide band gap material into the valence band of the narrow band gap semiconductor. Unfortunately, the predictions of the model failed to agree with experimental results generally obtained. Fig. 1.1c is the recombination model discussed by Dolega (1963). Another tunnelling model was proposed by Riben and Feucht (1966) (Fig. 1.1d) suggesting that the transport mechanism in the heterojunction was dominated by a non-thermal current. Fig. 1.1e and f show models relying on a mechanism combining a mixture of tunnelling-recombination for the transport mechanism which was proposed by Donnely and Milne (1966). This model is more complex than other models which depend on interface state density. The last model reflects the complexity of the transport properties of heterojunctions in general, making the interpretation experimental results very difficult.

In isotype heterojunctions (n-n, p-p), only majority carriers are involved and both the n-n and p-p heterojunctions can act as rectifiers (figs. 1.2). The

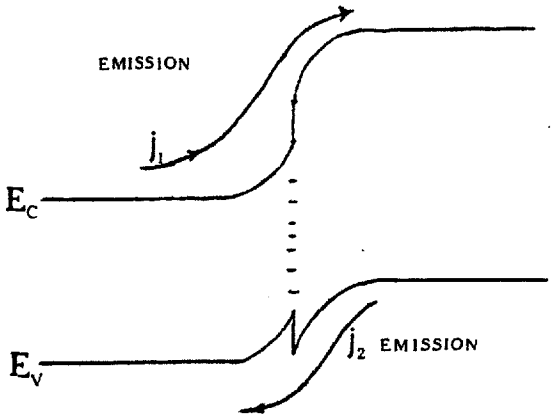

(a)

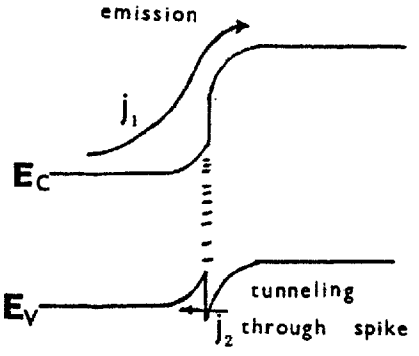

(b)

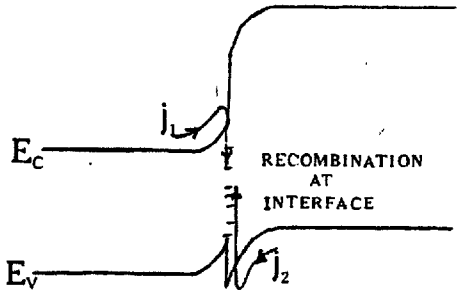

(c)

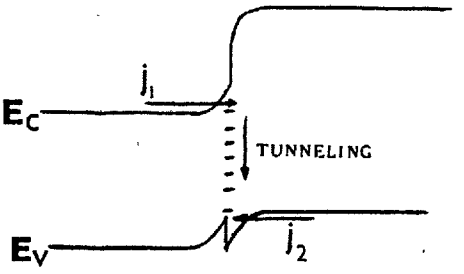

(d)

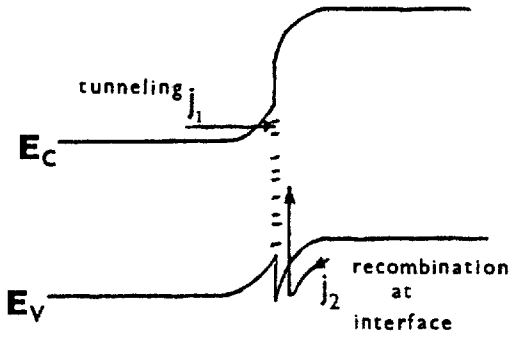

(e)

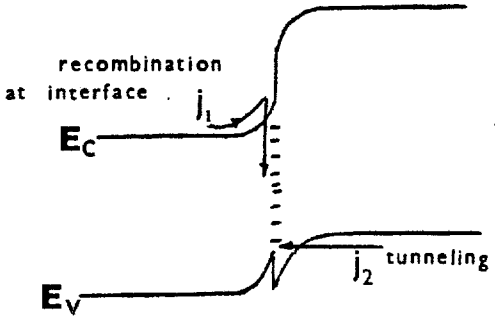

(f)

Fig. 1.1: Models of n-p Anisotropic Heterojunction (Milnes and Feucht, 1972)

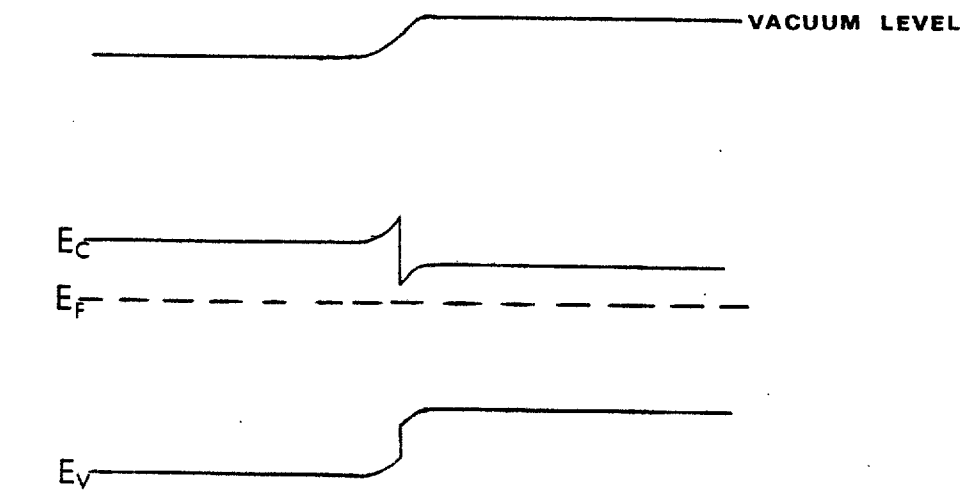

(a)

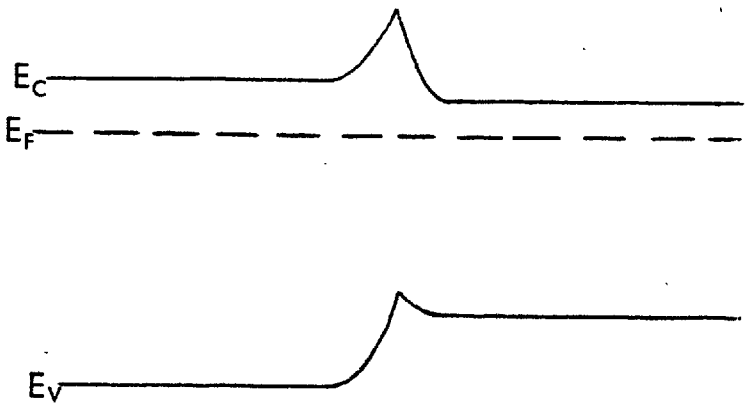

(b)

Fig. 1.2: (a) Energy Band Diagram of n-n Ge-Si Heterojunction
(b) One Possible Effect of Interface States on (a). (Milnes and Feucht, 1972)

existence of the interface states, however, can affect the space charge characteristics at the interface (fig. 1.2b). In the case of negligible interface states, Anderson's model can be applied (fig. 1.2a). However, a high density of interface states can change the polarity of the space charge. This occurs for example in the Ge-Si n-n heterojunction which with sufficient interface states behaves like a back-to-back Schottky diode (Oldham and Milne, 1964; Van Opdorp, 1969). A kinetic approach to a solution of the back-to-back Schottky diode model has been presented by Oldham and Milne (1964). The model assumed the interface states to be present as a thin layer sandwiched between the two depletion regions (fig. 1.3), both tunneling and image effects are neglected. Their analysis led to a double saturation characteristic, as was observed practically in numerous isotype hetero-junctions. However, this theory was not so successful in explaining the properties of other fabricated junctions and the discrepancies between theory and experiments are believed to be due to the tunnelling and image effects ignored in this theory (Hipwood, 1977). A dipole model was proposed by Van Ruyven (1964) where a dipole is formed at the interface. The model is similar to the model just described,

Both isotype and anisotype heterojunctions are affected by interface states, making consistent correspondence between any experimental observations and theoretical predictions very difficult to explain in a general way. As, however, isotype heterojunctions exhibit no minority carrier diffusion/injection or recombination process which occur in anisotype heterojunction, the effect of the interface states would be different from the anisotype heterojunction.

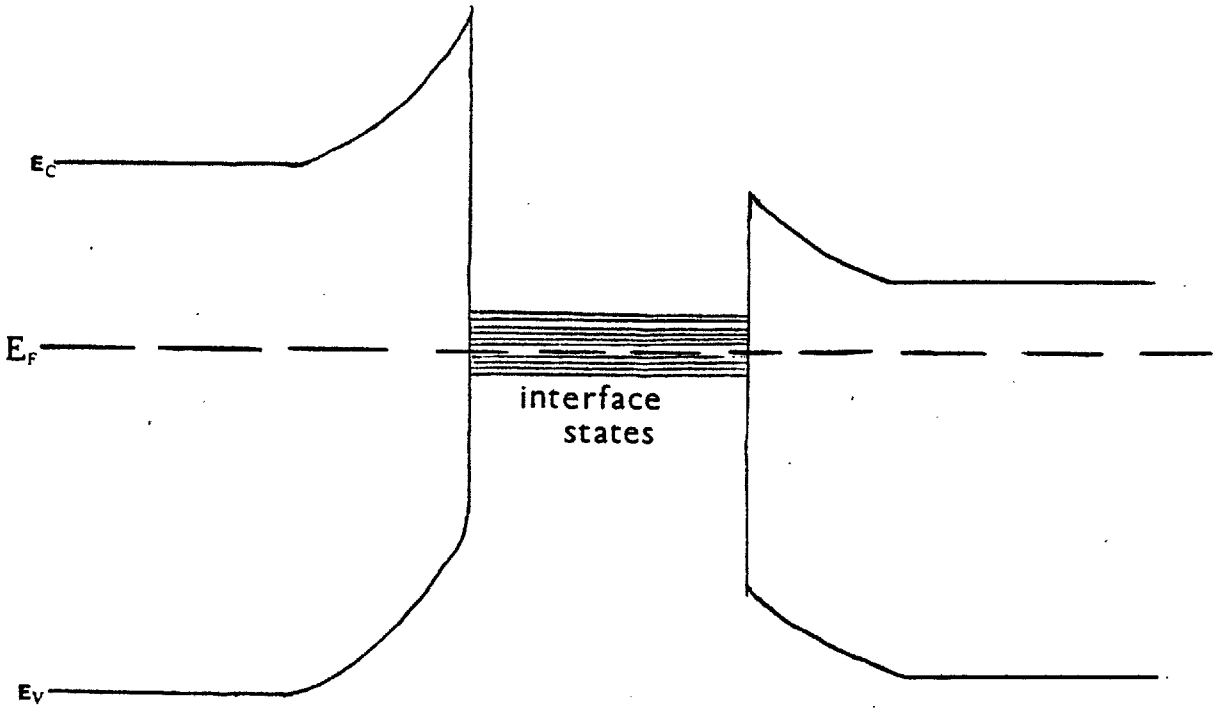

Fig. 1.3: Kinetic Treatment of n-n Heterojunction with Interface States (after Oldham and Milnes, 1964)

1.3.2 Graded Heterojunctions

Graded heterojunctions have some special properties in the transition region where, in the absence of a real metallurgical interface, all the essential parameters become a function of position. For example, position-dependent changes of electron affinity and band gap cause band bending due partly to built-in electrostatic field and partly to the grading of the band structure (Van Ruyven, 1972).

Kroemer (1957) was the first to present a graded heterojunction model. Other workers like Van Ruyven and Williams (1967) have developed the theory further.

1.4 AIMS

Investigation of pCdTe-nCdSe heterojunction as a possible solar cell began in this laboratory with Sadek (1975) who sputtered nCdSe onto single crystal pCdTe substrates. The results showed that single crystal pCdTe gives a large series resistance, which under realistic working conditions reduces any photovoltage present at the junction. The aim of this work is to investigate further the possibility of pCdTe-nCdSe heterojunction solar cells, by sputtering a double thin film heterojunction, thus eliminating the series resistance problem. This method of construction would be cheap and could give rise to large area cells at no appreciable increase in cost. However, sputtered thin film heterojunctions have a greatly increased defect density which can affect the properties of the heterojunction substantially. The

electrical and optical properties of the heterojunction have, therefore, been investigated to ascertain how significant this effect is in practice.

CHAPTER 2

HETEROJUNCTION THEORY

2.1 DEFINITION

A heterojunction is an electrical junction between any two dissimilar materials. Hence, for example, an electrical contact to a material used in a device is a heterojunction. However, in most cases the term 'heterojunction' implies a semiconductor heterojunction, where at least one of the constituents is a semiconductor.

In general, heterojunction theories can be classified into two types: theories applying to (i) abrupt heterojunctions and (ii) graded heterojunctions. This duality also appears in theories for homojunctions. In an abrupt heterojunction, there is an instantaneous change in the semiconductor properties and structure at an interface extending no more than a few atomic spacings. More recently the theory has been widened to consider heterojunctions which contain a diffuse or graded junction in which the properties change across the interface. Graded heterojunction theory was developed from the theory of inhomogeneous mixed crystals (Van Ruyven, 1972). Heterojunctions can also be classified into isotype and anisotype heterojunctions where both semiconductors are doped by the same type of impurity (n-n, p-p), or different types of impurities (p-n, n-p) respectively.

2.2 p-n ANISOTYPE HETEROJUNCTION THEORY - ANDERSON'S THEORY

The heterojunctions investigated in this thesis are anisotype abrupt junctions and so we shall consider theories applicable only to this case in detail. However, these theories can be applied to isotype heterojunctions after minor modification. In this work the heterojunctions are fabricated by sputtering at a temperature of 200°C, sputtering is mainly a mass transfer deposition process (cf. chapter 3) and gives rise to an interface between the layers only a few atomic spaces in thickness. The sputtering temperature is too low to allow any significant inter-diffusion to occur between the two semiconductors and, therefore, these heterojunctions can be considered to be abrupt.

Anderson's theory is an extension of p-n heterojunction theory, and the assumption is made in this theory that there is a negligible concentration of interface and surface states at the interface between the single crystal semiconductors.

The energy band profile of an anisotype heterojunction is shown in fig. 2.1, derived according to Anderson's theory by Milnes and Feucht (1972). The space charge transition width of the junction is

$$W = \left[\frac{2\varepsilon_1\varepsilon_2(V_D - V_a)(N_{A2}+N_{D1})^2}{q(\varepsilon_1 N_{D1} + \varepsilon_2 N_{A2})N_{D1}\,N_{A2}}\right]^{\frac{1}{2}} \qquad (2.1)$$

Eqn. (2.1) is obtained by solving Poisson's equation with the assumption of a Schottky barrier at the junction. The relative voltages supported in each of the semiconductors are:

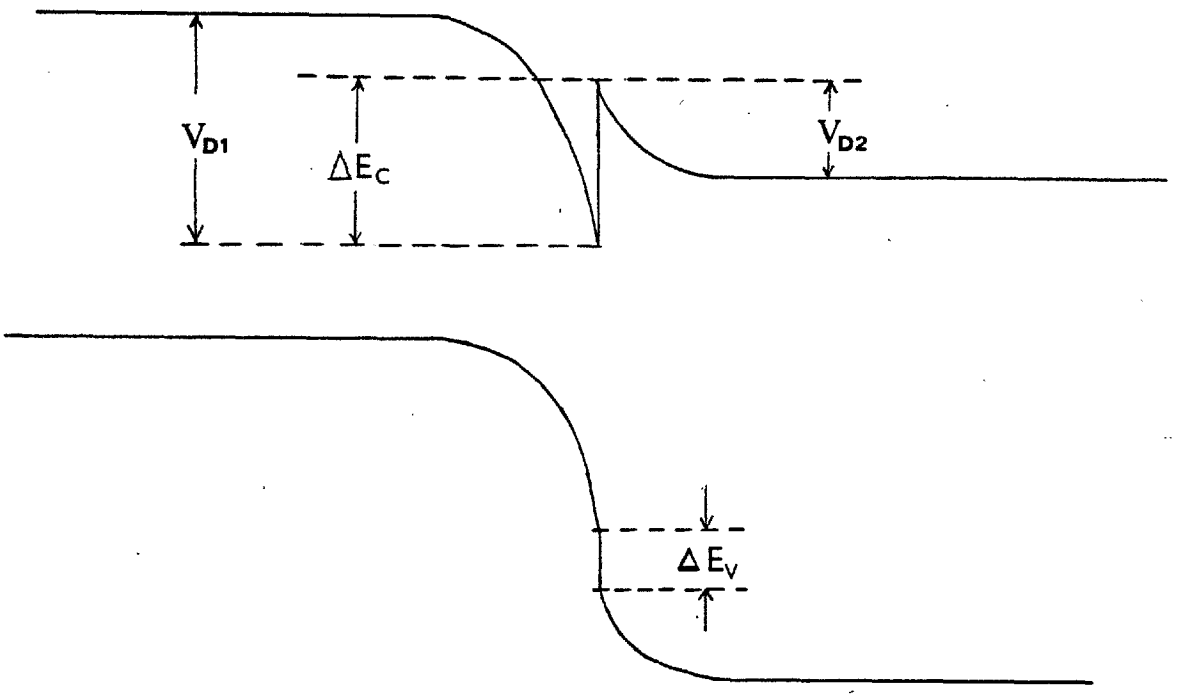

Fig. 2.1: Energy Band Diagram of a p-n Heterojunction (Milnes and Feucht, 1972)

$$(V_{D1} - V_1)/(V_{D2} - V_2) = N_{A2}\,\varepsilon_2/N_{D1}\varepsilon_1 \qquad (2.2)$$

where

$$V_1 + V_2 = V_a$$

and

$$V_{D1} + V_{D2} = V_D$$

The transition capacitance per unit area is

$$C/a = \left[\frac{q(N_{D1}N_{A2}\varepsilon_1\varepsilon_2)}{2(\varepsilon_1 N_{D1}+\varepsilon_2 N_{A2})} \times \frac{1}{(V_D - V_a)} \right]^{\frac{1}{2}} \qquad (2.3)$$

a generalisation of the homojunction result.

The dependence of current upon voltage has the same form as the Schottky diode equation:

$$I = I_o \left[\exp\left(\frac{qV_a}{kT}\right) - 1 \right] \qquad (2.4)$$

These equations only apply to ideal or perfect heterojunctions where the influence of the interface states is negligible. The properties of real heterojunctions, however, are dominated by interface states, and it is necessary to modify the Anderson model in order to explain the observed behaviour of such junctions.

2.3 THE EFFECT OF INTERFACE STATES ON THE CHARACTERISTIC OF HETEROJUNCTIONS

2.3.1 The Origin of Interface States

Interface states are due to (i) lattice mismatch and (ii) difference in expansion coefficients of the two semiconductors. Thermal mismatch causes mechanical strain at the interface during the cooling of the specimen from the growth temperature to room temperature. Lattice mismatch on the other hand leads to the formation of dangling bonds (fig. 2.2), as mismatch limits the number of possible completed bonds at the interface. Certain bonding electrons in one semiconductor find no bonding orbital in the other and are left unused, or form bonds to other orbitals among themselves.

Holt (1966),by considering the difference between the number of bonds per unit area at the two semiconductor interfaces, has calculated the theoretical value of the dangling bond density which is, in fact, the optimum density of dangling bonds formed at the interface (table 2.1). He showed that different crystal planes exhibit different dangling bond densities. However, the difference among the planes is not significant and for a polycrystalline structure, the dangling bonds density is an average.one. These results may be modified as Tansley (I, 1971) has pointed out, for experiment shows that not all dangling bonds are active as the surfaces usually restructure themselves to maximise the number of bonds formed.

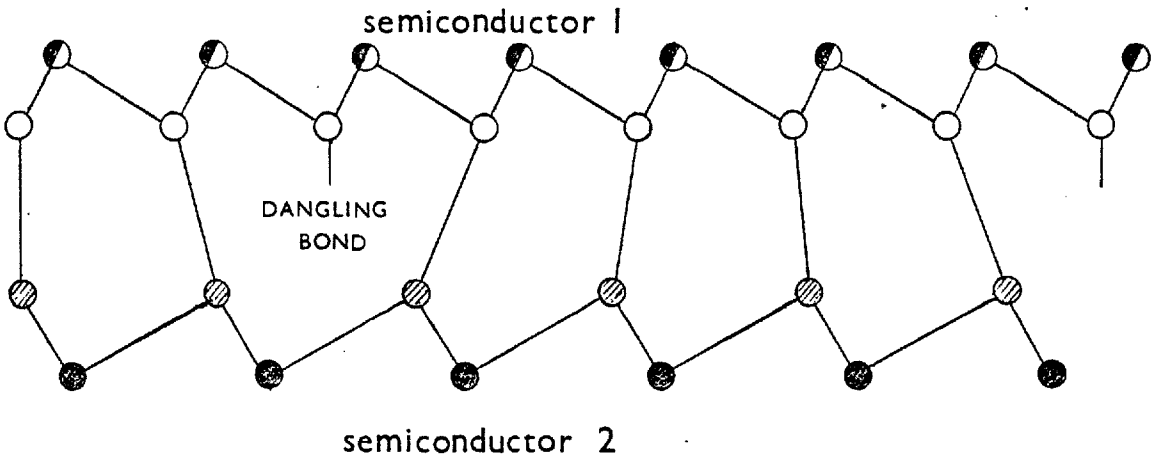

Fig. 2.2: Schematic Representation of Dangling Bonds Formed at the Interface of a Heterojunction (after Holt, 1966)

Crystal Plane	ΔN_d
(100)	$4(\lambda_2^2 - \lambda_1^2)/\lambda_1^2\lambda_2^2$
(110)	$2\sqrt{2}(\lambda_2^2 - \lambda_1^2)/\lambda_1^2\lambda_2^2$
{111}	$4(\lambda_2^2 - \lambda_1^2)/\sqrt{3}\lambda_1^2\lambda_2^2$

Table 2.1: Interface States Density (Holt, 1966)

Strain introduced during the cooling of the specimen from the sputtering temperature to room temperature largely depends on the difference of the thermal expansion coefficients. If the difference is small then only mechanical strain occurs compressing or expanding the lattice. However if it is large (>5% mismatch, Tansley I, 1971), dislocations and other physical defects can form at the interface. Direct examination of the interface (Tansley I, 1971) revealed that only a few percent of the density calculated by Holt's method, and most interface states are due to dislocations formed into a layer or grid.

Another form of interface state is formed when the surface states of semiconductors react with the ambient gases which may be chemisorbed onto both surfaces of the heterojunction. The nature of these new interface states depends very much on the types of gas adsorbed and whether they give rise to a superlattice or not. Annealing can cause desorption from the surface but this usually occurs only at high temperature ($\sim 600^{o}C$). Such temperatures also cause interdiffusion of the two materials and the heterojunction becomes graded which also reduces the effect of lattice mismatch. Hence, in order to maintain an abrupt heterojunction, relatively low temperatures were maintained during sputtering ($200-230^{o}C$).

2.3.2 Space Charge Region at the Interface

(a) No Interface State

Without interface states, the junctions can be described by Anderson's model (Milnes and Feucht, 1972).

Consider both semiconductors to be single crystals

and that depletion occurs in both materials (fig. 2.3).

Solving Poisson's equation (Hipwood, 1977):

$$\frac{d^2V}{dx^2} = - \frac{\rho(x)}{\varepsilon\varepsilon_o} \qquad (2.5)$$

For three regions (fig. 2.3), with space charge in each region, $\rho(x)$ is given by

Region I,

$$\rho(x) = q\, N_{D1} \qquad 0 < |x_1| < \ell_1$$

Region II,

$$\rho(x) = -q\, N_{A2} \qquad 0 > |x_2| > -\ell_2$$

Region III,

$$\rho(x) = 0 \qquad x > -\ell_2;\ x < \ell_1$$

which gives

$$\frac{dV_1}{dx_1} = \frac{qN_{D1}}{\varepsilon_1\varepsilon_o}\ (x_1 - \ell_2) \quad \text{(Region I)} \qquad (2.6a)$$

$$\frac{dV_2}{dx_2} = -\frac{qN_{A2}}{\varepsilon_2\varepsilon_o}\ (x_2 - \ell_2) \quad \text{(Region II)} \qquad (2.6b)$$

$$\therefore\ V_1 = \frac{qN_{D1}}{\varepsilon_1\varepsilon_o}\ \left(\frac{x_1^2}{2} - x_1\ell_1 + \ell^2/_2\right) \qquad (2.7a)$$

$$V_2 = V_D - \frac{qN_{A2}}{\varepsilon_o\varepsilon_2}\ (x_2\ell_2 + x^2/_2 + \ell^2/_2) \qquad (2.7b)$$

where at ℓ_1, $V = 0$; at ℓ_2, $V = V_D$, and ℓ_1 and ℓ_2 are the

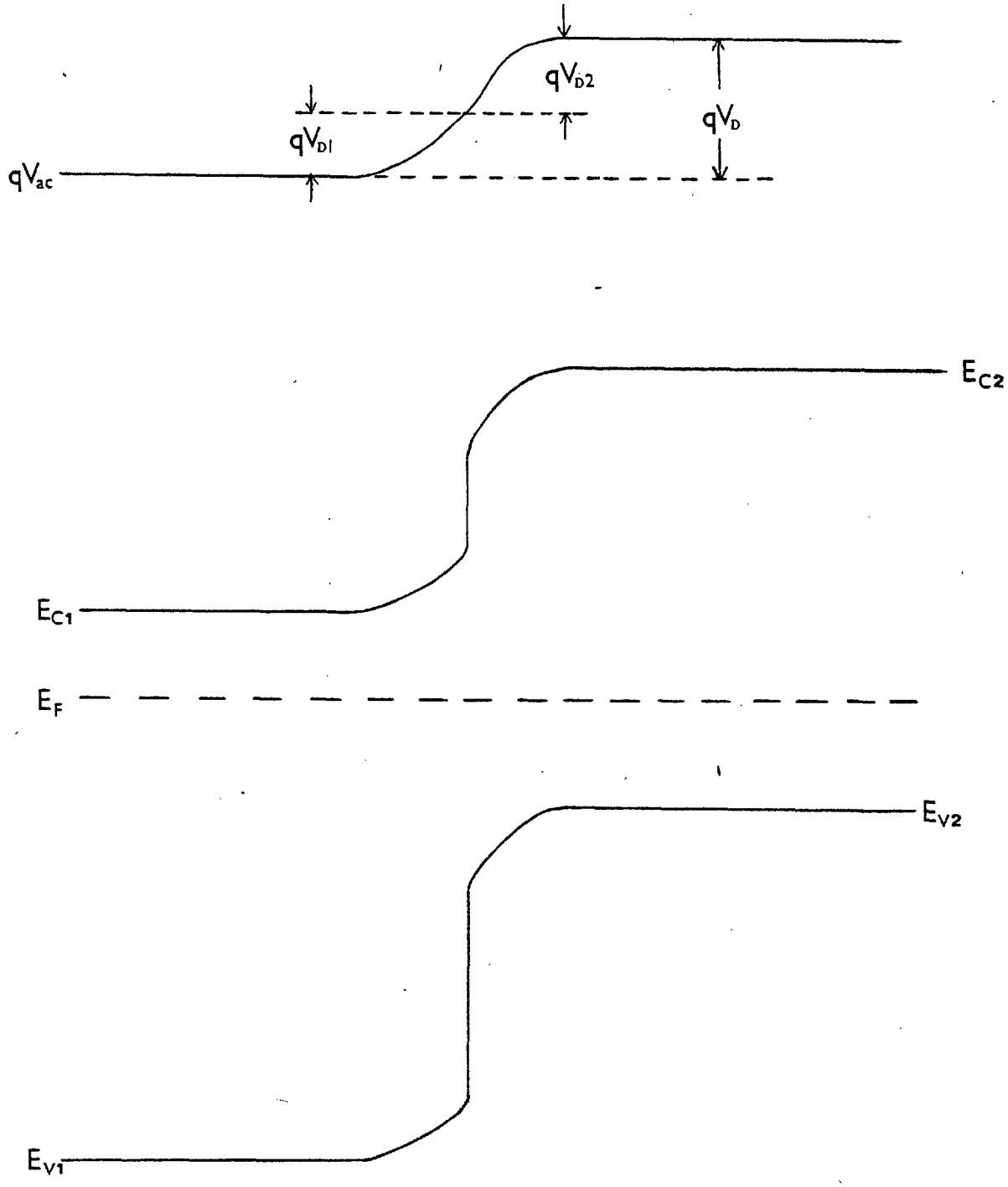

Fig. 2.3: Double Depleted p-n Heterojunction Energy Band Diagram (after Sadek, 1975)

width of the depletion layers in semiconductors 1 and 2 respectively. The appropriate boundary conditions are

$$|V_1(0)| = |V_2(0)| \tag{2.8}$$

$$\varepsilon_o\varepsilon_1 \left.\frac{dV_1}{dx}\right|_{x=0} = \varepsilon_o\varepsilon_2 \left.\frac{dV_2}{dx}\right|_{x=0} \tag{2.9}$$

which when substituted into eqns. (2.6a) and (2.6b), (2.7a) and (2.7b) give

$$V_D = \frac{qN_{D1}}{\varepsilon_o\varepsilon_1} \ell^2/_2 + \frac{qN_{A2}}{\varepsilon_1\varepsilon_2} \ell^2/_2 \tag{2.10}$$

$$\ell_1 = \left[\frac{2\varepsilon_o\varepsilon_1\varepsilon_2 N_{A2} V_D}{qN_{D1}(\varepsilon_2 N_{A2}+\varepsilon_1 N_{D1})}\right]^{\frac{1}{2}} \tag{2.11a}$$

$$\ell_2 = \left[\frac{2\varepsilon_o\varepsilon_1\varepsilon_2 N_{D1} V_D}{qN_{A2}(\varepsilon_2 N_{A2}+\varepsilon_1 N_{D1})}\right]^{\frac{1}{2}} \tag{2.11b}$$

The relative built-in voltages on either side of the junction can be obtained by using the boundary condition

$$|V_1(0)| = |V_2(0)| = V_{D1}$$

Applying this to eqns. (2.7a) and (2.7b) we have,

$$V_{D1}/V_{D2} = N_{A2}\varepsilon_2/N_{D1}\varepsilon_1 \tag{2.12}$$

With an applied voltage, V_a, we may write

$$V_2(\ell_2) = V_D - V_a$$

and eqns. (2.7a) and (2.7b), (2.10) and (2.11a) and (2.11b) can be modified to include the applied voltage and eqn. (2.12) becomes

$$\frac{V_{D1} - V_{a1}}{V_{D2} - V_{a2}} = \frac{N_{A2}\varepsilon_2}{N_{D1}\varepsilon_1} = K \qquad (2.13)$$

where

$$V_a = V_{a1} + V_{a2}$$

The model shows that the bands are bent parabolically (eqn. 2.7) at the junction interface and that the width of the depletion layers depends on the square root of the potential difference across the junction. All these results are exactly analogous to the results obtained for the homojunction. Also, it can be seen that the voltage dropped across either side of the junction is proportional to the doping density in that region.

For isotype heterojunctions, these results must be modified as one side of the junction has an accumulation layer. Hence, the effect of mobile charge becomes significant (Hipwood, 1977, Cserveny, 1968). The modification can also be used to correct for the majority carrier tails at the edge of the depletion layer. Although

this approach was first reported by Cserveny in (1968) in this work we shall consider the method due to Hipwood (1977) here.

The assumptions used are:

(i) Complete ionisation at room temperature

(ii) Non-degenerate semiconductors so Boltzman statistics can be applied.

(iii) $N_D >> N_A$ for n-type semiconductors

and

$N_A >> N_D$ for p-type semiconductors

Poisson's equation for $x > 0$ may be written

$$\frac{d^2\psi}{dx^2} = - q^2/_{kT\varepsilon_o\varepsilon_2} (- N_{A2} + p_2 - n_2) \qquad (2.14)$$

where

$\psi = qV/_{kT}$, is a dimensionless potential.

Let E_{Vb} be the valence band edge in the bulk of semiconductor 2, where $p_b = N_{A2}$.

$$\therefore \quad N_{A2} = N_{V2} \exp\left[\frac{E_{Vb}-E_F}{kT}\right] \qquad (2.15)$$

Also,

$$p_2 = N_{V2} \exp\left[\frac{E_V-E_F}{kT}\right]$$

$$= N_{V2} \exp\left[\frac{E_{Vb}-E_F}{kT}\right] \exp\left[\frac{E_V-E_{Vb}}{kT}\right]$$

$$\therefore \quad p_2 = N_{A2} \exp\left[\psi_2 - \psi_D + \psi_a\right] \tag{2.16}$$

The last term at the R.H.S. of eqn. (2.14) is the contribution from minority carriers which is only significant if a notch (Tansley I, 1971) is present at the interface junction, trapping the minority carriers. It happens that the p-n heterojunction model under consideration in this work has no notch (Sadek, 1975) at the interface, and therefore in the present case the contribution from that last term can be ignored. Eqn. (2.14) then becomes:

$$\frac{d^2\psi_2}{dx^2} = \frac{q^2 N_{A2}}{kT\varepsilon_o\varepsilon_2} \left[\exp(\psi_2 - \psi_D + \psi_a) - 1\right]$$

defining $\alpha = x/L_D$, where $L_D^2 = \dfrac{kT\varepsilon_o\varepsilon}{q^2N}$, the Debye length. We may write,

$$\frac{d^2\psi_2}{d\alpha^2} = \exp(\psi_2 - \psi_D + \psi_a) - 1 \tag{2.17}$$

Let $\bar{\varepsilon} = \dfrac{d\psi}{d\alpha}$ be the dimensionless electric field, integrating eqn. (2.17):

$$\tfrac{1}{2}\left[\bar{\varepsilon}^2\right]_0^{\bar{\varepsilon}_2} = \left[\exp(\psi_2 - \psi_D + \psi_a) - \psi\right]_{\psi_D - \psi_a}^{\psi_2}$$

$$\therefore \quad \tfrac{1}{2}\,\bar{\varepsilon}_2^2 = \left[\psi_D - \psi_a - \psi_2 - 1 + \exp(\psi_2 - \psi_D + \psi_a)\right] \tag{2.18}$$

Using similar arguments for semiconductor 1; i.e. with

$$n_1 = N_{D1} \exp(-\psi_1) \tag{2.19}$$

Poisson's equation may be written

$$\frac{d\bar{\varepsilon}_1}{d\alpha} = \frac{d^2\psi_1}{dx^2} = 1 - \exp(-\psi_1) \qquad (2.20)$$

which on integration gives the field as

$$\frac{1}{2}\,\bar{\varepsilon}_1^2 = \psi_1 + \exp(-\psi_1) - 1 \qquad (2.21)$$

The continuity conditions at x = 0 requires that:

$$\psi_1(0) = \psi_2(0) \quad , \quad \varepsilon_1 \left.\frac{dV_1}{dx}\right|_{x=0} = \varepsilon_2 \left.\frac{dV_2}{dx}\right|_{x=0}$$

Thus from eqns. (2.18) and (2.21)

$$\frac{1}{2}\,\bar{\varepsilon}_2^2(0) = \left[\psi_D - \psi_a - \psi_o - 1 + \exp(\psi_o - \psi_D + \psi_a)\right]$$

$$\frac{1}{2}\,\bar{\varepsilon}_1^2(0) = \psi_o + \exp(-\psi_o) - 1$$

By division:

$$\left(\frac{\bar{\varepsilon}_1(0)}{\bar{\varepsilon}_2(0)}\right)^2 = \frac{N_{A2}\varepsilon_2}{N_{D1}\varepsilon_1} = \frac{\exp(-\psi_o) + \psi_o - 1}{\psi_D - \psi_a - \psi_2 - 1 + \exp(\psi_o - \psi_D + \psi_a)}$$

$$= K \qquad (2.22)$$

This result may be compared to the result obtained for homojunctions by Gemmel and Scharfetter (1967):

$$\frac{\psi_o - 1}{\psi_D - \psi_a - \psi_o - 1} = K \qquad (2.23)$$

The extra terms in eqn. (2.22) arise from the discontinuity in the carrier concentrations at the interface.

If the voltages supported by both semiconductors are greater than a few kT, which is practically always true, then eqn. (2.23) is a good approximation to eqn. (2.22). Eqn. (2.22) can be approximated for small ψ by:

$$K = \left[\exp(-\psi_o) + \psi_o - 1 \right] / \left[\psi_D - \psi_a - \psi_o - 1 \right]$$

and eqn. (2.18) becomes

$$|\bar{\varepsilon}_2| = \frac{d\psi_2}{d\alpha} = \sqrt{2} \{ \psi_D - \psi_a - \psi_2 - 1 + \exp(\psi_2 - \psi_D + \psi_a) \}^{\frac{1}{2}} \tag{2.24}$$

Expanding the exponential term in eqn. (2.24):

$$\frac{d\psi_2}{d\alpha} = (\psi_2 - \psi_D + \psi_a)$$

$$\therefore \quad \alpha_2 = \ell n \left[\frac{\psi_2 - \psi_D + \psi_a}{\psi_o - \psi_D + \psi_a} \right] \tag{2.25}$$

Similarly, from eqn. (2.21)

$$\frac{d\psi_1}{d\alpha} = \sqrt{2} \{ \psi_1 + \exp(-\psi_1) - 1 \}^{\frac{1}{2}}$$

$$\simeq \psi_1$$

$$\therefore \quad -\alpha_1 = \ell n(\psi_1 / \psi_o) \tag{2.26}$$

Hence, the potential is exponentially dependent on the distance, as compared to the relationship derived from eqn.. (2.7) which can be rewritten as:

$$x_1 = \ell_1 - \left(2 \frac{\varepsilon_o \varepsilon_1}{qN_{D1}} V_1\right)^{\frac{1}{2}} \qquad (2.27)$$

$$x_2 = \ell_2 - \left[\frac{2\varepsilon_o \varepsilon_2}{qN_{A2}} (V_D - V_2)\right]^{\frac{1}{2}} \qquad (2.28)$$

which is parabolically dependent on the distance. The change in the relationship is due to the inclusion of the correction for the majority carrier tails at the edge of the depletion layer.

(b) Inclusion of Interface States

The effect of interface states is to alter the potential profile at the interface. Since interface states are generally localised, the charge due to these states can be regarded as a sheet charge situated at the interface.

Consider the interface states as monopoles with a constant charge per unit area of Q_{Is}, then, Q_{Is} is equal to the discontinuity in the dielectric displacement vector and the boundary condition, eqn. (2.9), can be replaced by:

$$\varepsilon_1 \left.\frac{dV_1}{dx}\right|_{x=0} = \varepsilon_2 \left.\frac{dV_2}{dx}\right|_{x=0} + Q_{Is} \qquad (2.29)$$

Using the new boundary conditions, eqn. (2.22) becomes:

$$K = \left\{ \frac{\left[\exp(-\psi_o) + \psi_o - 1\right]^{\frac{1}{2}} - \left[Q_{Is}/\zeta\sqrt{2}\right]}{\left[\psi_D - \psi_a - \psi_o + 1 - \exp(\psi_o - \psi_D + \psi_a)\right]^{\frac{1}{2}}} \right\}^2 \qquad (2.30)$$

where $\zeta = qL_{D1} N_{D1}$.

For small ψ_o, K can be approximated to:

$$K = \left[\frac{\psi_o/\sqrt{2} - Q_{IS}/(\sqrt{2}\,\zeta)}{(\psi_D - \psi_a - \psi_o)/\sqrt{2}} \right] \tag{2.31}$$

$$= \left[(\psi_o - Q_{IS}/\zeta)/(\psi_D - \psi_a - \psi_o) \right]^2$$

$$\therefore \quad \psi_o = \left[K^{\frac{1}{2}}(\psi_D - \psi_a) + Q_{IS}/\zeta \right]/(K^{\frac{1}{2}} + 1) \tag{2.32}$$

Hence, the potential at interface increases linearly with Q_{IS}. Substituting eqn. (2.32) into eqns. (2.25) and (2.26) shows that the space charge width increases as ψ_o increases, i.e. the potential barrier is getting steeper, enhancing the probability of tunnelling. Thus, the effect of interface states on the junction potential is to increase the field strength, giving rise to a leaky junction due to electron tunnelling through the junction.

2.3.3 Junction Capacitance

The variation of space charge width of the junction with respect to the applied field is reflected in the form of the charge in the capacitance. In this section this behaviour is discussed (1) in the absence and (2) in the presence of interface states.

(1) In the absence of interface states

Two conditions govern the behaviour of the junction capacitance (Donnelly and Milnes, 1967)

charge neutrality : $Q_1 + Q_2 = 0$ (2.33a)

and the potential at the junction:

$$\psi_1(0) + \psi_2(0) = 2\gamma(\psi_D - \psi_a) \tag{2.33b}$$

where γ is the fraction of voltage dropped across the space charge region of semiconductor 1.

If the charge neutrality is considered, the capacitance can be calculated by considering either Q_1 or Q_2. In terms of Q_1 the capacitance is, by definition, given by,

$$C_o = \left[\frac{dQ_1}{dV_a}\right]$$

$$= \left[\frac{dQ_1}{d\psi_a}\right] \frac{q}{kT}$$

Now,

$$Q_1 \equiv \frac{\varepsilon_1 \varepsilon_o kT}{qL_{D1}} \bar{\varepsilon}_1(0)$$

$$\therefore \quad Q_1 = qN_{D1}L_{D1}\sqrt{2}(\exp(-\psi_1(0)) - 1 + \psi_1(0))^{\frac{1}{2}} \tag{2.34}$$

Similarly

$$Q_2 = -qN_{A2}L_{D2}\sqrt{2}\left[\psi_D - \psi_a - \psi_2(0) - 1 + \exp(\psi_2(0) - \psi_D + \psi_a)\right]^{\frac{1}{2}} \tag{2.35}$$

as

$$\frac{dQ_1}{d\psi_a} = \frac{dQ_1}{d\psi_1(0)} \frac{d\psi_1(0)}{d\psi_a}$$

By solving eqns. (2.33a) and (b), $\frac{d\psi_1(0)}{d\psi_a}$ can be obtained, and $\frac{dQ_1}{d\psi_1}$ is given by eqn. (2.34).

Hence,

$$\frac{dQ_1}{d\psi_a} = \{2q\gamma N_{D1}N_{A2}L_{D1}L_{D2}(1-e^{-\psi_1(0)}) \left[\exp(\psi_2(0)-\psi_D+\psi_a) - 1\right]\} \times$$

$$\{N_{D1}L_{D1}\bar{\varepsilon}_2(0)(1-e^{-\psi_1(0)}) + N_{A2}L_{D2}\psi_1(0)\left[\exp(\psi_2(0)-\psi_D+\psi_a)-1\right]\}^{-}$$

$$\therefore C_o = \left[2q^2\gamma N_{D1}N_{A2}L_{D1}L_{D2}AB\right]/\{N_{D1}L_{D1}\bar{\varepsilon}_2(0)A + N_{A2}L_{D2}\bar{\varepsilon}_1(0)\ B\} \times (kT)^{-1} \qquad (2.36)$$

where

$$A = \left[1-\exp(-\psi_1(0))\right]$$

and

$$B = \left[\exp(\psi_2(0)-\psi_D+\psi_a) - 1\right]$$

For

$$\exp(-\psi_o) \ll 1$$

$$C \propto (\psi_D - \psi_a)^{-\frac{1}{2}}$$

i.e. eqn. (2.36) is in the form used by Anderson (cf. eqn. 2.3). However, if ψ_o ceases to be negligible, which can happen if K (cf. eqns. (2.22) and (2.23) is large, then eqn. (2.36) would deviate from eqn. (2.3). The junction capacitance would have a more complex dependency on ψ_o and $(\psi_D - \psi_a)$ as in eqn. (2.36).

(2) In the presence of interface states

The presence of trapped charge at the interface modifies the two conditions given in (2.23a) and (2.33b) giving,

$$Q_1 + Q_2 + Q_{IS} = 0 \tag{2.37a}$$

$$\psi_1(0) + \psi_2(0) + \phi_m = 2\gamma \quad (\psi_D - \psi_a) \tag{2.37b}$$

Using similar arguments as those given above, the capacitance given again by

$$C = \frac{dQ_1}{dV_a}$$

$$= \frac{q}{kT} \quad \frac{dQ_1}{d(+\psi_a)}$$

is found to be

$$C = \frac{qN_{D1}L_{D1}A}{kT} \left[qN_{A2}L_{D2}B(2\gamma + \frac{d\phi_m}{d(+\psi_a)}) + \frac{dQ_{IS}}{d(+\psi_a)} \bar{\varepsilon}_2(0) \right] \Omega^{-1} \tag{2.38}$$

where

$$\Omega = N_{D1}L_{D1}\bar{\varepsilon}_2(0)\ A + N_{A2}L_{D2}\bar{\varepsilon}_1(0)\ B$$

Using Q_2 we have,

$$C = \frac{qN_{A2}L_{D2}B}{kT} \left[q\ N_{D1}L_{D1}A(2\gamma + \frac{d\phi_m}{d(+\psi_a)}) + \frac{dQ_{IS}}{d(+\psi_a)} \bar{\varepsilon}_1(0) \right] \Omega^{-1} \tag{2.39}$$

Thus,

$$C = C_o + (C_\phi + C_{IS}) \qquad (2.40)$$

where $C_\phi = \frac{q^2}{kT} N_{A2}N_{D1}L_{D2}L_{D1}AB \frac{d\phi_m}{d(+\psi_a)} \ \Omega^{-1}$, is the capacitance due to the electric dipole and $C_{IS} = \Xi \frac{dQ_{1s}}{d\psi_a} \ \Omega^{-1}$, the capacitance due to the interface trapped charge.

$\Xi = qN_{D1}L_{D1}A\bar{\epsilon}_2(0)/kT$ if from a consideration of Q_1, or

$\Xi = qN_{A2}L_{D2}B\bar{\epsilon}_1(0)/kT$ if Q_2 is considered. C_{IS} is the only term in eqn. (2.41) which depends on the physical properties of one or other of the semiconductors although it depends, only upon the properties of one of them. Thus C_{IS} is not due only by interface trapped charge but depends upon the interaction of the trapped charge with the concentration of dopant in one semiconductor and its dielectric constant.

2.3.4 The A.C. Field Effect

(a) Capacitance

Eqn. (2.40) predicts the behaviour of the junction capacitance for a d.c. bias field. Let us now consider the case when an a.c. signal is applied to the junction. Applying small signal a.c. theory to find the admittance of the junction (Donnelly and Milnes, 1967) gives

$$(\psi_D - \psi_a) = (\psi_{Do} - \psi_{ao}) + (\psi_{D1} - \psi_a)\, e^{j\omega t}$$

$$\psi_1(0) = \psi_{10}(0) + \psi_{11}(0)\, e^{j\omega t}$$

$$\psi_2(0) = \psi_{20}(0) + \psi_{21}(0)\, e^{j\omega t}$$

$$\phi_m = \phi_m(0) + \phi_{m1}\, e^{j\omega t}$$

$$\phi_{mo} = \phi_{mo}(0) + \phi_{mo1}\, e^{j\omega t}$$

$$Q_1 = Q_{10} + Q_{11}\, e^{j\omega t}$$

$$Q_2 = Q_{20} + Q_{21}\, e^{j\omega t}$$

$$Q_{IS} = Q_{IS}(0) + Q_{IS1}\, e^{j\omega t}$$

$$Q_{ISO} = Q_{ISO}(0) + Q_{ISO1}\, e^{j\omega t} \qquad (2.41)$$

Using a relaxation model,

$$\frac{dQ_{IS}}{dt} = -\left(\frac{Q_{IS}-Q_{ISO}}{\tau_q}\right) \qquad (2.42)$$

where Q_{IS} is the actual charge on interface states, Q_{ISO} is the steady charge and τ_q is the relaxation time. A similar relationship can be applied to the electric dipole, i.e.

$$\frac{d\phi_m}{dt} = -\left(\frac{\phi_m-\phi_{mo}}{\tau_\phi}\right) \qquad (2.43)$$

for a.c. eqns. (2.37) can be replaced by

$$Q_{11} + Q_{21} + Q_{IS1} = 0 \qquad (2.44a)$$

$$\phi_{m1} + \psi_{11}(0) + \psi_{21}(0) = 2\gamma\,(\psi_{D1} - \psi_{a1}) \qquad (2.44b)$$

Using eqns. (2.41) and (2.42),

$$\frac{dQ_{IS}}{dt} = j\omega Q_{IS1} = - \frac{Q_{IS1}-Q_{ISO1}}{\tau_q}$$

$$\therefore \quad Q_{IS} = \frac{Q_{ISO1}}{1+j\omega\tau_q}$$

$$= \frac{-1}{1+j\omega\tau_q} \frac{dQ_{ISO}}{d\psi_A} (\psi_{D1} - \psi_{a1}) \qquad (2.45)$$

Similarly,

$$\phi_{m1} = \frac{-1}{1+j\omega\tau_\phi} \frac{d\phi_m}{d\psi_a} (\psi_{D1} - \psi_{a1}) \qquad (2.46)$$

By definition,

$$I = \frac{kT}{q} (\psi_{D1} - \psi_{a1}) Y$$

$$= \frac{dQ_1}{dt}$$

$$= j\omega \frac{dQ_1}{d\psi_1} \psi_{11}(0) \qquad (2.47)$$

where Y is the small signal a.c. junction admittance in the terms Q_1.

By solving for $\psi_{11}(0)$ using eqns. (2.44), (2.45) and (2.46) in terms of $\frac{dQ_1}{d\psi_1}$, $\frac{dQ_2}{d\psi_2}$, $\frac{dQ_{ISO}}{d\psi_a}$ and $\frac{d\phi_m}{d\psi_a}$, then, substituting them through eqns. (2.34) and (2.35), Y can be found. The junction capacitance is then obtained as:

$$C_f = \Omega^{-1} \frac{q}{kT} N_{D1} L_{D1} A \left[qN_{A2} L_{D2} B(2\gamma + \frac{1}{1+(\omega\tau_\phi)^2} \frac{d\phi_m}{d\psi_a}) + \frac{dQ_{ISO}}{d\psi_a} \frac{\bar{\varepsilon}_2(0)}{1+(\omega\tau_q)^2} \right] \tag{2.48}$$

This equation is identical to eqn. (2.38) except for the additional coefficients in the terms for the interface charge and the electrical dipoles. These coefficients show that within the ranges where there is a significant contribution from these two terms, peaks will be observed when $\omega = \tau_\phi$ and or τ_q. When Q_2 is considered instead of Q_1 a similar change in the coefficients of the $\frac{dQ_{ISO}}{d\psi_A}$ term occurs instead, as we have already seen for the d.c. capacitance in section 2.3.3(b).

(b) Voltage-current relationship

By using similar arguments to those used by Many et al. (1965) the current density is given as:

$$J(t) = q \mu_n n_b F(x,t) + \frac{dQ}{dt} \tag{2.49}$$

Consider semiconductor 1 in the absence of trapped interface charge, then

$$J_1(t) = q \mu_n n_1 F_1(x,t) + \frac{dQ_1}{dt}$$

from eqn. (2.19), the current density becomes:

$$J_1(t) = \frac{kT}{L_{D1}} \mu_n \, N_{D1} \, \exp(-\psi_1) \, \frac{d\psi_1}{d\alpha} + \frac{dQ_1}{dt}$$

Apply small signal a.c. theory and consider the a.c. part only,

$$J_{11}(t) = \frac{kT}{L_{D1}} \mu_n \, N_{D1} \, \exp(-\psi_1) \, \frac{d\psi_{11}}{d\alpha} + j\omega \frac{dQ_1}{d\psi_1(0)} \, \psi_{11}(0)$$

From section 2.3.4a ,

$$J_{11}(t) = \left[\left(\frac{kT}{L_{D1}} \mu_n \, N_{D1} \, \exp(-\psi_1) \frac{d\psi_{11}}{d\alpha}\right)^2 + \left[\omega C_o(\psi_{D1}-\psi_a)\right]^2\right]^{\frac{1}{2}}$$

(2.50)

A similar expression can also be obtained for $J_{21}(t)$.

Now again consider semiconductor 1 but in the presence of trapped interface charge giving rise to electric dipoles. The conditions are the same as (2.34a) using the relaxation model we now have

$$J_{11}(t) = \left\{\left(\frac{kT}{L_{D1}} \mu_n N_{D1} \, \exp(-\psi_1) \, \frac{d\psi_{11}}{d\alpha}\right)^2 + \left[\omega C \, (Q_1)(\psi_{D1} - \psi_{a1})\right]^2\right\}^{\frac{1}{2}}$$

(2.51)

and similarly, for semiconductor 2,

$$J_{21}(t) = \left\{\left[\left(\frac{kT}{L_{D2}} \mu_p N_{A2} \, \frac{d\psi_{21}}{d\alpha} \, \exp(\psi_2 - \psi_D + \psi_a)\right]^2 + \left[\omega C \, (Q_2)(\psi_{D1} - \psi_{a1})\right]^2\right\}^{\frac{1}{2}}$$

(2.52)

Eqns. (2.51) and (2.52) contain two terms. The first term depends only on the physical properties of the semiconductors, whereas the second term contained contributions from Q_{Is} and ϕ_m. The second term, therefore, accounts for

the increase in the current density on the application of a.c. with respect to the current in a d.c. field.

These concepts will now be applied to an elucidation of the transport phenomena in heterojunctions.

2.3.5 Transport Mechanisms

In this section various transport mechanisms proposed for heterojunctions are compared. The heterojunction used in this thesis is an anisotype heterojunction, therefore only transport mechanims related to this type of heterojunction will be discussed. The diffusion and emission model proposed by Anderson (1962) has been referred to in section 2.2, and it can be seen that it is predominantly a thermal current model. With the presence of interface states, non-thermal current due to tunnelling and recombination can be the dominating transport mechanism.

Tunnelling models are widely used following the failure of the thermal emission model to explain experimental results satisfactorily (Riben and Feucht, 1966 a and b). However, due to the mathematical difficulties involved in evaluating the exact form of the electron tunnelling through the barrier, approximations must be made. Commonly, the potential barrier at the interface is either assumed to be parabolic or triangular (which is a first order approximation to a parabolic potential). The tunnelling current density is evaluated, using

$$J = \int_0^B P(t)\, J(E)\, dE \qquad (2.53)$$

where P(t) is the tunnelling probability, J(E) is the electron flux,both at an energy E. To evaluate the tunnelling probability, usually the WKB approximation is used in which it is assumed that the potential at the junction varies slowly with respect to the electron wavelength. A more complex but realistic expression has been proposed by Price (1962) to describe three possible tunnelling paths (fig. 2.4). Price made the assumption that the interface is perfectly ordered, abrupt and epitaxial, but he considered the variation of the electron potential in the interface region during the matching of the electronic wavefunctions. Unfortunately the resulting expression is too complex to be analytically useful.

However, Tansley (1966) and Rediker et al (1964) proposed more understandable tunnelling models to explain conduction mechanism under forward bias. Tansley, using the WKB approximation, found the tunnelling probability as

$$P \approx \exp\left[\xi \left(\sqrt{V_2 y} - V_2\right)\right] \qquad (2.54)$$

where $\xi = 2t'\sqrt{\frac{8m^*}{h}}$ and t' is a constant.

The current-voltage relation is then:

$$I = I_{oo} \exp\left(\frac{V_a}{V_o}\right) \exp\left(\frac{T}{T_o}\right) \qquad (2.55)$$

where

$$V_o = \frac{h}{\lambda 4t'\sqrt{2m^*}} \quad ; \quad T_o = \frac{4}{\lambda k V_D}\left[\frac{h^2}{32t'^2 m^*}\right]^{\frac{1}{2}} ,$$

$$I_{oo} = \exp\left[-\left(\frac{E_F}{kT} + \xi V_D \lambda\right)\right] \quad ; \quad 0 < \lambda < 1$$

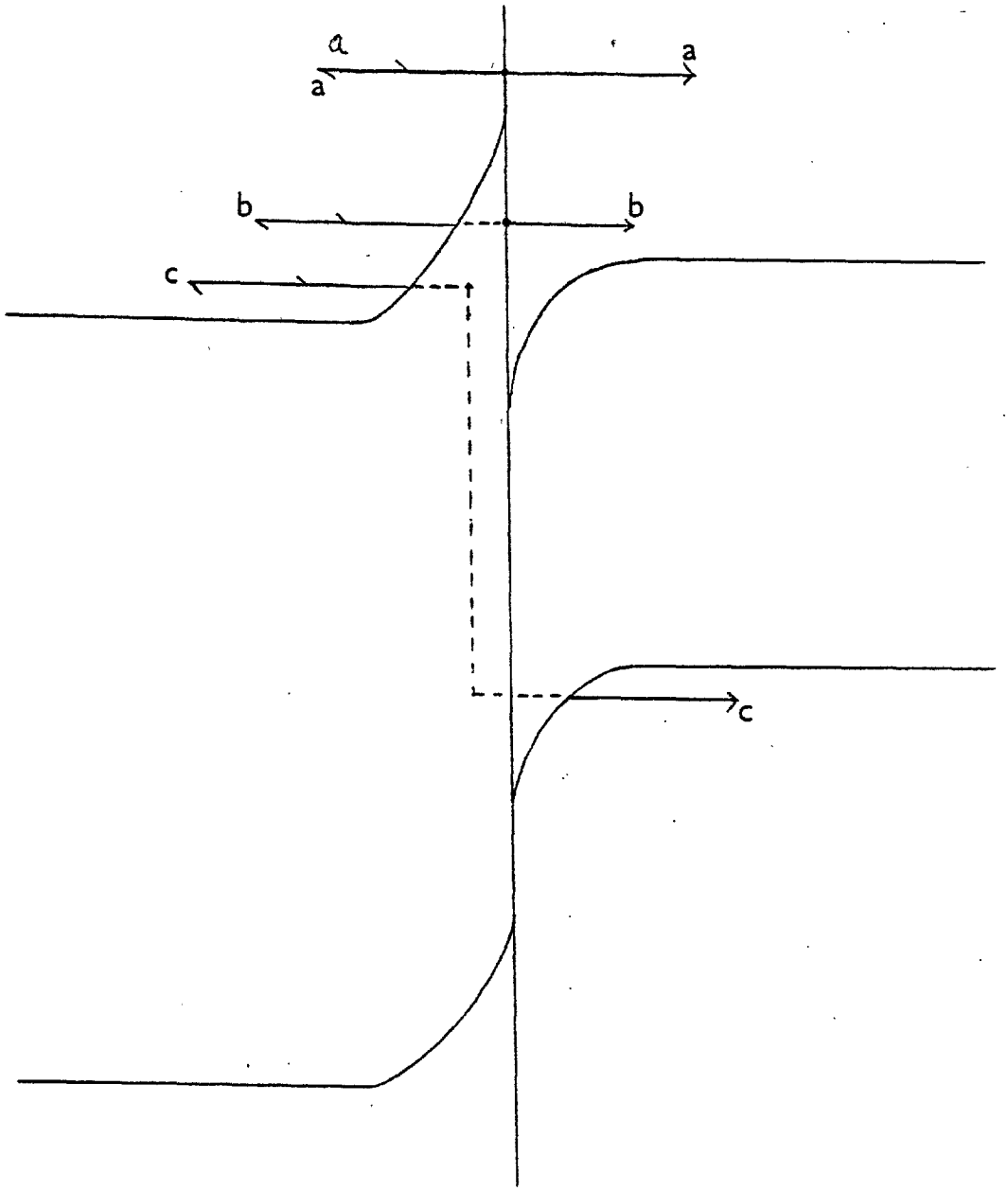

Fig. 2.4: Tunnelling Processes across the Junction (Price, 1962)

(a) Allowed-Allowed transmission through the interface

(b) Tunnelling transmission

(c) Interband tunnelling

Eqn. (2.55) which is similar to that obtained by Newman (1965) experimentally, is obtained using two assumptions: (a) It is postulated that there is an exponential band profile at the interface due to either impurities diffusing across the interface or minority carrier effects. (b) The density of the incident electron flux varies parabolically with band energy obeying Boltzmann's statistic and the interfacial perturbation is neglected. Rediker et al. (1964) however, assumed a constant field in the transition region. They have also pointed out the possibility of the formation of an 'hyperabrupt junction'. This junction is due to a large effective impurity density produced by large lattice mismatch, and can narrow the 'junction' at the appropriate forward biases to allow tunnelling to occur.

Thermally-assisted tunnelling model has also been proposed (Tansley, 1971; Rybka et al., 1975) to describe the conduction mechanism of anisotype heterojunctions. Tansley (1971) developed a model to allow the coexistence of thermal injection and tunnelling at high biases or temperatures. The doping density of the heterojunction is used as an adjustable parameter to fit the theory due to experimental results. This approach proved successful when applied to GaAs-InAs, GaAs-GaP alloys in heterojunctions. In the second case of Rybka et al. (1975), their model produced equations which applied well to the asymmetrically doped p^{+}Ge - nGaAs heterojunction they investigated.

Riben and Feucht (1966a) proposed a tunnelling-recombination model to describe the forward conduction characteristics and a Zener tunnelling model to describe the

reverse conduction characteristics of nGe-pGaAs heterojunctions. A parabolic band profile is assumed at the junction with the heterojunction asymetrically doped, so that the current is rate limited by pGaAs only. The current density equations derived are:

$$J_f = BN_t \exp[-4(2m^*q)^{\frac{1}{2}} (V_d - K_2 V_a)/3hH] \qquad (2.56)$$

for forward bias and,

$$J_r = (8q^2/ha^2)(-V_a) \exp[-4(2m^*q)^{\frac{1}{2}}(Eg_1 + \Delta Ev)^{3/2}/\{3\pi H(V_d - V_a)^{\frac{1}{2}}\}] \qquad (2.57)$$

for reverse bias.

The two equations differ only in the tunnelling potential, giving rise to a difference in the voltage dependence of J_f and J_r. To improve the correlation between the theoretical prediction and experimental results, Riben and Feucht (1966b) modified the two tunnelling-(recombination) models into multi-step tunnelling-recombination models (fig. 2.5). The forward current density is then given by:

$$J_f = \beta N_t \exp[-\alpha\theta^{\frac{1}{2}} (V_d - K_2 V_a)] \qquad (2.58)$$

where β and α are constants, $\theta^{\frac{1}{2}}$ varies linearly with temperature. In order that eqn. (2.58) functionally agrees with the experimental data, the energy level of the trap (below E_c), E_t, must be proportional to the square of the electric field in the transition region. The number of steps, R, to transverse the depletion region is defined as

$$R = (V_d - V_a K_2)/[\theta (V_d - V_a)] \qquad (2.59)$$

The reverse current density becomes

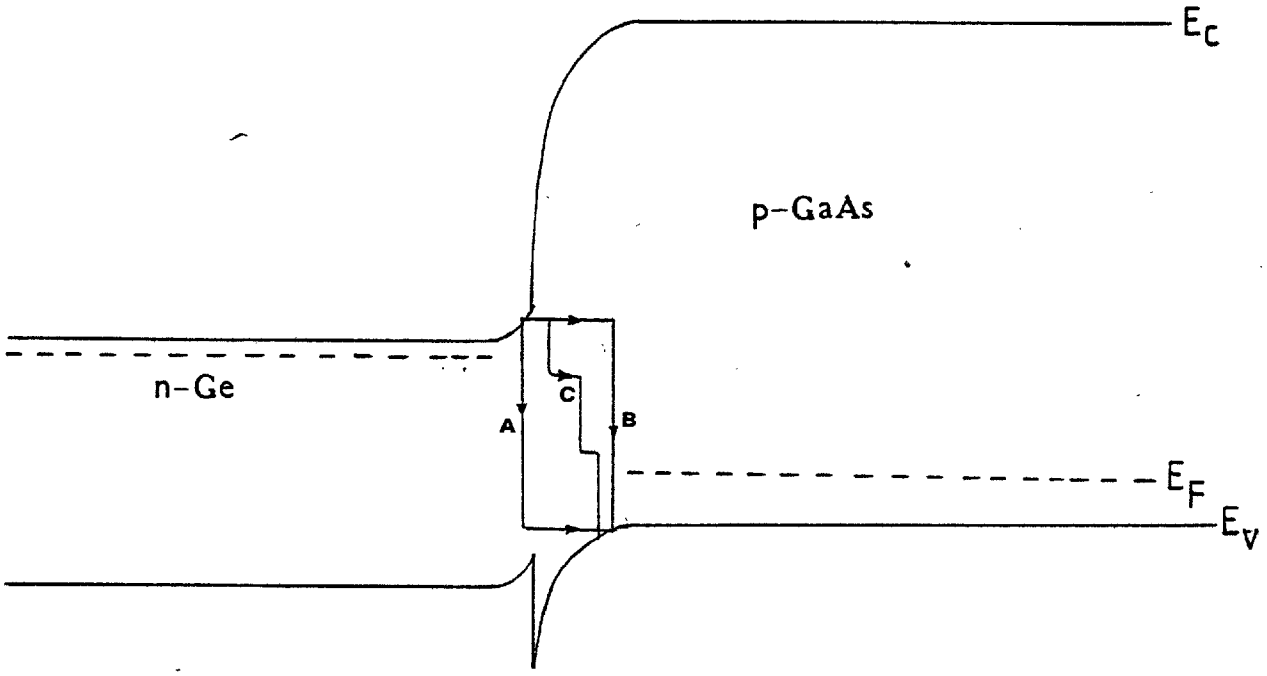

Fig. 2.5: Proposed Tunnelling Model for Forward Biased n-p Ge-AsAs Heterojunction
A, B and C are possible recombination-tunnelling paths (Riben and Feucht, 1966b)

$$J_r = (-q^2 a\, N_t V_a h^{-1}) \exp[-\alpha\, E_r^{\frac{1}{2}} (E_{g1} + \Delta E_v)(V_d - V_a)^{-\frac{1}{2}}] \qquad (2.60)$$

where E_r is the tunnelling barrier for each step and a is the lattice constant. Riben and Feucht (1966b) concluded that band diagram used by Anderson (1962) is applicable but thermal emission is not the dominant conduction mechanism, rather that tunnelling-recombination is the most probable mechanism.

The validity of proposed tunnelling models is supported by experimental data. Nonetheless, as many workers (e.g. Tansley, 1966; Riben and Feucht, 1966a and b) have pointed out, this does not preclude thermal emission. Instead, the coexistence of various conduction mechanisms is expected; each mechanism may dominate in some heterojunctions or within certain voltage/temperature ranges for other heterojunctions.

2.4 THE THIN FILM HETEROJUNCTION

2.4.1 Thin Film Effect

In the analysis done so far, heterojunctions are considered to have semi-infinite bulks. However, many heterojunctions are formed by having one or both semiconductors in thin film form. The thickness of the film becomes significant when it is comparable to its Debye length. Hipwood (1977) has shown that for a thin film heterojunction if a sufficiently high voltage is dropped across the film the field can be approximated by the voltage across the film divided by its thickness (fig. 2.6). This means that the film behaves like an insulator if the bias voltage is sufficiently high, also the voltage dropped across the film is smaller than that predicted by early analyses.

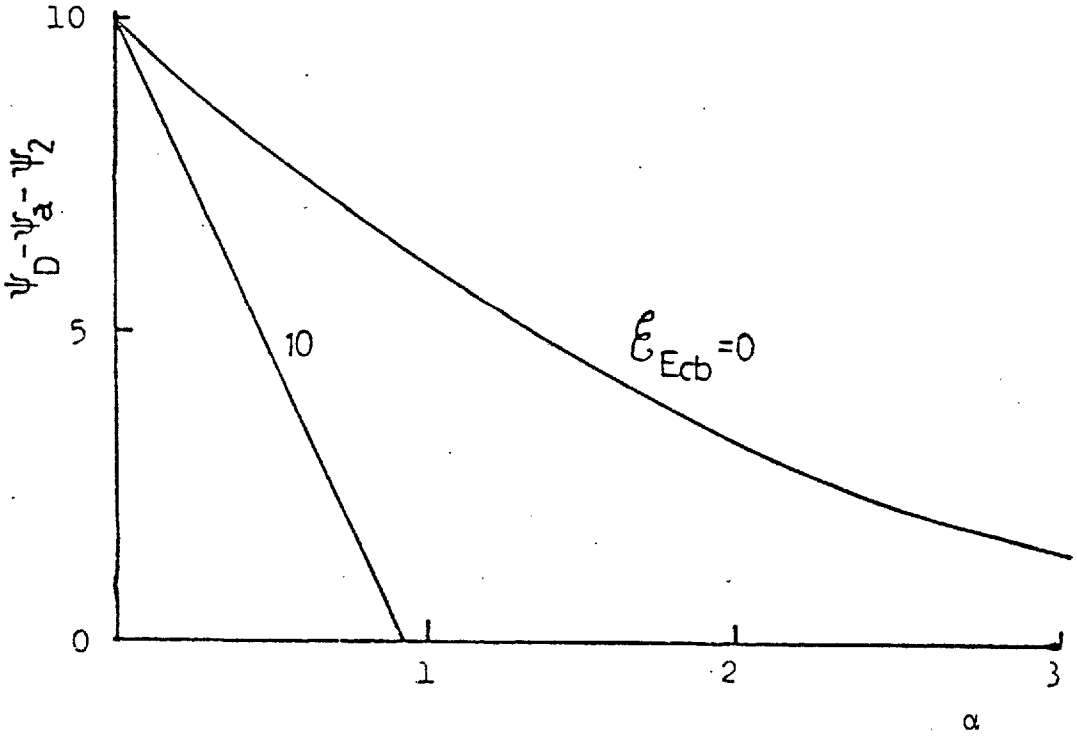

Fig. 2.6: Thin Film Effect - Film Thickness vs Potential across the Film (after Hipwood, 1977)

Jakubowski (1976) showed that for a thin polycrystalline semiconductor film the effective mobility and charged carrier concentration depend on the grain boundary barrier potential, the crystallite size and the depletion layer width (fig. 2.7). In the case where the crystallite width, W, is greater than the depletion-layer width, X_d, the effective mobility, μ_{eff}, can be expressed in the form:

$$\frac{1}{\mu_{eff}} \approx \frac{\bar{n}_k}{n_k} \frac{kN_c}{A^*T \exp(-\frac{q|\phi|_s}{kT})W} + \frac{\bar{n}_k}{n_k} \left(\frac{W-2X_d}{W} \right) \frac{1}{\mu_k} \qquad (2.61)$$

where, $\bar{n}_k$ -charged carrier concentration in the crystallites; n_k-carrier concentration of undisturbed regions of crystallites; ϕ_s-grain boundary potential, μ_k-mobility of undisturbed regions of crystallites and $A^*$is the Richardson's constant. In eqn. (2.61) the first term on the RHS represents the 'scattering' of carrier on potential barriers, and the second term is the 'scattering' in the undisturbed regions of crystallites. Also, the expression shows that $\mu_{eff} \approx \mu_k$ for large crystallites. For $W << 2X_d$,

$$\mu_{eff} \approx \frac{W^2 A^* T \exp\left[-\frac{1}{8}(W/L)^2\right]}{k L_D N_c \operatorname{erf}\left(\frac{W}{2\sqrt{2}L}\right)} \qquad (2.62)$$

In eqn. (2.62), μ_{eff} increases with the decrease of crystallite dimensions. In physical terms, this means that when the crystallites are very small the potential barriers become low enough to cease affecting the conduction process. Though the model proposed is a much simplified one, it does indicate

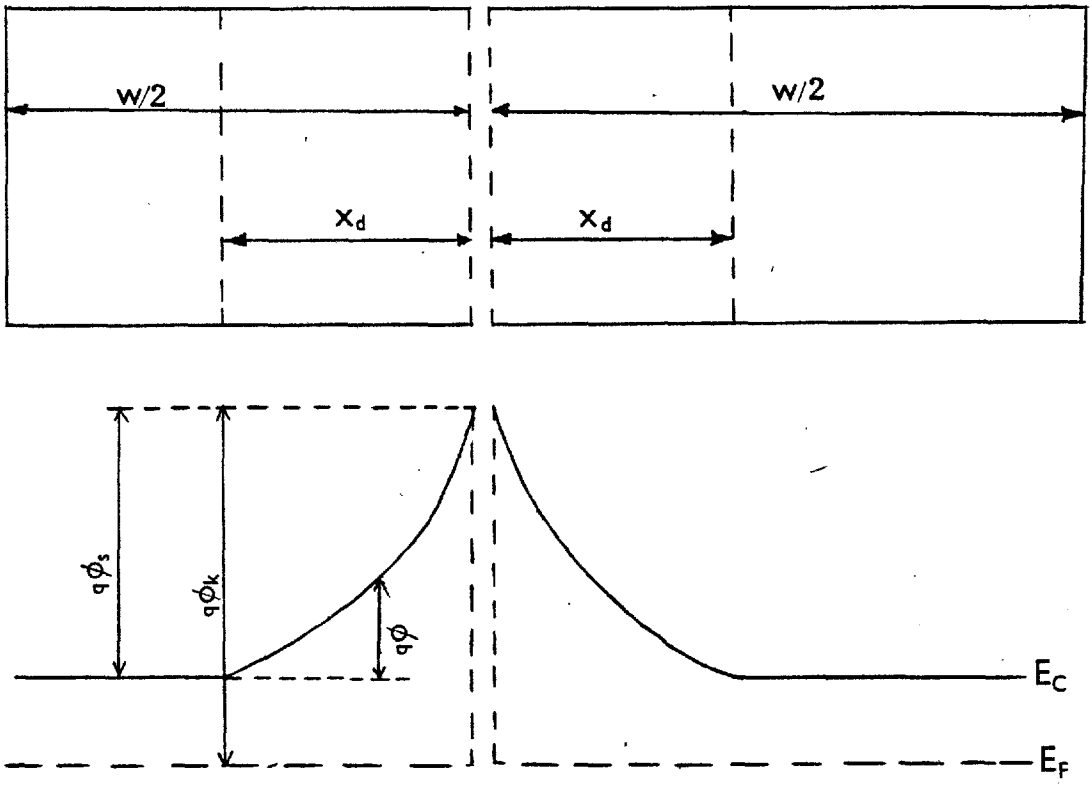

Fig. 2.7: Model of Two Potential Barriers on Crystallites Boundary (Jakubowski, 1976)

X_d - depletion region width, W-crystallites width

ϕ_s - potential barrier height from E_c (undisturbed region)

ϕ_k - potential barrier height from Fermi level, E_F

the complexity of the problem. The dependence of the mobility and consequently the conductivity, on the size of the grains and the nature of the boundaries of the crystallites means that the electrical behaviour of the film is directly related to the structure of the film which in turn is related to the conditions of preparation. Hence, in order to produce consistent results, the preparation conditions for the thin film must be as near invariant as possible.

Jerhot and Šnejdar (1970; 1974) have produced expressions for the potential distributions and capacitances of the space charge region of thin non-degenerate monocrystalline thin films. Three possible energy band profiles were considered (fig.2.8). The capacitance expression for fig. 2.8a proved to be extremely complex. Though expressions for fig. 2.8b and c are presented in shortened form they are by no means simple. However, the general cases can be approximated to a useable form when applied to specific problems. From the capacitance expressions Jerhot and Šnejdar (1976) have shown that for a thin semiconductor film with a thickness comparable or smaller than the effective Debye length, the space-charge capacitance at one surface is a function of the properties of second surface and also to the ratio of the film thickness to Debye length. We will consider a specific case of an n-type thin film with an energy band diagram similar to fig. 2.8c. Then, if the surface s_2 has a metallic contact, i.e. $\frac{d\psi_{s2}}{d\psi_{s1}} = 0$, the capacitance at the surface s_1 is

$$C_{sc1} = C_b \left[F_3(\psi_{s1}, E_o, \lambda)\right]^{-1} \left\{ \frac{1}{1+\lambda^{-2}} \left(1 - e^{-\psi_{s1}}\right)\right\} \quad (2.63)$$

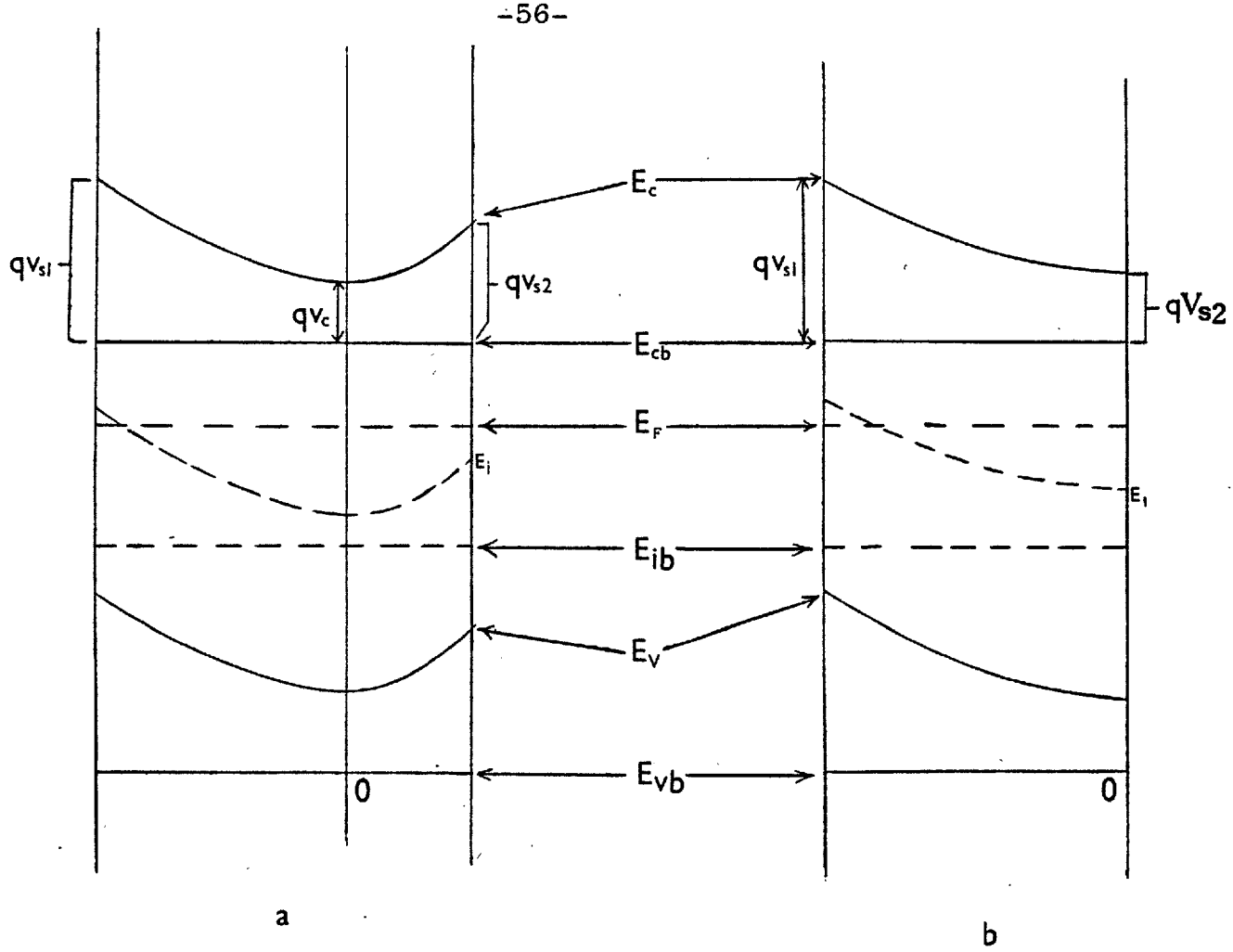

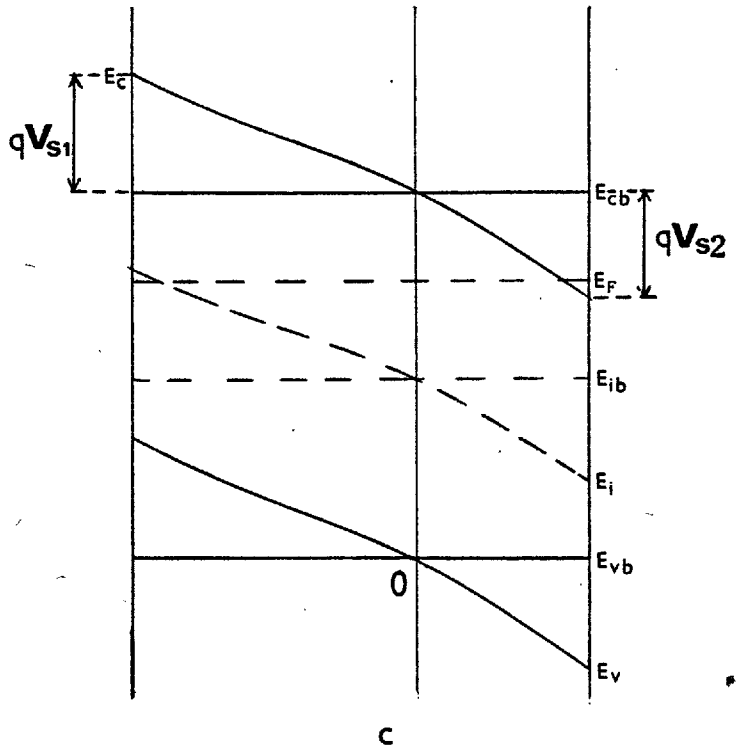

Fig. 2.8: Energy Level Diagram of Thin Film (Jerhot and Šnejdar, 1970)

(a) $\psi_{s1} > 0$; $\psi_{s2} > 0$; $\psi_{s1}\psi_{s2} > 0$

(b) $\psi_{s1} > 0$; $\psi_{s2} > 0$; $\psi_{s1}\psi_{s2} > 0$

(c) $\psi_{s1} > 0$; $\psi_{s2} < 0$; $\psi_{s1}\psi_{s2} < 0$

where

$$C_b = \varepsilon_1 \varepsilon_o / L_D \quad ; \quad \lambda = (n_b/p_b)^{\frac{1}{2}}$$

and

$$F_3(\psi_{s1}, E_o, \lambda) = \pm \{\frac{2}{1+\lambda^{-2}} (e^{-\psi_{s1}} + \psi_{s1} - 1) + E_o^2\}^{\frac{1}{2}}$$

Eqn. (2.63) is, in fact, a simplified form of the original equation (Jerhot and Śnejdar, 1976), with terms dropped by assuming (i) $n >> p$; (ii) $\frac{d\psi_{s2}}{d\psi_{s1}} = 0$.

The structural and thickness effect of thin semiconductor films are obviously significant, judging from the work done by e.g. Jukubowski (1976), Jerhot and Śnejdar (1970; 1974). The solutions are complex even after approximation. Normal analysis can sometime prove to be difficult and numerical analysis using a computer is required.

2.4.2 Junction characteristic of thin film heterojunctions

Two conditions can be considered:

(1) The thickness of the two films is greater than the depletion width.

(2) The thickness is of the order or less than the depletion width.

It is further assumed that the doping of the two films is about the same, and columnar crystallites are formed perpendicular to the substrate surface, hence few grain boundaries are encountered. Also the size of the crystallites is about the same.

Under (1) eqn. (2.61) can be approximated to the value of the bulk mobility when $W >> 2X_d$. For $W > 2X_d$, $\bar{n}_k \sim n_k$, this gives

$$\frac{1}{\mu_{eff}} \approx \left(\frac{W-2X_d}{W}\right) \frac{1}{\mu_k} + \frac{kN_c}{WA^*T} \exp\left(\frac{q|\phi_d|}{kT}\right) \qquad (2.64)$$

The second term, RHS of eqn. (2.64), is the boundary barrier scattering. This term can be neglected in practical applications because the crystallites are assumed to be columnar, i.e. the frequency of encountering any boundary barriers is relatively small.

Hipwood (1977) has applied the solution of Poisson's equation to a semi-infinite case of fig. 2.8c and has shown the potential distribution behaviour as (fig. 2.6):

$$Z = \sqrt{2}\,\{(\psi_D - \psi_a - \psi_o + \tfrac{1}{2}\bar{\varepsilon}_o^{\,2})^{\frac{1}{2}} - (\psi_o - \psi_a - \psi_2 + \tfrac{1}{2}\bar{\varepsilon}_o^{\,2})^{\frac{1}{2}}\} \qquad (2.65)$$

where $\bar{\varepsilon}_o$ is the electric field corresponding to a flat conduction band, i.e. $E_c = E_{cb}$.

For a double thin film heterojunction, eqn. (2.65) can be used as first order approximation, though the equation is derived for a monocrystalline film. This can be justified by neglecting any transverse current as small. Significant modification will be caused by image forces and interface trapped charged. Eqn. (2.64) can also be applied as the equation describes only the region of the film away from the junction.

In condition (2) potential distribution of the space charge region is nearly the same as in fig. 2.8c. Its equation is given by Jerhot and Šnejdar, (1970): as

$$\zeta = \int_{o}^{\psi_{s1}} \frac{d\psi}{F(\psi, \lambda)} \tag{2.66}$$

$$F(\psi_1, \psi_{s2}, \lambda) = \pm\{\frac{2}{1+\lambda^{-2}} (e^{-\psi} - 1 + \psi) + \frac{2}{1-\lambda^2} (e^{\psi} - 1 - \psi)\}^{\frac{1}{2}}$$

where ζ is the coordinate perpendicular to the surface measured in Debye lengths.

The first term on the right-hand side of eqn. (2.66) is the contribution from electrons, and the second term is that from the hole carriers, that is for an n-type film the first term would dominate the behaviour and vice-versa for a p-type film.

Consider an n-type film,

$$\zeta = \int_{o}^{\psi_{s1}} [\frac{2}{1+\lambda^{-2}} (e^{-\psi} + \psi - 1)]^{-\frac{1}{2}} d\psi$$

For large ψ, i.e. $e^{-\psi}$ can be neglected,

$$\zeta \sim \sqrt{2(1+\lambda^{-2})}\ [(\psi_{s1}-1)^{\frac{1}{2}} + 1] \tag{2.67a}$$

which is similar to eqn. (2.65) giving an insulator type potential.

For small ψ, where $e^{-\psi}$ can be expanded,

$$\zeta \sim (\bar{1} + \lambda^{-2})^{\frac{1}{2}} \ln \psi_{sl} \qquad (2.67b)$$

which is similar to eqns. (2.25) and (2.26). Thus, the potential distribution of a thin film does not vary significantly from the potential distribution of a heterojunction crystal, provided the thickness of the film is not smaller than the Debye length and the potential is not too large. Similar argument holds for p-type films.

2.5 SUMMARY

The complexity of the transport mechanism of the heterojunction when the effect of interface states is considered can be observed throughout the theoretical analysis of heterojunctions. Approximation has to be made from the theory in order to correlate with experimental results. Justification of approximation derived from the possible dominance of various factors (e.g. interface charge) in practice, thus simplifies the mathematics considerably.

CHAPTER 3

SPUTTERING AND SPUTTERED FILMS

3.1 DEFINITION

Sputtering of thin films involves the bombardment of a target composed of the required compound with gas ions, usually positively charged, which cause surface atoms to be ejected from the target. These ejected atoms are deposited onto the substrate which is usually placed closed to the target.

3.2 HISTORICAL REVIEW

This phenomenon has been known for well over a century and was used as a method for depositing thin films when vacuum pumps were too crude to be used for vacuum evaporation. With the advent of better pumps, vacuum evaporation became available and has been extensively used to produce thin films because the properties of the film obtained by sputtering were usually not reproducible. Subsequently, sputtering was used to investigate the physics of ion bombardment and the isolated phenomenon of gaseous discharge.

Renewed interest in using sputtering for the deposition of films was due to the increasing technological use of the refractory metal films for electronic applications. Requirement in this field led to the improvement in the qualities of sputtered films so that now their electrical properties are comparable with those produced by vacuum evaporation (Maissel, 1966).

3.3 THEORY OF SPUTTERING

Stark (1909) proposed that sputtering is due to direct transfer of momentum from bombarding ions to the atoms of the target. This theory is found to be more tenable than the 'hot spot' theory proposed by Crookes (1891) in which high local temperature evaporates target materials. The momentum transfer theory was supported by evidence found by various other workers (Berry et al, 1968; Maissel, 1966).

(1) Sputtering yields depend on the mass of the bombarding ions as well as on their energy.

(2) The sputtering yield is very sensitive to the angle of incidence of the bombarding ions.

(3) A threshold energy seems to exist, below which sputtering does not occur.

(4) Sputtered atoms have energies many times greater than thermally evaporated atoms (even from extremely hot sources).

(5) Atoms sputtered from single crystals tend to be ejected along directions of close packing.

(6) Sputtering yields decrease at very high energies probably because ion penetration below the surface and back scattering.

(7) Observation shows that sputtering is not produced by electron bombardment, even at very high electron energies.

(8) The sputtering process is independent of temperature, but it has been noted that sputtering yield decreases with increasing target temperature.

(9) The rate of secondary emission of electrons, emitted by bombardment of the target (i.e. the cathode) by the ions, is relatively low.

Modern theories (Berry et al, 1968; Maissel, 1966) of sputtering have been developed from the theory of radiation damage. These theories are statistical in nature and the sputtering process is considered to be based on two basic principles: (i) direct transfer of momentum, whereby atoms of target surface are ejected due to direct collision with the ions; (ii) indirect transfer of momentum in which the ions penetrate some distance into the target, displacing some lattice atoms (referred to as 'knock-on'). These knock-ons either further displace other atoms which diffuse onto the surface and emerge as sputtered atoms or themselves diffuse onto the surface and emerge as sputtered atoms. However, Politt et al, (1978) has proposed a new sputtering theory in which target atoms or molecules are electronically excited to reduce their bonding energies and subsequently ejected from the target. Their theory includes momentum transfer as secondary effect.

3.4 SPUTTERING CONDITION

An 'abnormal' glow discharge is commonly employed during sputtering (N.B. an abnormal glow is achieved when the increase in voltage drop across the discharge corresponds to an increase in cathode current density, Berry et al, 1968) as normal glow represents the minimum

conditions under which sufficient secondary electrons are generated to replace those lost to the anode or to the walls of the sputtering chamber (fig. 3.1). Thus to obtain an effective growth rate by sputtering, it is necessary to increase both the sputtering yield and the collision rate of the ions with the target which means that productive sputtering occurs in abnormal glow conditions.

Most of the ions required to maintain secondary emission from the target are produced in the negative glow region. Hence, any object which restricts the volume of the negative glow region affects the sputtering rate (Berry et al, 1968). Thus, the application of a magnetic field or the use of a secondary electron source to enhance the ionisation rate has been widely employed. This method is preferred at low pressures. Sputtering at high pressure leads to problems associated with back-scattering and gas inclusion during deposition (Francome, 1963), the film is also subjected to intense electron bombardment which may lead to film damage.

The gas used in producing the plasma is usually a chemically inert gas with a suitable ionic mass; the most commonly used being argon which has also been used in this work. A chemically inert gas is used to avoid unwanted chemical reactions during the sputtering process. In this work, the backing pressure of the system was about 10^{-6} torr and the argon pressure during sputtering was $5\text{-}6 \times 10^{-3}$ torr.

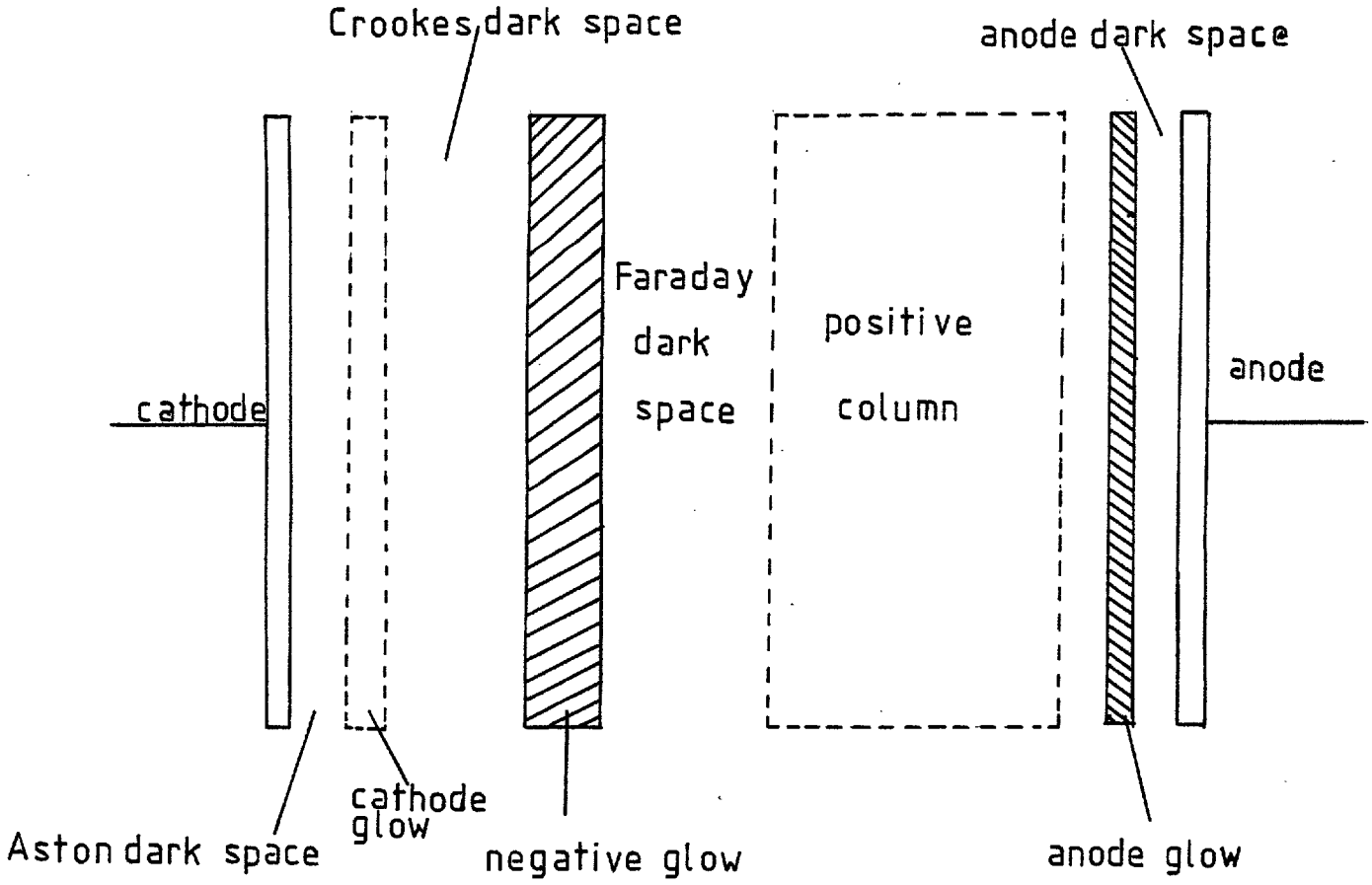

Fig. 3.1: Principal Regions in a Low-Pressure Glow Discharge

3.5 DEPOSITION RATE

The deposition rate of a material is given by

$$Q = C I \gamma \qquad (3.1)$$

where Q is the deposition rate, C is a constant which characterises the sputtering apparatus, I is the ion current, and γ is the sputtering yield. (Berry et al, 1968).

The ion current depends on the gas pressure but variation of the gas pressure has several other effects on the deposition rate (Berry et al, 1968; Maissel, 1966).

(i) If the gas pressure is increased the ion current also increases. However, this current causes a back EMF which decreases in the applied voltage and, hence, the energy of the ions.

(ii) Increase in gas pressure increases the collision rate of the ions with the gas molecules. Although this effect increases the number of ions striking the target at an oblique angle, and so apparently increasing the sputtering yield, the energy of these ions is reduced by the collisions with gas molecules. Thus the effective sputtering yield decreases.

(iii) At high pressure probability of sputtered atoms being back-scattered by the plasma to the target increases.

The substrate should be as close to the target as possible to obtain the maximum sputtering rate for a given set of conditions without disturbing the Crookes Dark Space. Any local interference with Crookes Dark Space decreases the number of ions striking the target locally,

causing a thinner film to be deposited onto the substrate. in this area. Thus there is an optimum pressure and voltage for any system to obtain a maximum sputtering yield.

3.6 R.F. SPUTTERING

R.F. sputtering is used because both CdSe and CdTe targets are highly resistive, thus rendering d.c. sputtering difficult.

The basic principle of r.f. sputtering is to apply a high voltage r.f. signal between the anode and cathode so that they interchange polarity at field frequency. More electrons strike the target (the cathode) and the anode in the positive cycle than do ions in the negative cycle, creating a net d.c.'offset potential' accumulating on the target, since the anode is conductive and does not retain charge. The overall effect is that the target is bombarded with ions (Leveson, 1973). Since the target is not insulating, a d.c. blocking capacitor is used in series with it to prevent any charge leakage (fig. 3.2).

3.7 SPUTTERED FILMS

3.7.1 Adhesion of Sputtered Films

The problem of the adhesion of thin sputtered films onto the substrate has received little attention. Most data available is related to the adhesion of evaporated films. However, it is generally accepted that clean substrates are required in order to produce a good adhesion between the film and the substrate. Also, films of high melting point materials in general adhere to the substrate more strongly than those of low melting point (Maissel, 1966).

It appears, however, that sputtered films in general adhere more strongly than evaporated films because the incident ions are more energetic than the atoms deposited during evaporation, and, thus, can penetrate into the substrate or dislodge contamination from its surface (Maissel, 1966).

3.7.2 Contamination of the Sputtered Films

The presence of a high vacuum better than 10^{-6} torr before admitting sputtering gas is essential to eliminate any active gases in the chamber. Nonetheless, contamination can still arise from other sources. Thus Berry et al (1968) and Maissel (1966) list the following: (i) vapours may desorb or outgas from the walls of sputtering chamber and other structures in the chamber. These contaminants can be active gases (e.g. O_2) water vapour or hydrocarbons backstreaming from the diffusion pump. They are more active in sputtering than in an evaporation because they can be ionised or in the case of hydrocarbons, they can be cracked into other compounds which subsequently ionise. The problem can be reduced by presputtering the target before deposition, and also leaving the chamber full of argon after the sputtering so that any gas adsorbed by the walls other structures in the sputtering chamber, is predominantly argon; (ii) sputtering pressure is relatively high and can cause backstreaming of pump oil from the diffusion pump during the sputtering run.

This source of contamination can be avoided by partially closing the Baffle valve to reduce vapour diffusion; (iii) the substrate surface may be contaminated by active gas absorbed onto the substrate. They can be removed by heating the substrates at a high temperature (300^{o}C) for a minimum period of one hour.

3.7.3 Properties of Sputtered Films

This section will be devoted to the properties of sputtered semiconductor films as films of this type are used in the devices considered later.

Very little work has been published on semiconductor films deposited by sputtering, despite the fact that better stoichiometry can be obtained in sputtered semiconductors than in evaporated films.

The physical structure of the semiconductor film depends on the following factors:-

(i) Substrate: Single crystal substrate with a similar crystal structure and lattice parameter to the deposited compound can induce epitaxial growth of the thin film, whereas amorphous substrate can only produce either highly polycrystalline or amorphous films.

(ii) Substrate temperature: The thin film formed can either be large grain polycrystalline film or single crystal film depending on the substrate temperature. Higher substrate temperatures enable the depositing atoms/molecules to arrange themselves in the lowest energy sites, thus producing a better crystalline structure in the film. Normally, the substrate temperature during

sputtering is between 200-400°C.

The physical structure of the sputtered film influences its electrical properties. Both amorphous and polycrystalline films have a higher resistivity than the same bulk material, and the conduction mechanisms can also be different (e.g. hopping and defect conduction), due to the high density of defects. Expitaxial thin film exhibits resistivity similar to its bulk counterpart.

Thickness of the film can also affect the electrical properties of the film. If it is of the order of the mean free path of the electron, then the carrier can undergo either diffuse (inelastic) or specular (elastic) scattering from the film surface, depending whether the film is polycrystalline or single crystal (Chopra et al, 1963).

CHAPTER 4

PROPERTIES OF CdTe AND CdSe - RESUME

4.1 CRYSTAL STRUCTURES

The crystal structures associated with II-VI compounds are cubic (zincblende) and hexagonal (wurzite) (fig. 4.1). The bonding in these compounds is a mixture of ionic and covalent. The ionic characteristic increases as the atomic weight decreases, i.e. from HgTe to ZnS (Ray, 1969). The lattice arrangements of wurzite and zincblende are nearly the same, out to and including the next-nearest neighbour where the only difference is the distance to the centre. For wurzite, the atoms of the nearest- and next-nearest neighbours may not have the same distance from the reference centre, depending on $U(\approx^3/8)$ (see section 4.1.2), whereas in zincblende, all the atoms of the nearest and next-nearest neighbour are at equal distance from the reference centre. The closely packed planes of wurzite and zincblende are (0001) and (111) with the stacking axis along [0001] and [111] direction respectively (Aven and Prener, 1967).

4.1.1 Cadmium Telluride

CdTe at normal temperatures and pressures crystallises in the cubic zincblende structure. Each Cd(Te) has four nearest-neighbours of Te(Cd) at a distance of $\sqrt{\frac{3a}{4}}$, where a is the lattice parameter, lying at the corners of a regular tetrahedron.

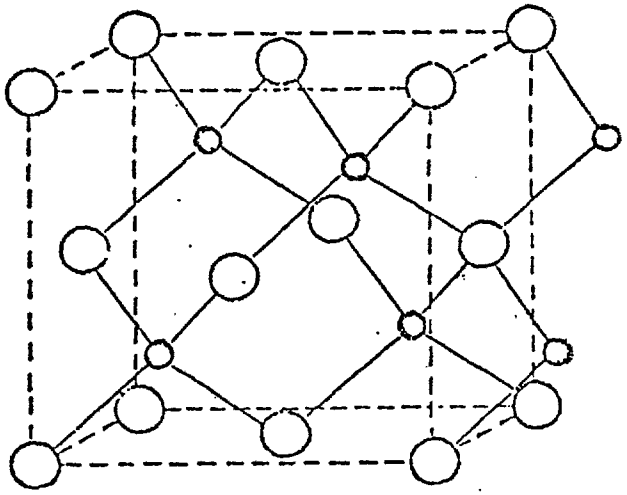

a. Zincblende

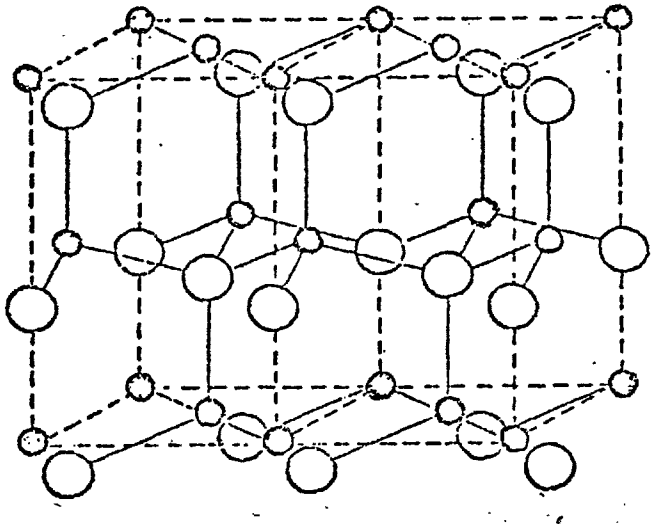

b. Wurzite

FIG. 4.1

Like other zincblende crystals, CdTe does not have a centre of symmetry or inversion, consequently it is polar and opposed (hkℓ) faces, and opposed [hkℓ] and [$\bar{h}\bar{k}\bar{\ell}$] direction may have different physical and chemical properties. Hence, CdTe is piezoelectric. The Cd and Te ions of opposite polarity can be visualised as forming a network of permanent dipoles.

Impurities like Cu, Ag, Au, In diffuse into CdTe with relative ease (Aven and Prener, 1967). Column I elements in the periodic table (Au,Ag,Cu) substitute for the cations and give rise to deep acceptors, whereas In acts as a donor. An energy band diagram giving the significant impurities energy levels was introduced by De Noble (1959) and is given in fig. 4.2.

4.1.2 Cadmium Selenide

Both cubic and hexagonal forms of CdSe are known. Crystals grown at high temperature have a wurzite structure whereas the zincblende modification is formed by precipitation from solution at room temperature (Aven and Prener, 1967). However, the cubic form is metastable, and partial conversion to the hexagonal form takes place upon heating at 130°C, and the transformation is complete after heating at 700°C for 18 hours (Pashinkin et al, 1962). There are two molecules in the hexagonal unit cell : Cd at 0,0,0; $^1/_3$, $^2/_3$, $^1/_2$ and Se at 0, 0, U; $^1/_3$, $^2/_3$, $^1/_2$ + U (U ≈ $^3/_8$). Each Cd atom is bonded to four Se atoms which are sited approximately at the corners of a tetrahedron, one at distance uc and three at $\left[{}^1/_3\ a^2 + c^2\ (U-{}^1/_2)^2\right]^{\frac{1}{2}}$, where a

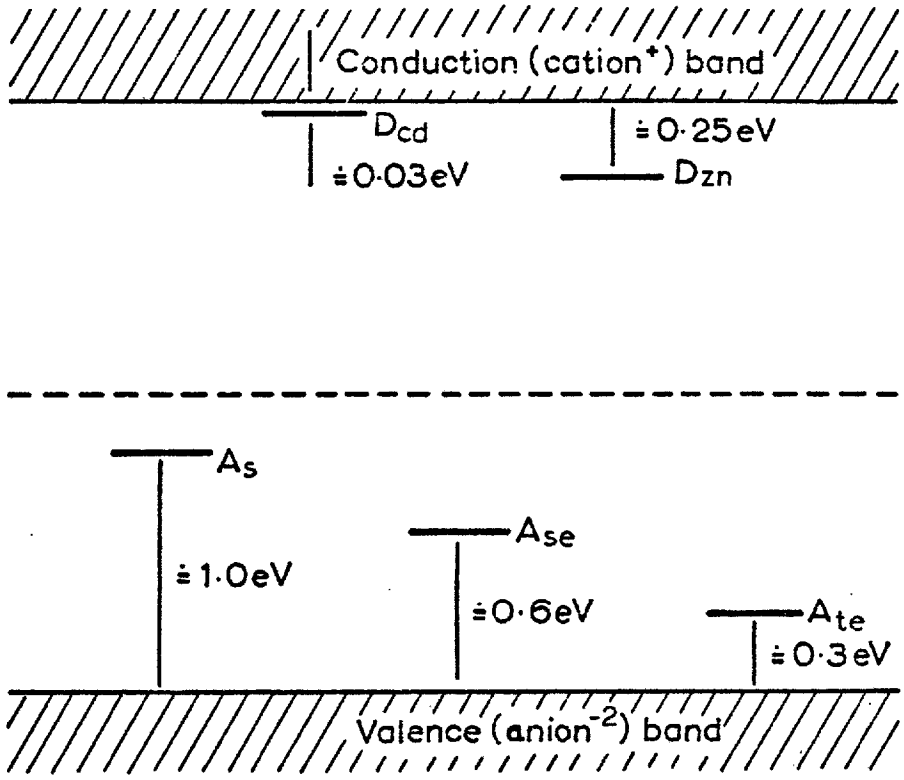

FIG.4.2a : Summary of characteristic donor and acceptor energy levels in ii and vi compounds
(After BUBE - 1960, p.171)

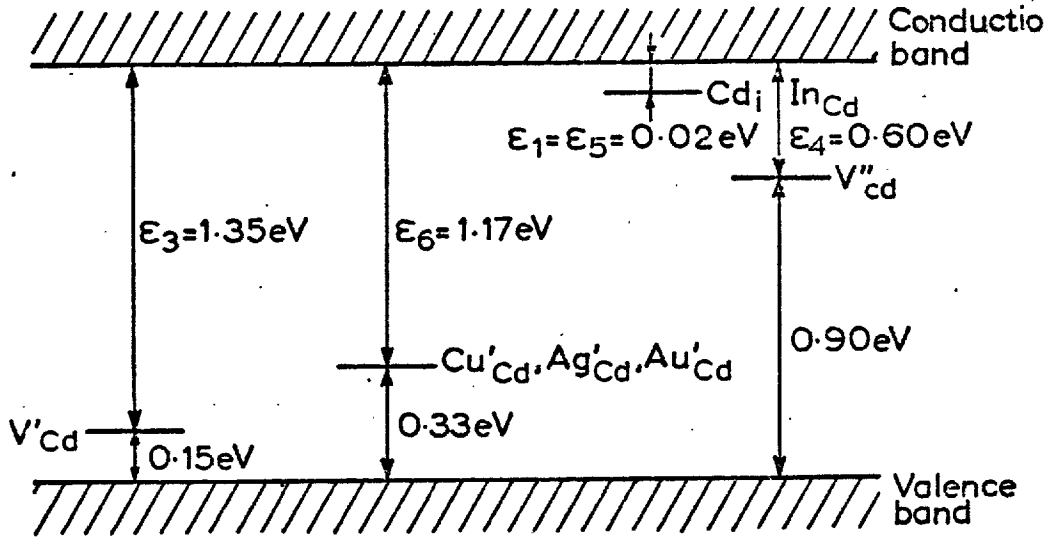

FIG.4.2b : Electronic energy-band scheme of CdTe, giving the room-temperature values of the thermal ionization energy of the various centres.

and c are the lattice parameters along a- and c-axes. CdSe, like other wurzite crystals, has no centre of symmetry, with a polar axis parallel to $[000\bar{1}]$. As in CdTe, a network of permanent dipoles exists in CdSe. But in wurzite, these moments are not balanced but align along a single polar axis, and the material is therefore both piezo- and pyroelectric (Aven and Prener, 1967).

Impurities in CdSe behave in a very similar way to those in CdS. For example, chemisorbed oxygen acts as acceptor and can increase the height of the boundary potential barriers between crystallites of both CdSe and CdS. Various traps and recombination centres are described in Ray (1969).

Some of the physical properties of CdTe and CdSe are listed in table 4.1.

4.2 ELECTRICAL AND OPTICAL PROPERTIES

4.2.1 Cadmium Telluride

CdTe can be doped both p- and n-type. The minimum in the conduction band was found to be at $\underline{k} = 0$. (Aven and Prener, 1967). Hall mobility of both n- and p-type CdTe was also investigated (Aven and Prener, 1967). p-n homojunctions in CdTe have also been investigated for electroluminescence (Ray, 1969).

CdTe has a band gap which should prove an optimum for photovoltaic solar energy conversion and it has the added advantage of being the only II-VI compound that can be doped to produce either conductivity type. However, the efficiency of single crystal photovoltaic homojunctions is severely limited by poor minority carrier lifetime ($\lesssim 10^{-11}$ sec). The photovoltaic performance of polycrystalline

TABLE 4.1

PROPERTY	CdTe	CdSe
Effective mass of electron m_e^*	$0.096 \pm 0.005m$	0.13m
Effective mass of hole m_h^*	$0.35 \pm 0.05m$	1m 0.45m
Mobility of electron	$700\ cm^2V^{-1}Sec^{-1}$	$650\ cm^2V^{-1}Sec^{-1}$
Mobility of hole	$65\ cm^2V^{-1}Sec^{-1}$	$20\text{-}50\ cm^2V^{-1}Sec^{-1}$
Band gap at 300^oK	1.4 eV, 0.863 micron	1.72 eV, 0.72micron
dEg/dT	$(2.3\text{-}5.4) \times 10^{-4}$ eV/°K	4.6×10^{-4} eV/°K
Static dielectric constant	11	9.33 10.2
High frequency dielectric constant	7.21	6.05 5.96
Electron affinity	4.28 eV	4.95
Lattice constant	6.481 Å	6.077 Å (cubic)

film cells and the single crystal cells do not appear to be very different (Aven and Prener, 1967).

4.2.2 Cadmium Selenide

CdSe is always n-type and the mobility of the electron is generally found to be between 390-900 cm^2/V-sec. Its effective mass found by optical measurement is anisotropic (Aven and Prener, 1967). In intrinsic CdSe, the carriers are provided by native defects, e.g. excess cadmium atoms give rise to interstitial cadmium atoms which act as a donor giving n-type conductivity.

CdSe is not generally used at present in any photovoltaic devices except in the form of alloy or hetero-junction as $Cu_{2-x}Se$-CdSe. Photoconductivity experiments revealed that CdSe has a photosensitising centre with an hole ionisation energy of 0.6 eV (Aven and Prener, 1967). A series of traps in semi-insulating CdSe characterised by thermally stimulated current experiments were listed by Kindleysides and Woods (1970).

4.3 THIN FILM CdTe AND CdSe

Thin films of II-VI compounds can be prepared by several methods but thermal evaporation and sputtering are most widely used. Holt (1974) has reviewed the general condition for the growth and structure of epitaxial II-VI films where he showed that reproducible epitaxy can be obtained within a range of substrate temperatures (200-500°C) which depend on growth conditions. Sputtered films are discussed in section 3.8.3.

4.3.1 Cadmium Telluride

CdTe films evaporated onto single crystal substrates (e.g. mica, NaC , KCℓ) form crystals with mixed hexagonal-cubic structures (Aven and Prener, 1967). For the sputtered film, however, columnar growth is observed (Pawlewicz et al, 1976) when the substrate (in this case Mo and fused quartz) temperature is greater than 250°C. Pawlewicz also found that the CdTe film he obtained through sputtering was highly faulted, semi-insulating electrically and the fundamental properties of the film were governed by the condition of preparation, e.g. gas pressure and substrate temperature. Typical resistivity found for the near-stoichiometric films is between 10^6-10^8 Ω cm.

4.3.2 Cadmium Selenide

Glew (1977) has d.c. sputtered undoped CdSe film (thickness 0.4 - 4 μm) in a mixed atmosphere of H_2Se and Ar or in pure Ar. He showed that CdSe films grown on indium-tin oxide coated soda glass slides have an hexagonal phase predominating, and other films sputtered in argon were less disordered than those sputtered in the H_2Se-Ar mixture. It was noted however that a cubic phase was observed in some CdSe films sputtered at 800°C. Variation of the film resistivity normal to the surface against film thickness and substrate temperature was investigated. It was found that the highest dark resistivity was ∿6 x 10^9 Ω cm with film thickness of ∿1.5 μm, deposited substrate temperature of ∿150°C. Resistivity in the light remained relatively constant, 10^6 Ω cm (Glew, 1977).

Chan and Hill (1975) have pointed out that the conflicting reports on the electrical properties of CdSe films arise mainly due to differences in the conditions of preparation. For evaporated CdSe films, the stoichiometry of the film was changed from Cd rich to Se rich as deposition rate and substrate temperature increased (Chan and Hill, 1975). Conductivity in evaporated n-CdSe films was found to be complex and involved various mechanisms, typically conduction limited by intercrystalline potential barrier scattering may dominate at temperatures above 273^{o}C and impurity conduction (e.g. hopping) may dominate at temperatures below 273^{o}K (Chan and Hill, 1976).

An electrical model consisting of resistors and diodes was proposed by Kuźnicki (1976) to describe thin polycrystalline CdSe films. He modelled the barrier region as a back-to-back diode connected by a linear resistor,(fig. 4.3a). By assuming the resistance along the grain barrier is linear, and that across the barrier is non-linear, an electrical model was built. It formed an elementary cell of the thin film (fig. 4.3b). The model is analysed numerically and the theoretical results agreed with the experimental values.

Various models have been proposed in an attempt to describe the electrical properties of the thin films affected by structure or impurities, e.g. potential barriers due to grain boundaries or stacking faults (Glew, 1977; Holt, 1974) can dominate the electrical characteristics. Experimental results showed that two or more conducting mechanisms can be responsible for the electrical characteristics of a thin film. (Chan and Hill, 1975). Hence, interpretation of

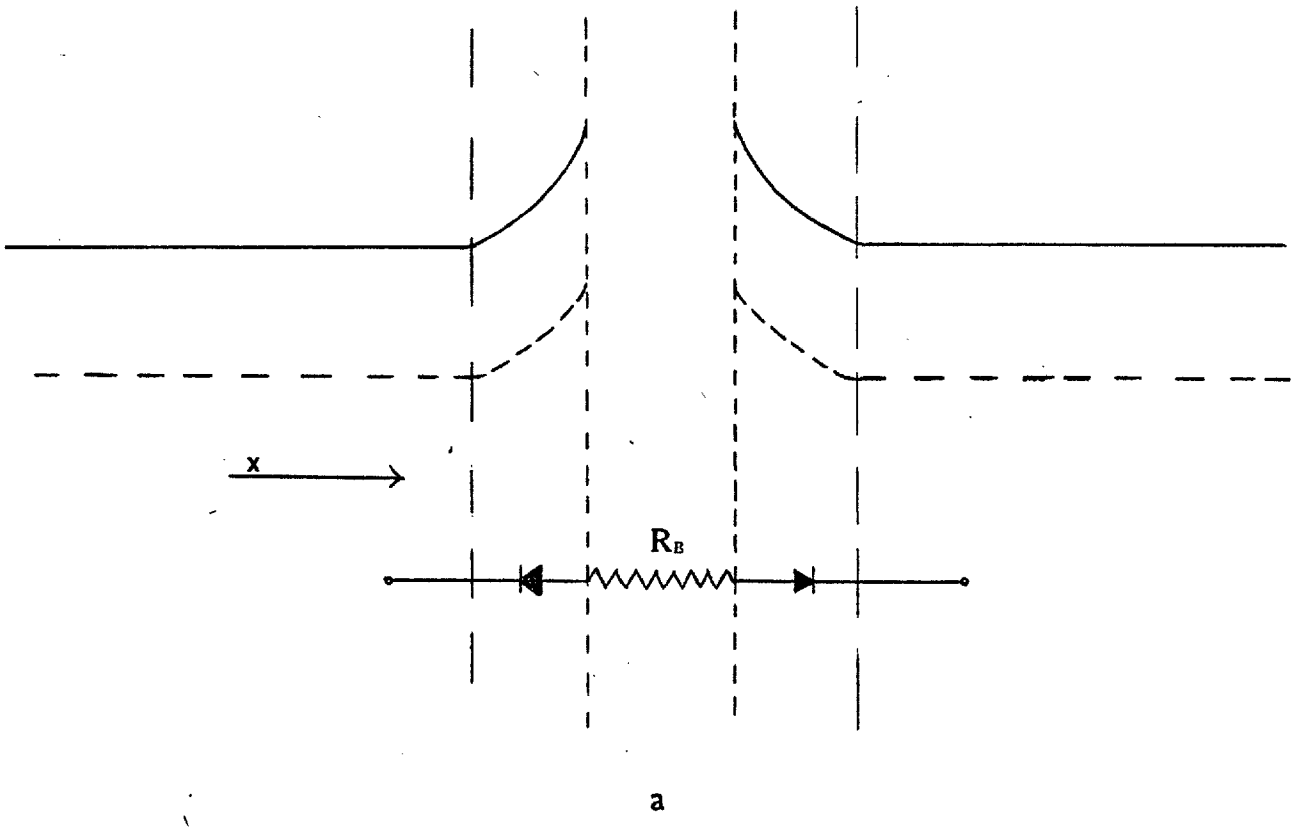

a

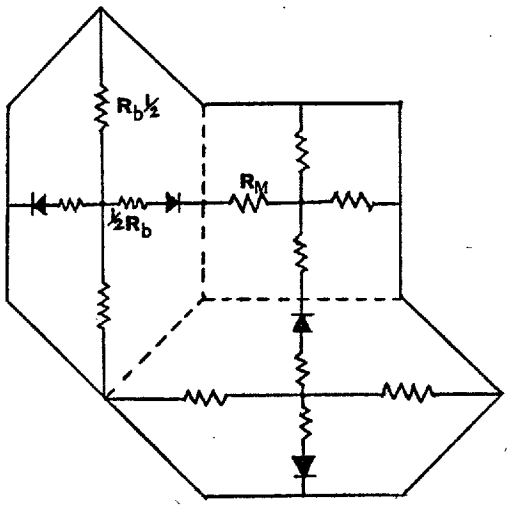

b

Fig. 4.3: Electrical Model of Polycrystalline CdSe Films (Kuźnicki, 1976)

(a) Equivalent circuit of the barrier region

(b) An elementary cell of the electrical model

R_m - resistance of the crystallites

R_b - resistance of the barrier

experimental results may be difficult.

4.4 pCdTe-nCdSe HETEROJUNCTIONS

By applying Anderson's theory (1962), an energy band diagram for the pCdTe-nCdSe heterojunction has been proposed by Sadek (1975) (fig. 4.4). The band diagram was supported by the results of photovoltaic experiments (Sadek, 1975; Cheah, 1976). However, these results do not imply that the thermal emission model can be applied. (Riben and Feucht, 1966). The lattice mismatch, calculated using the method introduced by Holt (1966), of the heterojunction is found to be of the order of 7%. Tansley (1971) has pointed out that lattice mismatch greater than 4% in any thin film, of thickness greater than a monolayer, would induce the formation of dislocations with only 4% of the misfit accommodated in strain. Therefore, it seems that pCdTe-nCdSe heterojunction would have a damaged interface with possibly a network of dislocation spreading across the junction.

Two properties can affect the heterojunction characteristic significantly: (i) the bulk properties of the two semiconductors - native defects and dopants can dominate the electrical and optical properties of the semiconductors. In addition in polycrystalline films, the occurrence of extended defects can further affect the conduction mechanism of the semiconductors; (ii) the junction characteristics can also be dominated by the high density of traps arising from dislocations and other defects at the interface (cf. section 2.3).

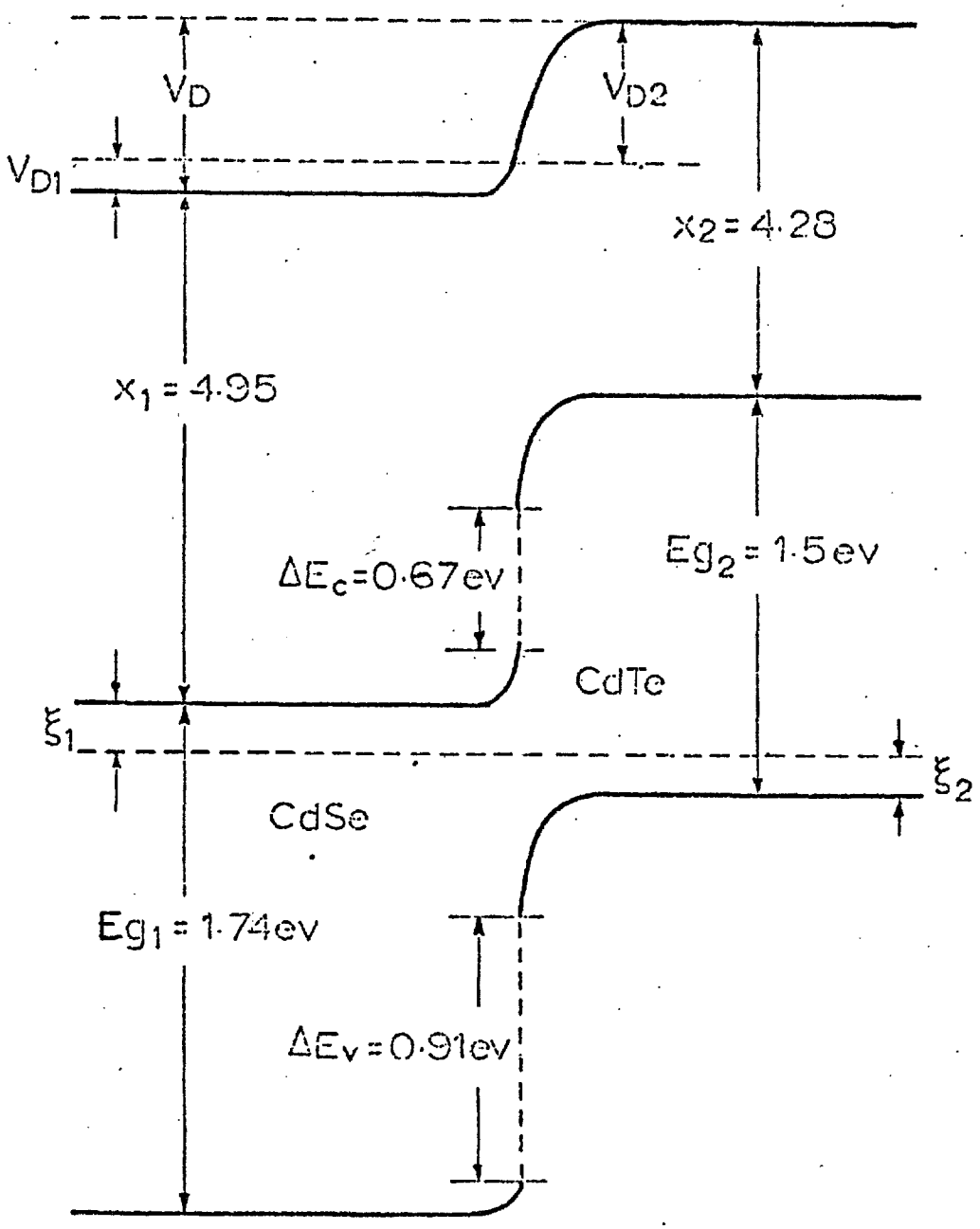

FIG. 4.4: Energy band diagram for p CdTe - n CdSe hetero-junction. (after Sadek, 1975)

If one or both semiconductors are thin films then structural defects formed during growth will dominate the properties of the heterojunction. Thin film effects (cf. section 2.4) can dominate the properties of the heterojunction which may largely depend on the way the device is prepared. For a 'through' film device, the conduction path may or may not encounter a number of intercrystalline potential barriers. But for an in-plane film device where the conduction path has to transverse one of the semiconductors, more barriers and defects are likely to form obstacles along the path. Under these conditions the electrical and optical properties could be dominated by the structure of the semiconductor film.

CHAPTER 5

EXPERIMENTAL PROCEDURES AND DEVICE FABRICATION

5.1 PREPARATION PROCEDURE

The layers of the heterojunction were deposited by r.f. sputtering of the compounds in an atmosphere of pure argon. Firstly the n-CdSe was sputtered onto the substrate at a temperature of 250°C, and the process was repeated with a CdTe target to obtain the film of the second semiconductor.

5.1.1 Sputtering System

The layout of the system is shown in the block diagram in figure 5.1. The power unit generated a r.f. signal at a frequency of 13.86 MHz. This signal was fed into a Heathkit SB220 power amplifier. The power output from the amplifier was connected to the target in the sputtering chamber through a matching unit. The power output and matching could be monitored by a Heathkit power meter HM 102. The substrate was mounted facing downward and earthed (fig. 5.2). Heating for the substrate was provided by a grid of Molydenum wires threaded inside the substrate holder. The sputtering chamber also had a shutter to facilitate pre-sputtering and a thermocouple to monitor the substrate temperature which was controlled by an Ether 'Mini' (type 17-90B) temperature controller. The vacuum pump consisted of a rotary pump (Speedivac, ED35), and oil diffusion pump with a cold trap.

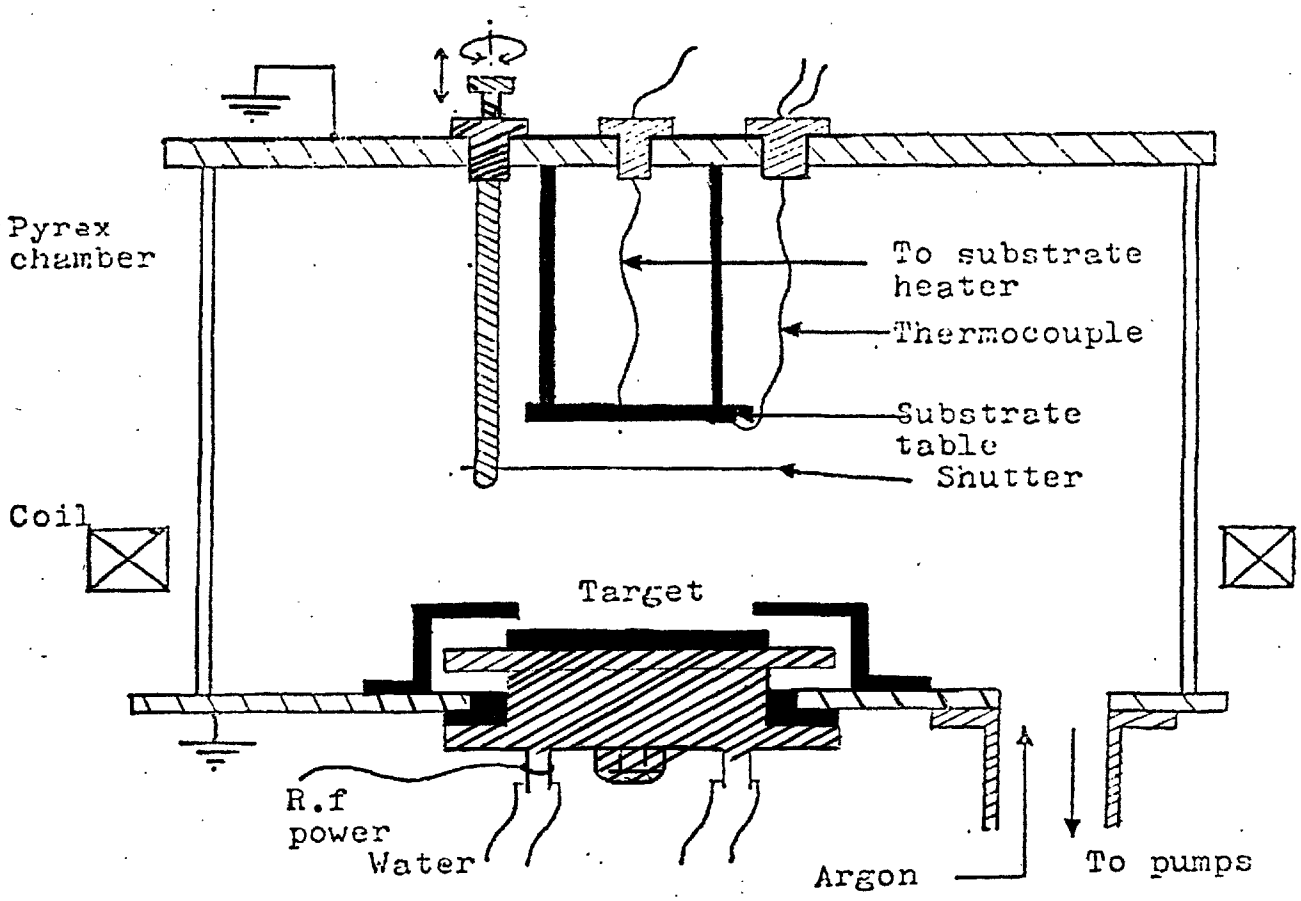

Fig. 5.1 Schematic Diagram of The Sputtering System
(After Hipwood, 1976)

The target has a diameter of 5 cm, a thickness of 2 mm and was water-cooled during sputtering. The target to substrate distance was usually held at 7.5 cm.

5.1.2 Sputtering Procedure

The background pressure of the sputtering chamber was $\leq 1 \times 10^{-5}$ torr, and the argon pressure during sputtering was maintained at $\sim 5 \times 10^{-3}$ torr to give an optimum sputtering rate. The sputtering power was 200 watts. The substrate temperature was kept at 250°C during sputtering. Before sputtering commenced, the target was first pre-sputtered for half an hour by placing the shutter between the target and the substrate. A ring electromagnet was used to confine the plasma to enhance the sputtering rate.

After sputtering the substrate was slowly cooled at 1° per min to minimise any possible mechanical damage due to differences in thermal expansion coefficients. The sputtering rate was found to be of the order of 0.25 μm per hour. The average thickness of the sputtered films was 1 μm. and was determined by using Talysurf 4 (Taylor-Hobson).

5.1.3 Substrate and Contacts

A soda glass microscope slide was used as a substrate. The substrate was chemically cleaned by using organic solvents (Trichloroethylene, Acetone and Absolute Alcohol) and by subjecting the substrates to ultrasonic vibration. The substrate was then mounted onto the substrate table (fig. 5.2).

ITO (Indium tin-oxide) was sputtered onto the soda glass slide to act as ohmic contact to n-CdSe film. The resistivity of the ITO film was found to be 50-100 Ω per unit

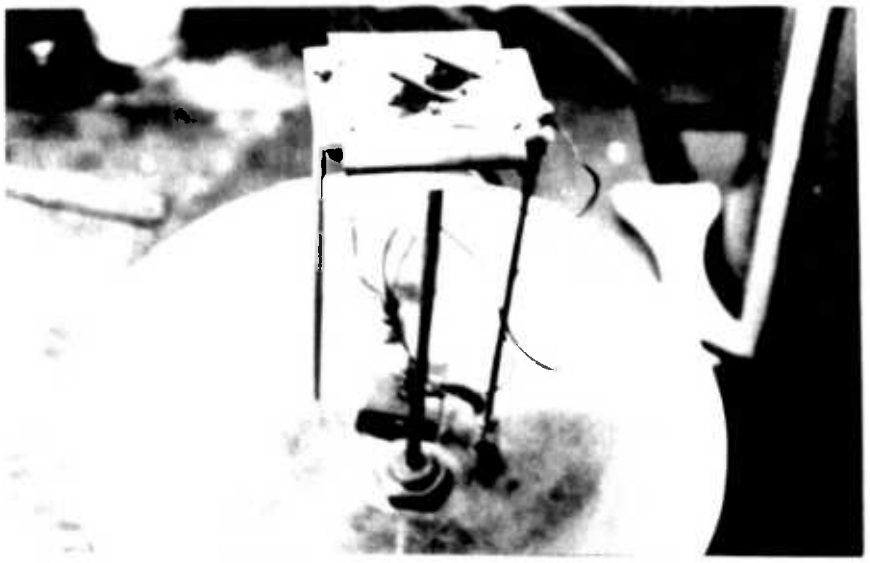

Fig. 5.2 Substrate Mounter of the Sputtering System

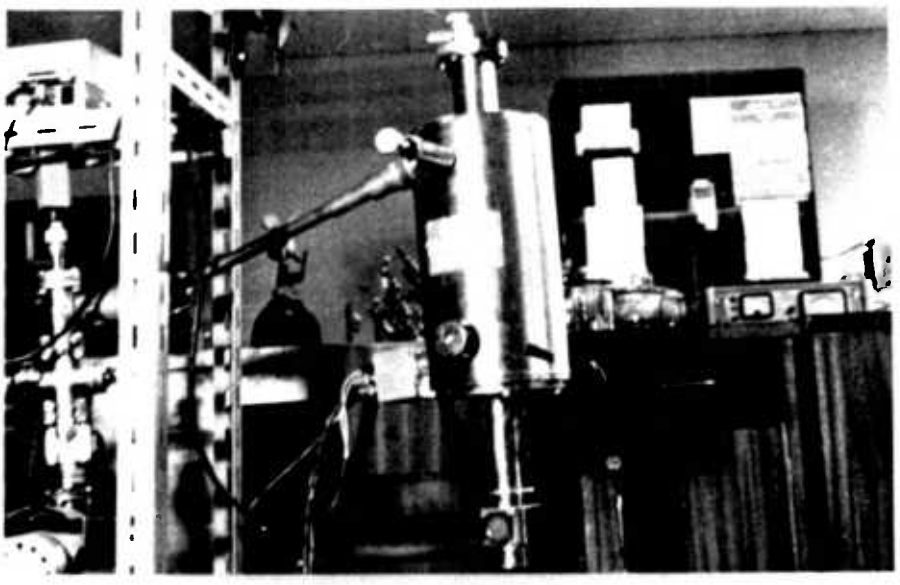

Fig. 5.3 Cryostat used for Temperature Variation Measurements

square for a thickness of the ITO film of 1000Å and gave an 80% transmission of light with a wavelength 0.5 μm to infra-red. The film structure is polycrystalline but with a considerable amount of preferred orientation {100} in the cubic {100} (Vossen, 1971).

Gold was evaporated through a mask onto the pCdTe to make ohmic contacts. The contacts which were circular had an area of 3.3×10^{-3} cm^2.

5.2 EXPERIMENTAL PROCEDURES

5.2.1 Current-Voltage Measurement

Current-voltage measurements were made for applied d.c. and a.c. as a function of temperature. The cryostat used was made by BOC and was of the double jacket type (fig. 5.3) with the inner jacket being part of the cold finger. The outer jacket is to maintain the temperature within the cryostat. The device was mounted onto a copper block attached to the cold finger, with the device facing downwards.

(a) d.c. Current-voltage measurement

The voltage was applied from a battery, its value being adjusted by a 500 Ω variable resistor. The voltage across the device was measured indirectly by determining the voltage dropped across a fixed resitor in series with the device (fig. 5.4a).

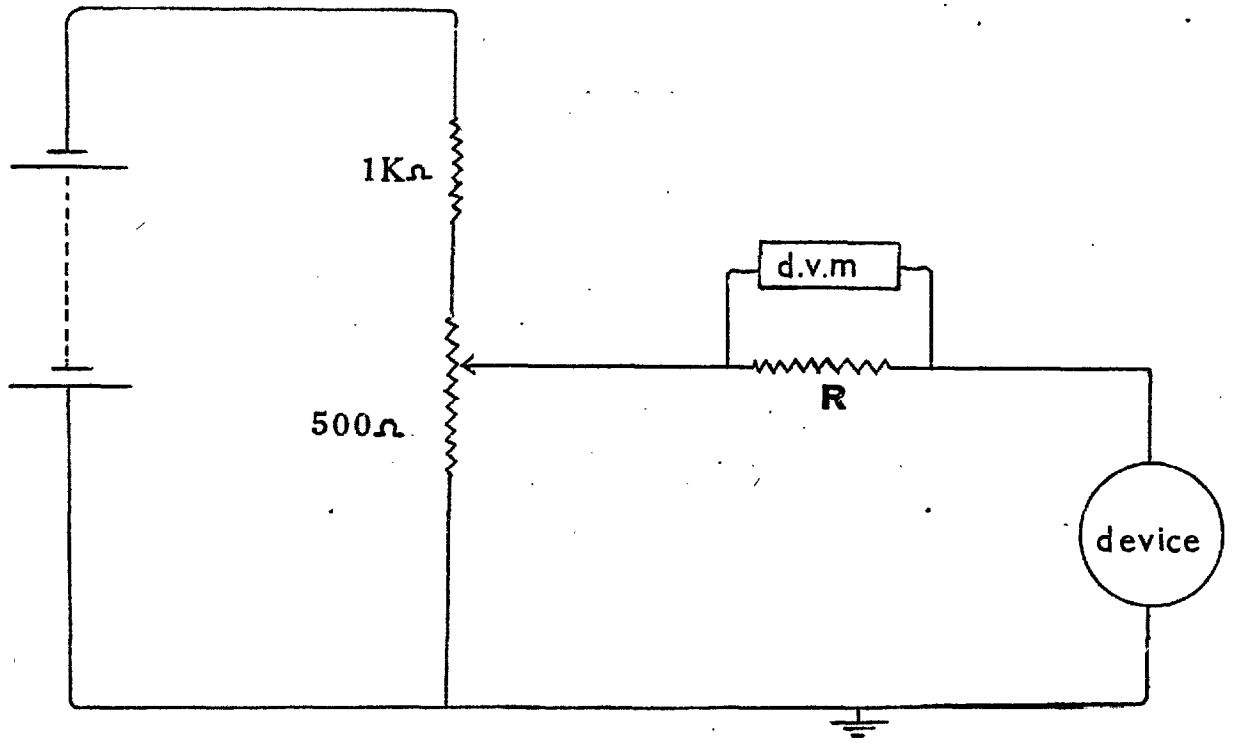

(a)

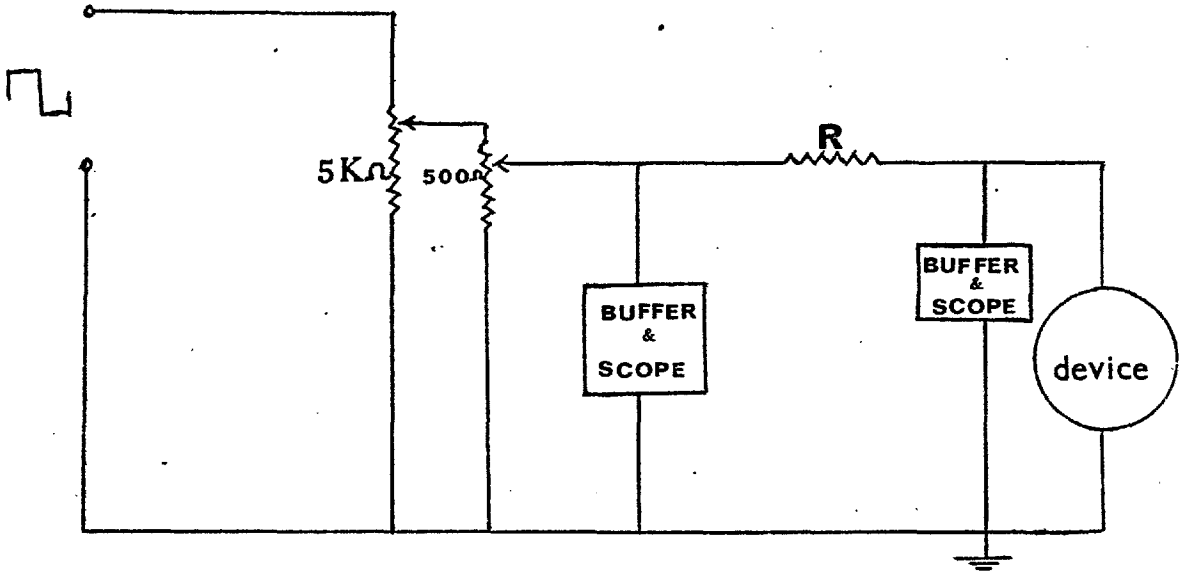

(b)

Fig. 5.4: Current-Voltage Measurement Circuit Diagrams

(a) D.C.

(b) A.C.

(b) a.c. current-voltage measurement

The circuit is schematically shown in fig. 5.4b. The a.c. source used was an Advance Electronics (wide range oscillator) SG67, and the oscilloscope was a Hewlett Packard 1402A. All inputs to the oscilloscope were connected via a buffer box to provide a high input impedance. This is because the impedance of the device was often greater than the input impedance of the scope ($\sim$1 MΩ).

5.2.2 Capacitance Measurement

The variation of capacitance with frequency as a function of temperature was measured. A Wayne-Kerr Radio Frequency Bridge (range 15 KHz to 5 MHz) was used, coupled with a Wayne-Kerr Frequency Source (range 100 KHz-10 MHz). The device was placed in the cryostat as described in section 5.2.1. A constant voltage of 0.74 volt, supplied by the frequency source, was applied across the device.

5.2.3 Photovoltaic Measurement

A prism was mounted at the base of the cryostat (fig. 5.5a) so that light transmitted through the window of the cryostat was reflected up onto the device by the prism. The light source was a quartz halogen bulb (150 w, 240 v), and the light was chopped using a Brookdeal Light Chopper 9479 which allows the chopping frequency to be adjusted. The chopped light was passed through a monochrometor (Type Hilger and Watts) to select the required wavelength. A reference signal was fed from the chopper into

the lock-in amplifier (Brookdeal (type 401) along with the signal from the device. The output from the lock-in amplifier was then fed into a chart recorder (Rikadenti B-281H) (fig. 5.5b). The chart recorder was calibrated with respect to the scanning speed of the monochrometer.

5.2.4 Thermally Stimulated Current Measurement

An absorption pump using a molecular sieve was used to pump the cryostat (fig. 5.6a) to a pressure of 5×10^{-3} torr. This type of pump was selected in order to avoid any gaseous contamination arising from back streaming from an oil filled vacuum pump. The layout of the cryostat is shown schematically in fig. 5.6b. The device was stuck onto a copper block with silver paste, and the leads were joined onto the device using fine gold wires. A heater was embedded in the copper block. When the cold finger was immersed in liquid nitrogen, the sample temperature was $77^{o}K$. The sample was heated by a Stanton Redcroft Programmable Temperature Controller which allowed the heating range to be varied between $1^{o}/min$ and $20^{o}/min$, and temperature gradient across the copper block was negligible for heating rates up to 10^{o} per min. The current through the junction was measured with a Keithley 602B electrometer whose output was registered on the Rekadenki B-281H chart recorder. Background leakage current, measured across the leads out, in open circuit condition with 9 volt bias across the device was $\sim 10^{-13}$ amp (i.e. negligible). Measurements were conducted in the dark.

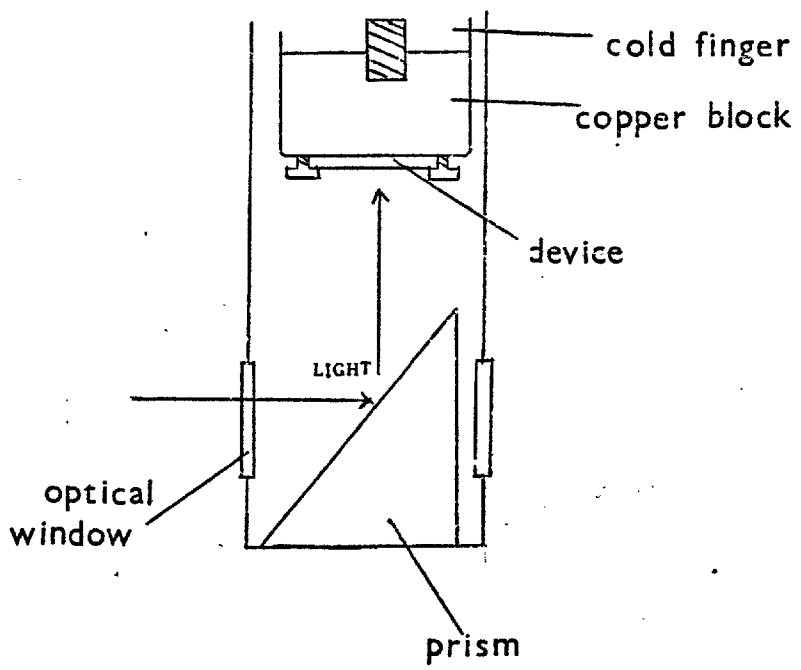

a

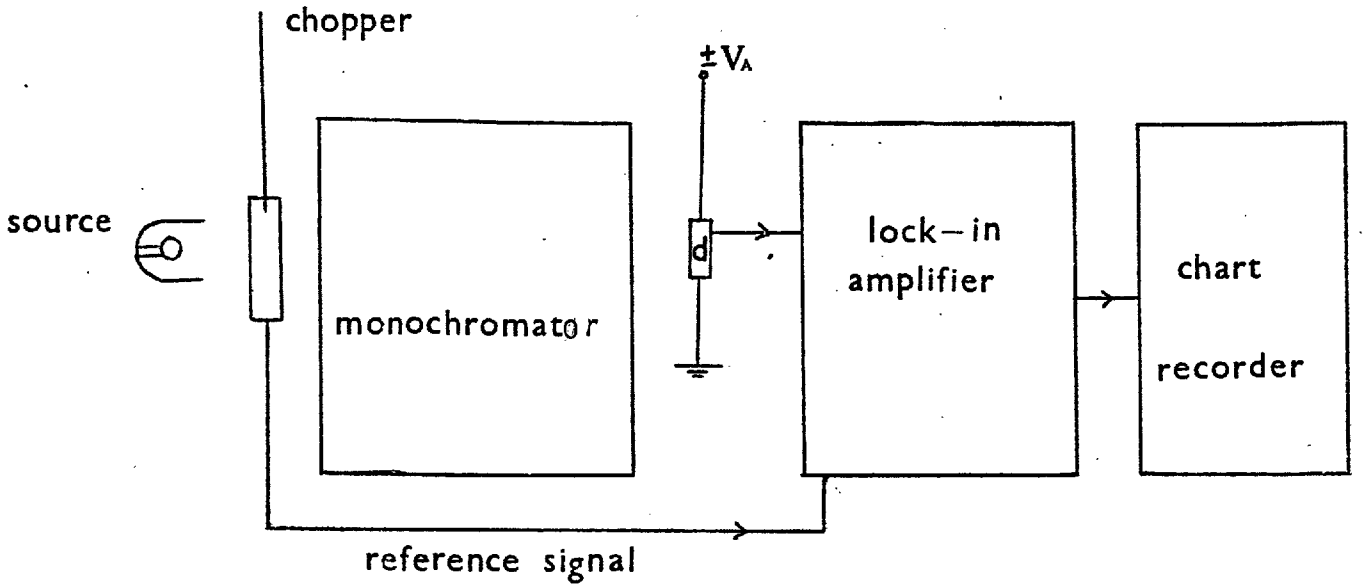

b

Fig. 5.5: Schematic Diagram of Photovoltaic Measurement
(a) Part of the Cryostat
(b) General lay-out of the Experiment
d - device
V_A - applied voltage

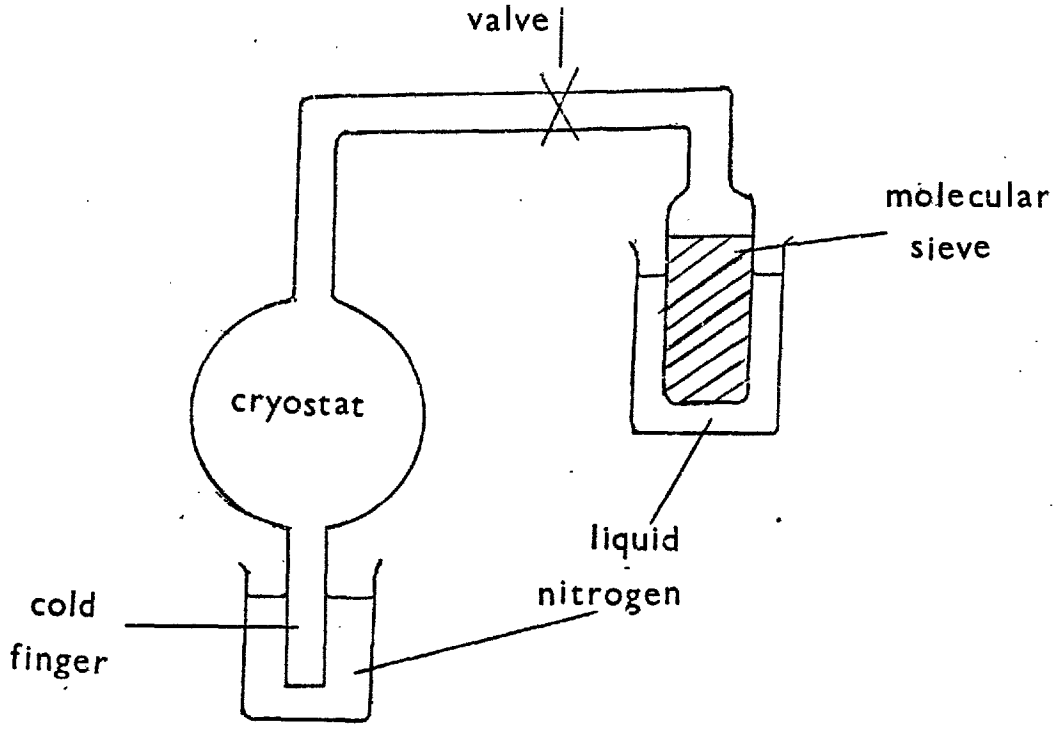

a

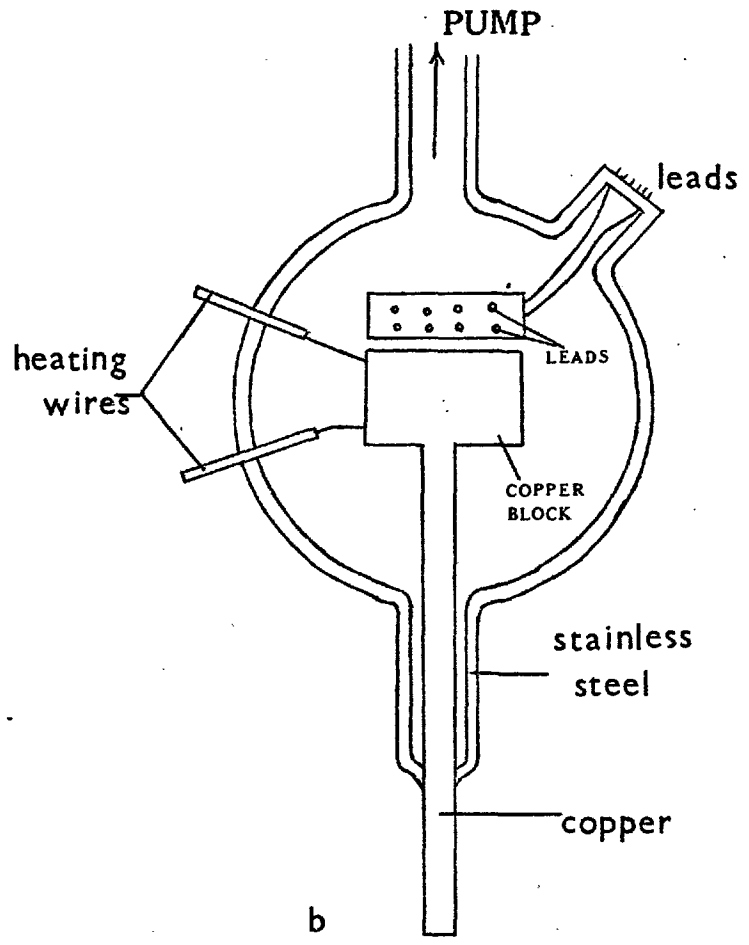

b

Fig. 5.6: Thermally Stimulated Current Measurement
(a) General lay-out
(b) Schematic diagram of the cryostat

CHAPTER 6

RESULTS AND DISCUSSION

6.1 ELECTRICAL RESULTS

6.1.1 D.C. Current-Voltage Results

The D.C. current-voltage characteristic of the heterojunction was investigated in order to obtain information on the D.C. conduction mechanism of the heterojunction.

The current-voltage relationship is of the form

$$I = I_o \exp(V/V_o) \qquad (6.1)$$

for both forward and reverse bias.

The results are shown in figs. 6.1 and 6.2. I_o can be obtained by extrapolating the top half of the curve where eqn. (6.1) holds, the ordinate being V_o, and at $V = V_o$;

$$I = 2.718\ I_o$$

The symmetrical response of the device for both forward and reverse bias is shown in figs. 6.1 and 6.2. The device broke down for both; the breakdown voltage being in the range of 1-2 volts, though in some devices breakdown voltage as low as 0.7 volts were observed. The breakdown was not destructive and did not seem to change the I-V characteristic in any significant way. Hence, it is probably an electronic breakdown of an avalanche type and does not involve any change in the physical structure of the heterojunction films. Breakdown was more easily observed

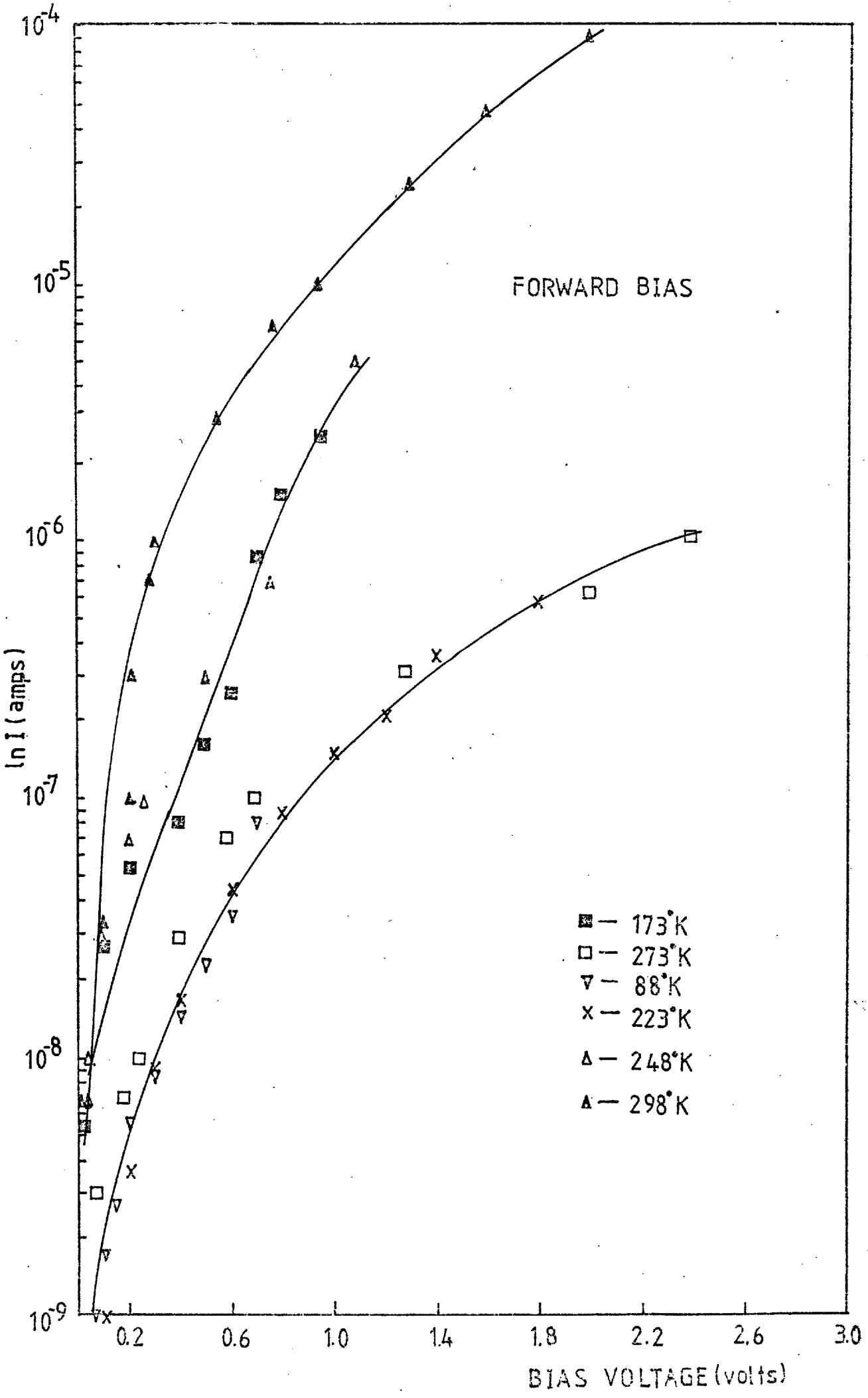

Fig. 6.1a D.C. Current – Voltage Characteristic

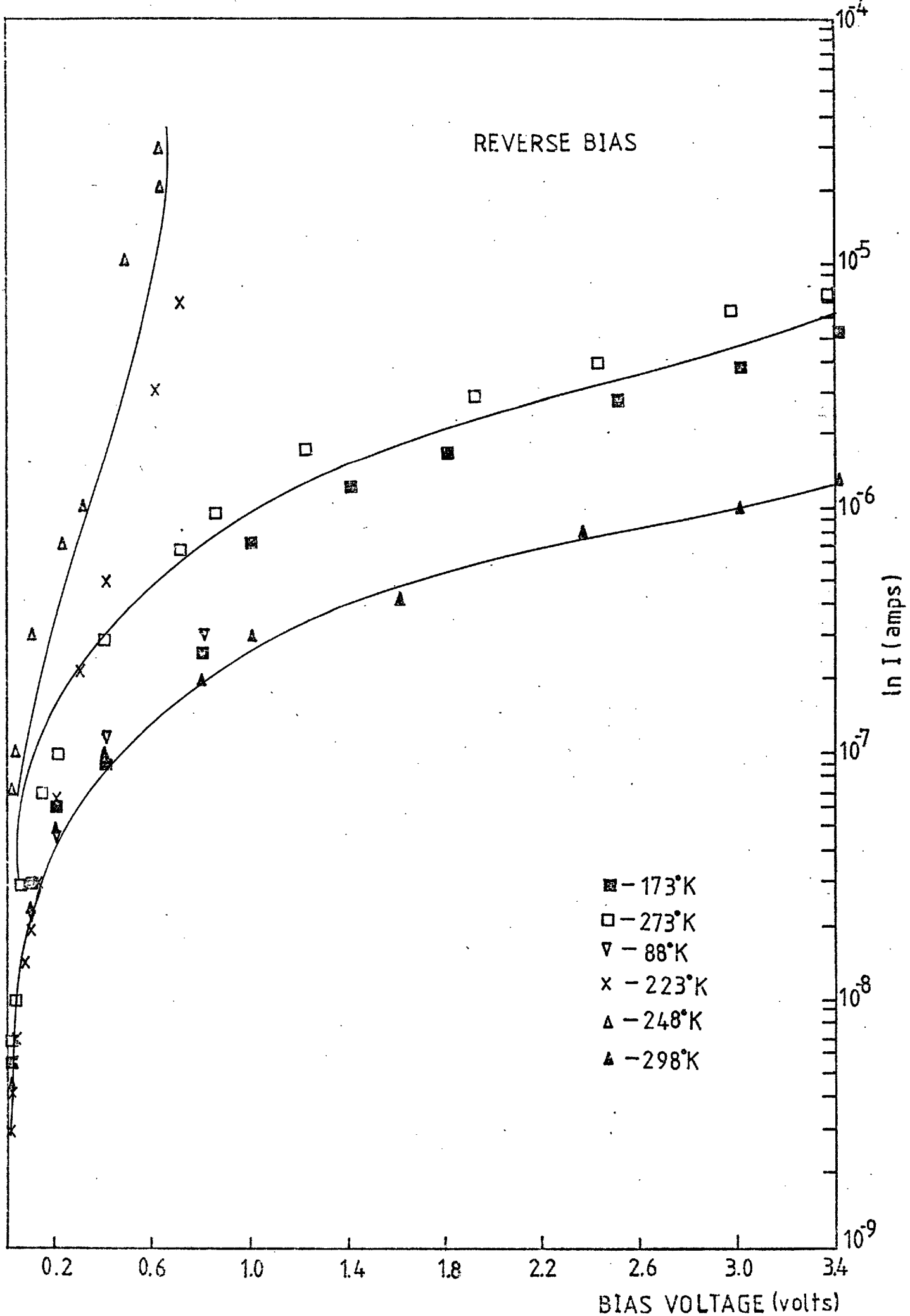

Fig.6.1b D.C. Current—Voltage Characteristic

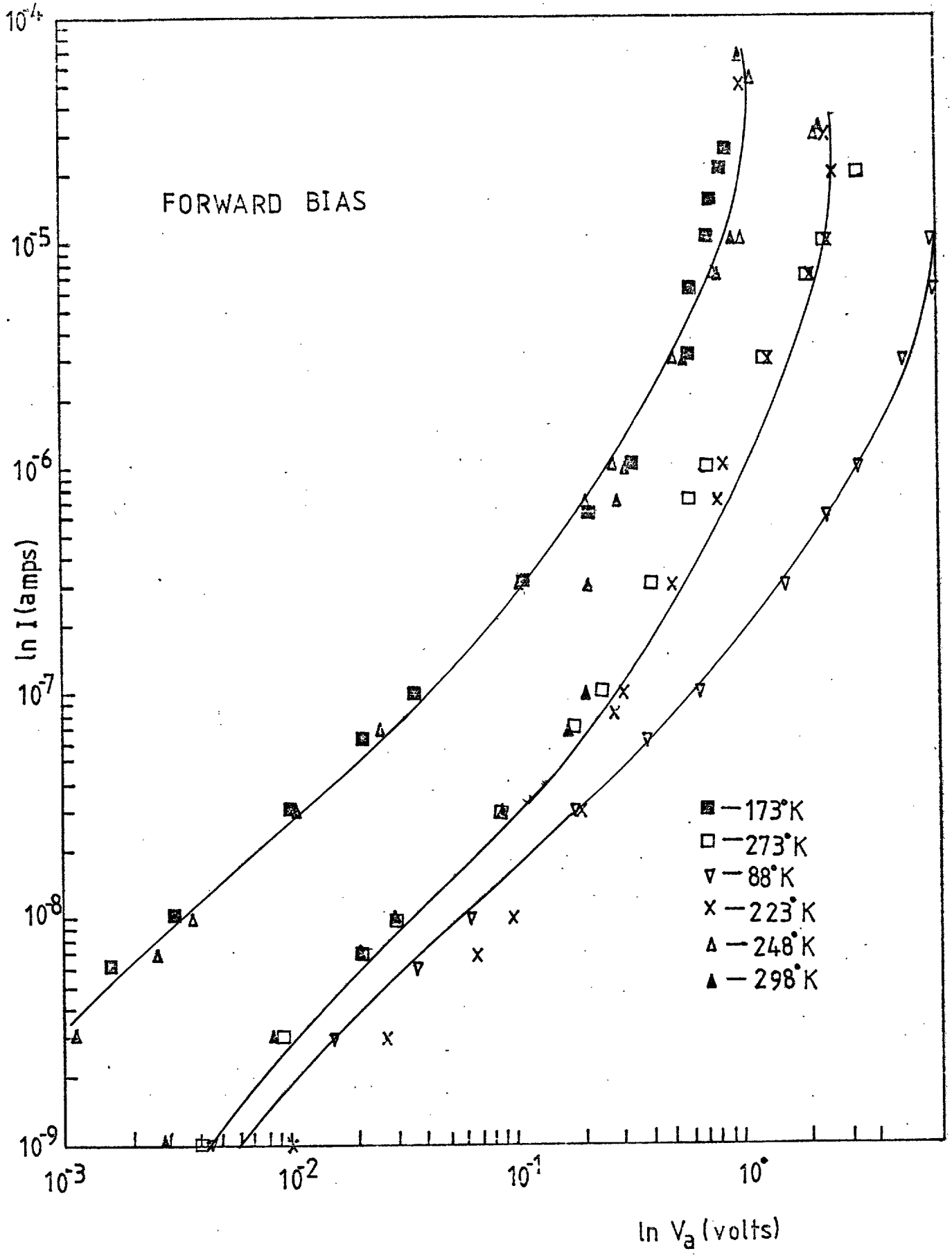

Fig. 6.2a D.C. Current—Voltage Characteristic

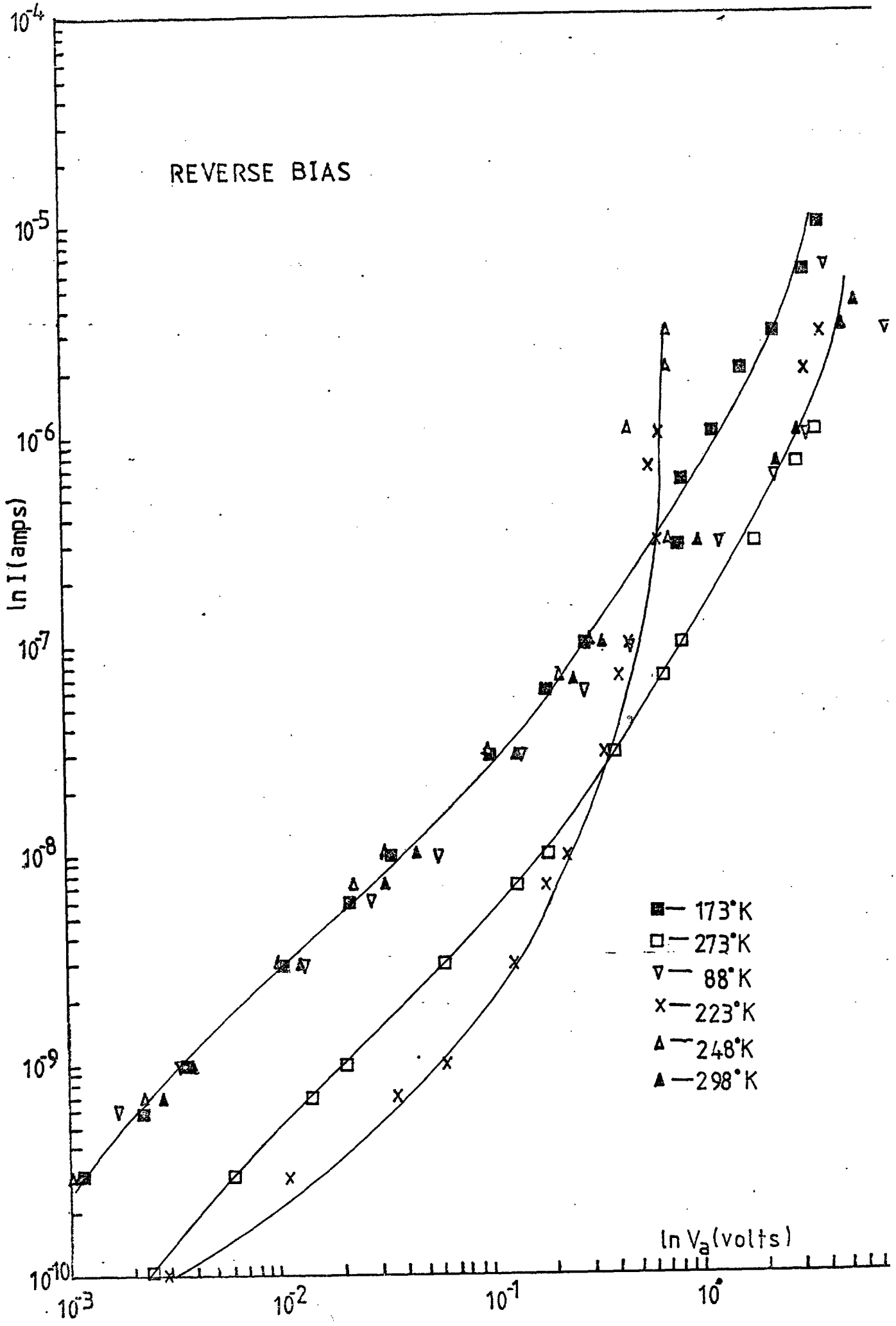

Fig.6.2b D.C. Current-Voltage Characteristic

Bias Condition	V_o(eV)	I_o(amp)	T^o(K)	B(amp-cm)	W (m)
F	0.9	2×10^{-7}	298	6.75×10^{-22}	1.80×10^{-9}
F	0.45	1.3×10^{-5}	298	4.89×10^{-19}	3.61×10^{-9}
R	0.74	9.0×10^{-8}	298	5.12×10^{-22}	2.19×10^{-9}
R	1.72	1.8×10^{-6}	298	1.93×10^{-21}	9.44×10^{-10}
F	1.5	4.6×10^{-6}	273	5.92×10^{-21}	1.08×10^{-9}
F	1.16	1.1×10^{-6}	273	2.16×10^{-21}	1.40×10^{-9}
R	1.61	3.3×10^{-6}	273	3.85×10^{-21}	1.01×10^{-9}
R	1.38	7.5×10^{-7}	273	$1.09(5)\times10^{-21}$	1.18×10^{-9}
F	0.3	3.1×10^{-7}	248	1.3×10^{-19}	5.41×10^{-9}
R	0.26	1.8×10^{-7}	248	2.30×10^{-19}	6.25×10^{-9}
F	0.22	2.85×10^{-7}	248	1.66×10^{-18}	7.38×10^{-9}
R	0.07	8.7×10^{-8}	248	7.66×10^{-10}	2.32×10^{-9}
F	1.32	1.7×10^{-6}	223	2.67×10^{-21}	1.23×10^{-9}
R	0.115	1.9×10^{-7}	223	9.02×10^{-15}	1.41×10^{-8}
F	1.16	1.9×10^{-7}	223	3.24×10^{-22}	1.4×10^{-9}
R	0.097	1.4×10^{-8}	223	2.56×10^{-14}	1.68×10^{-8}
F	0.18	1.4×10^{-7}	173	7.30×10^{-18}	9.02×10^{-9}
R	1.4	4.4×10^{-6}	173	6.28×10^{-21}	1.16×10^{-9}
F	0.21	2.1×10^{-8}	88	1.96×10^{17}	7.73×10^{-9}

Table 6.1: $B = {}^{J_o}/_{N_t}) \exp({}^{V_d}/_{V_o})$, $J_o = I_o/a$, $N_t = 10^{18}$ cm^{-3},
$q = 3.3 \times 10^{-3}$ cm^2, $V_d = 2.17$ eV $K = 0.5$,
$W = 2\ (\alpha K e^{3/2}\ V_o)$
I_o from figs. 6.1; F - Forward; R - reverse

at temperatures less than 248^{o}K and negative resistance was observed in a few cases (fig. 6.3). For some devices quasi-breakdown was observed when another electrical path was adopted (fig. 6.4). These electrical paths could also be described by eqn. (6.1). However, there was a change in I_o and V_o.

The current was observed to vary randomly with temperature. No relation of any form can be obtained.

D.C. current-voltage measurements have shown that the current obeyed an empirical formula of the form of eqn. (6.1). This was observed by other workers, e.g. Denton et al. (1975) and Walsh et al. (1970). Eqn. (6.1) also resembled the results obtained by Newman (1965) and derived by Tansley (1966) (cf. eqn. 2.55), except the D.C. I-V results obtained showed no temperature dependence. The value of I_o is relatively stable (table 6.1), remaining within an order of magnitude and the D.C. resistance was obtained from the linear region (V_a < 1.0 volt) of the D.C. I-V response. The resistance of forward bias characteristic was higher (maximum 6.2 MΩ and minimum 380 kΩ) than that of reverse bias (maximum 1.9 MΩ and minimum 340 kΩ). This result implies that though the conduction mechanism of reverse bias and forward bias are the same, the electrical path must be different or conduction is associated with different carriers. Since eqn. (6.1) was temperature independent, conduction could be due to tunnelling.

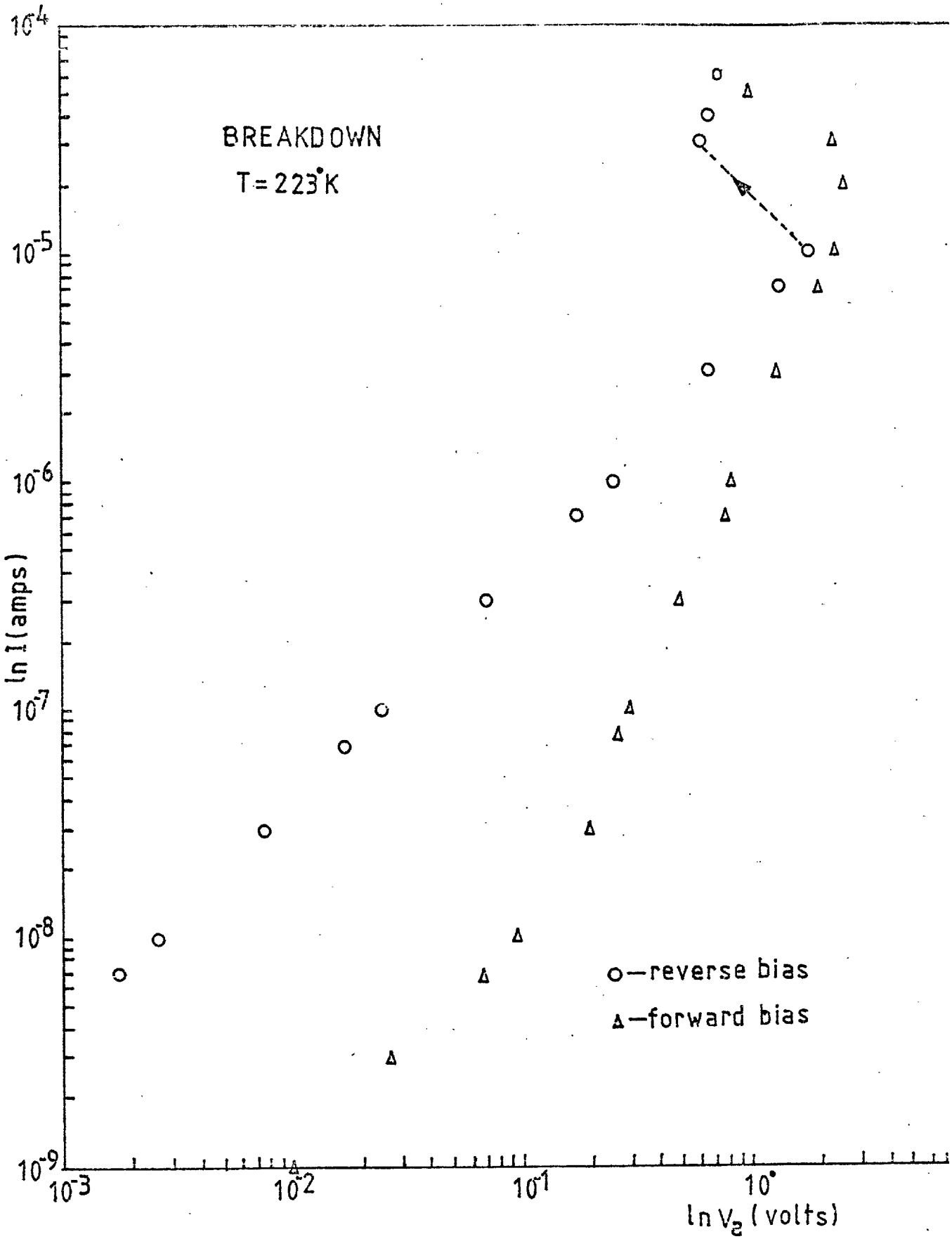

Fig. 6.3 D.C. Current– Valtage Characteristic

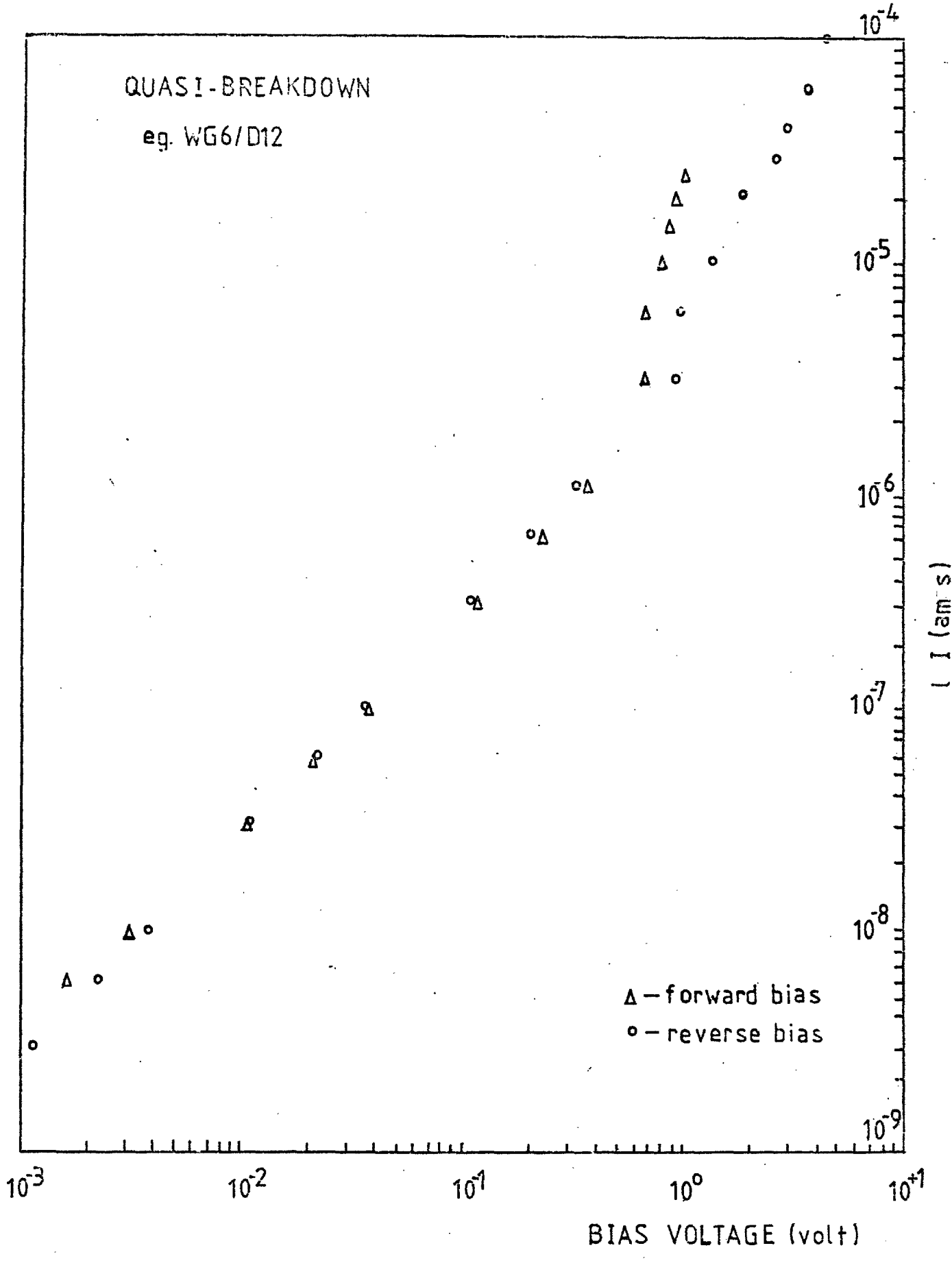

Fig.6.4 D.C. Current– Voltage Characteristic

6.1.2 A.C. Current-Voltage Results

To investigate the A.C. and capacitance properties of the heterojunction, A.C. current-voltage measurements were taken.

The results showed that the current increased with frequency and voltage (fig. 6.5a). The relation between current and voltage was linear except at frequencies less than 10 kHz and higher than 1 MHz, where non-linearity was observed in some cases. Fig. 6.5a shows some typical A.C. current-voltage results. The increase in current with frequency can be attributed to the A.C. impedance decreasing with increasing frequency. It was found that the current-frequency relationship could be expressed empirically by (fig. 6.5b)

$$I \propto \exp(-\gamma\omega^{-1/n}) \qquad (6.2)$$

where γ was a constant and n was found to be 5 in some cases and 9 in others through curve fitting. The gradients (table 6.2) were relatively stable for a given temperature. Unfortunately the data was too limited to establish with any certainty the γ-T relation, although it is possibly a linear relation (fig. 6.5c):

$$\gamma \propto 0.4T \qquad (6.3)$$

As eqn. (6.3) implies, T could be linearly related to γ. Fig. 6.6 also shows that there is a weak relationship between current and temperature. However, the current

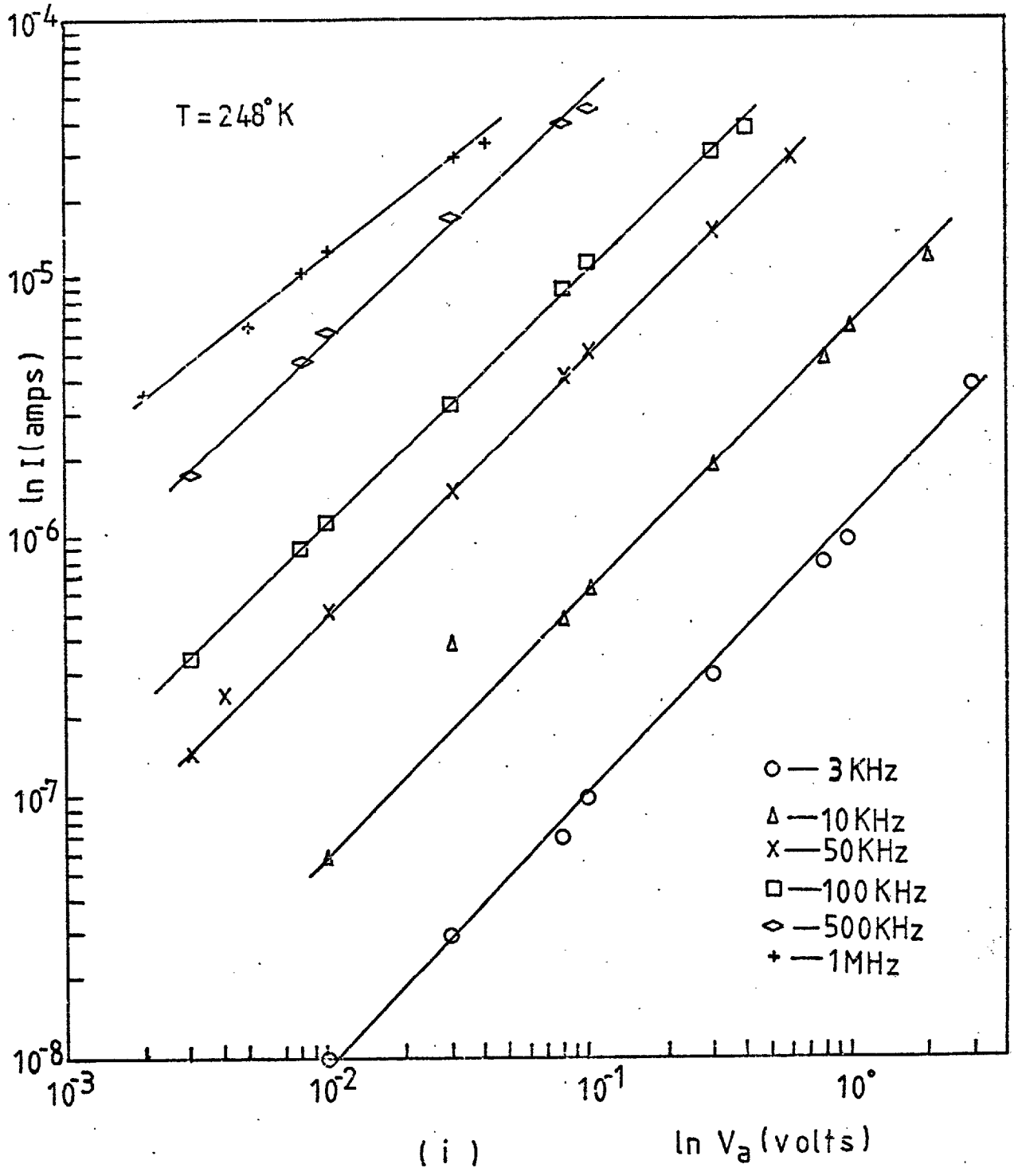

Fig.6.5a Typical A.C. Current–Voltage Result

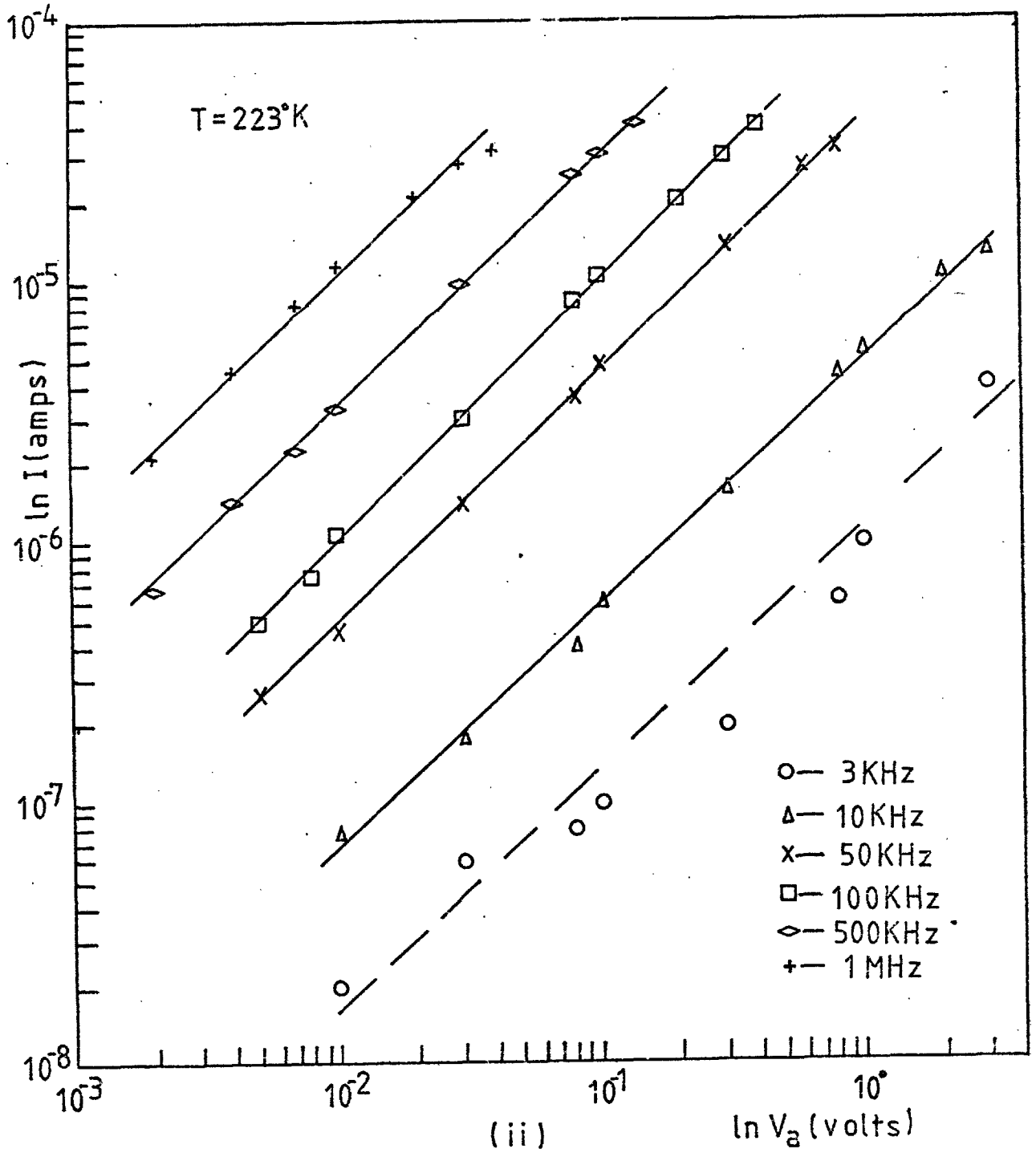

Fig.6.5a Typical A.C. Current–Voltage Result

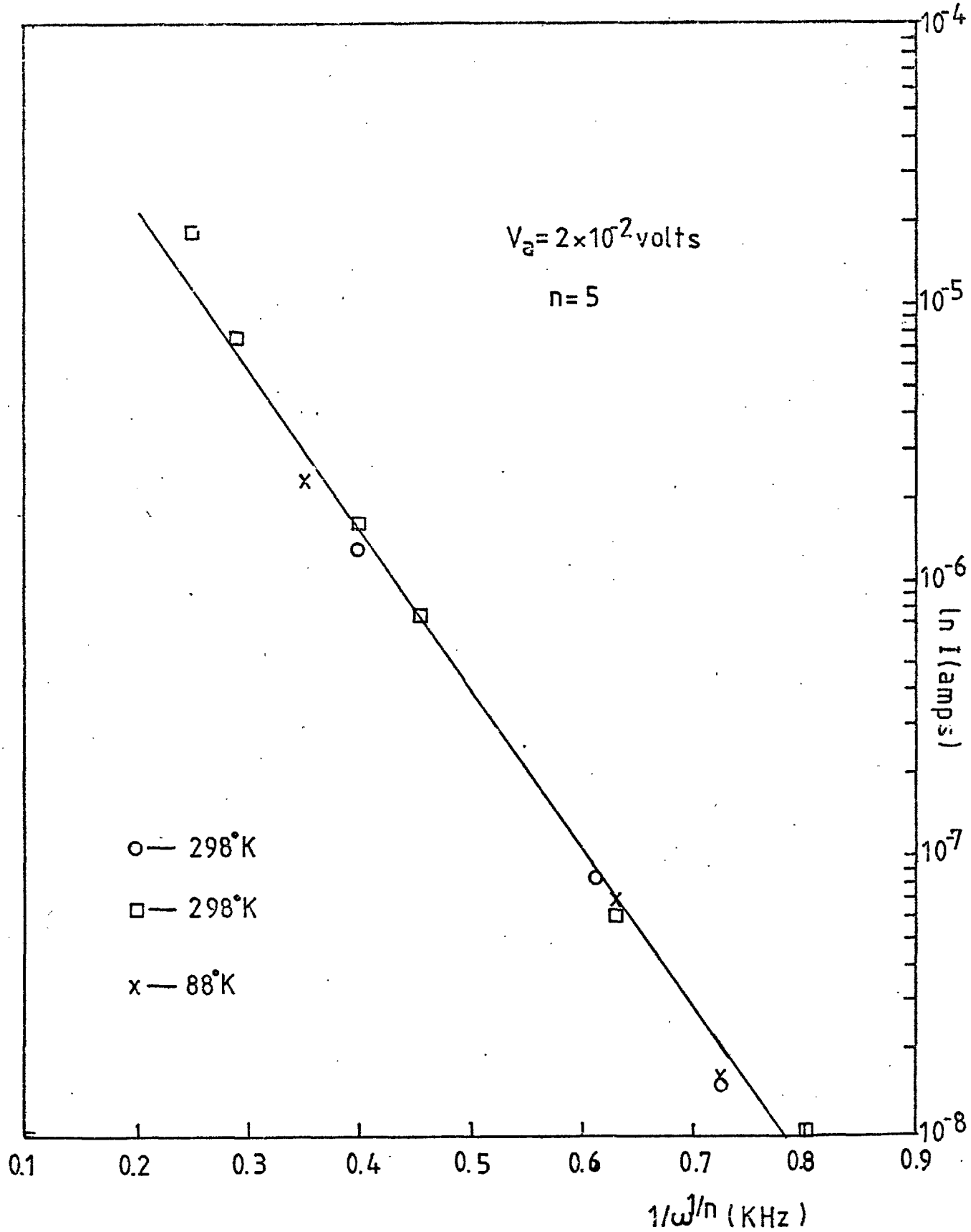

Fig. 6.5b A.C. CURRENT— FREQUENCY RELATION

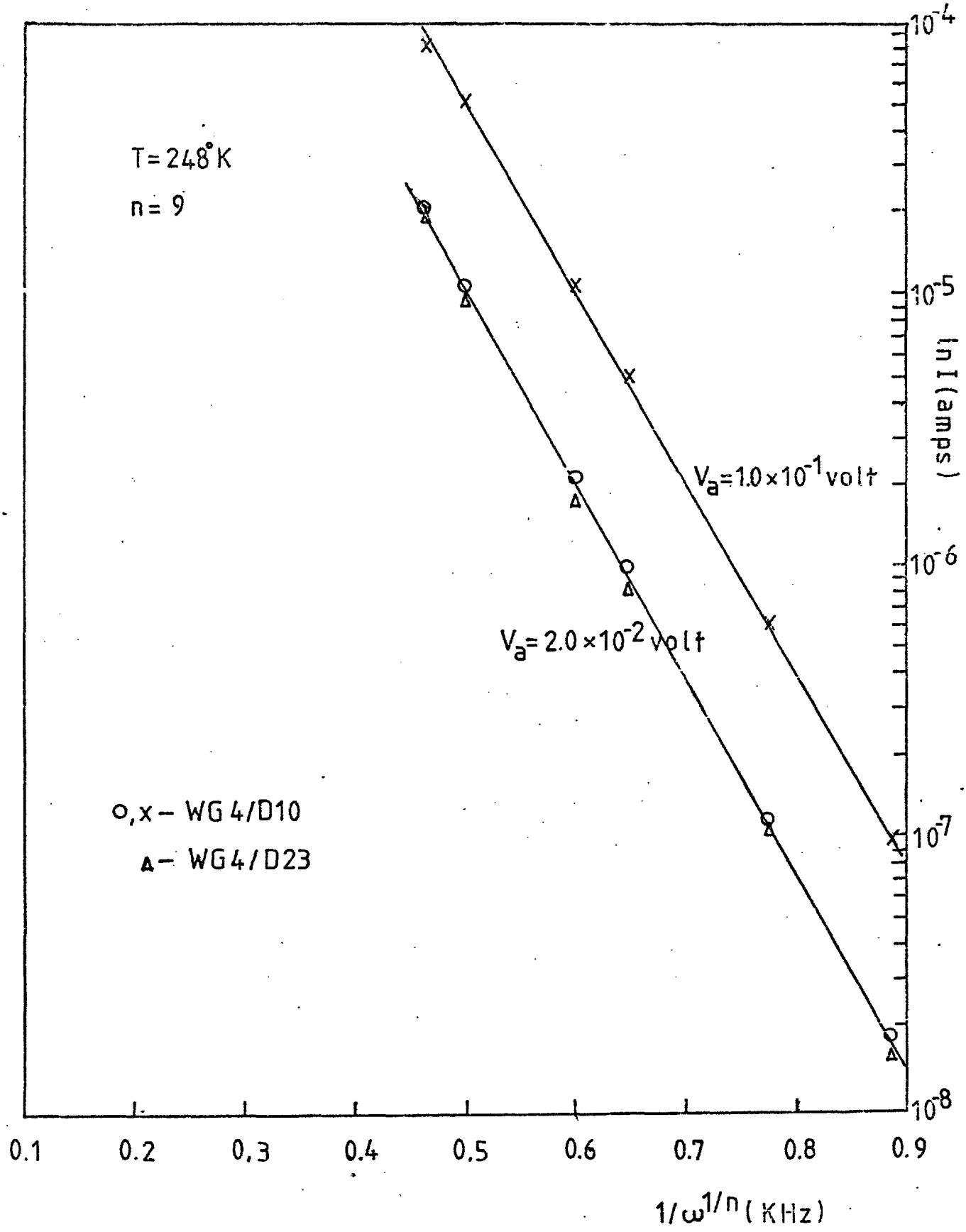

Fig.6.5b A.C CURRENT—FREQUENCY RELATION

T(^{o}K)	n	α
248	9	16.53
248	9	16.53
100	8	16.53
273	9	15.64
273	9	14.19
223	10	17.17
223	9	17.17
298	6	14.17
298	5	14.17
88	5	14.17
298	5	10.79

Table 6.2: (cf. equation 6.2)

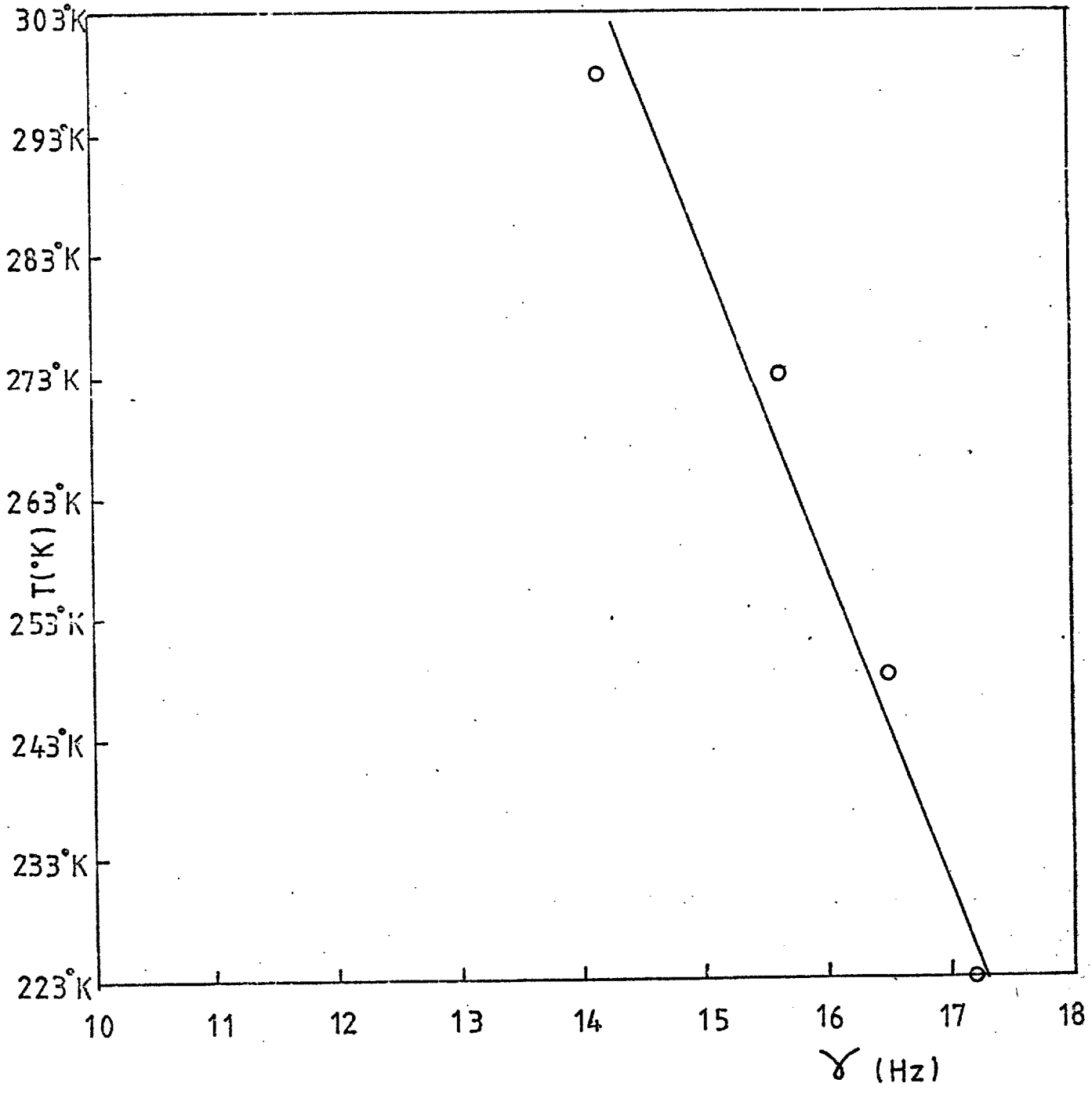

Fig.6.5c Temperature— γ Relation

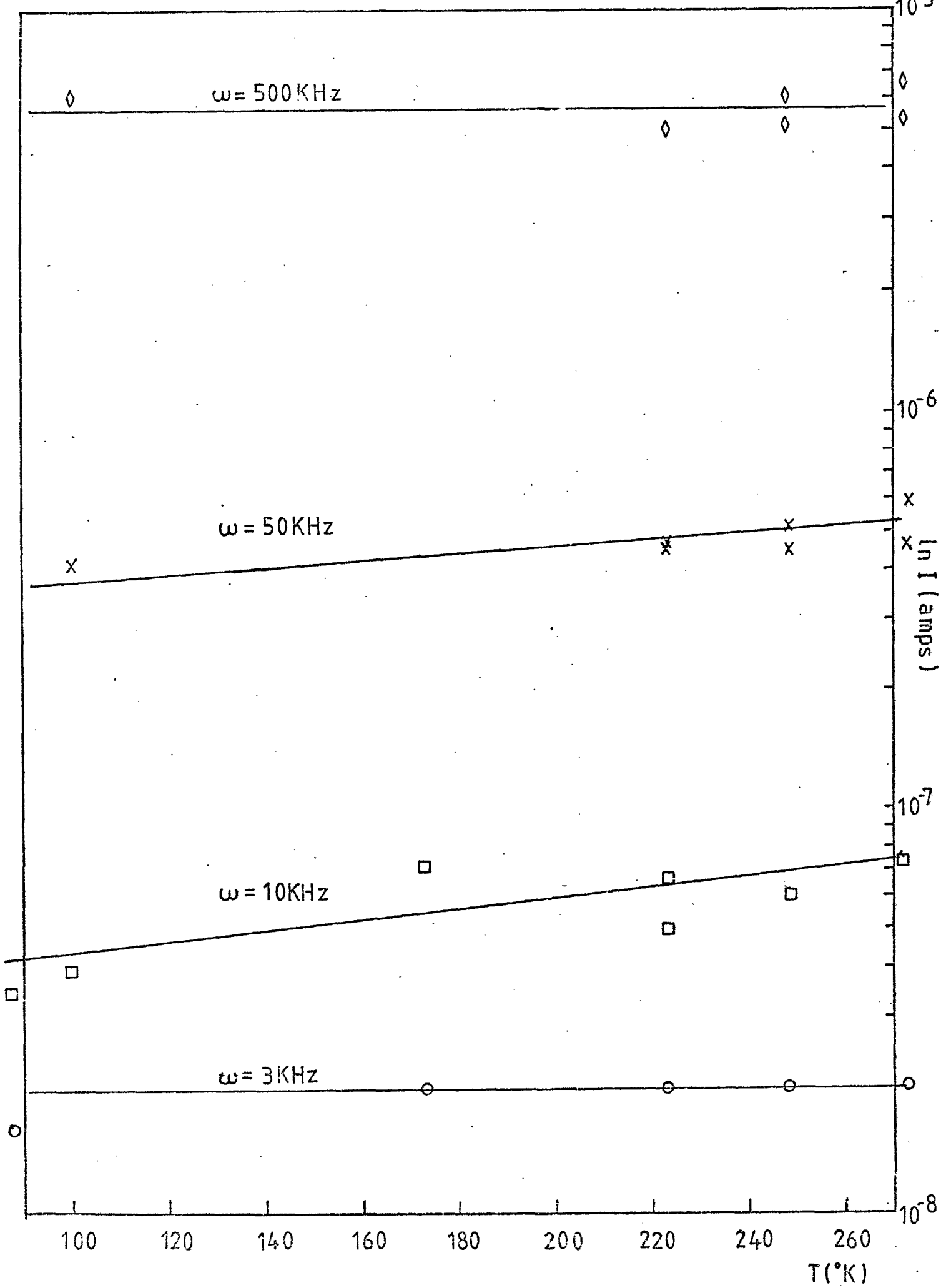

Fig.6.6 A.C. Current — Temperature Relation

became independent of temperature as bias voltage and frequency increased. Thus, current-temperature relationship might not be as simple as eqn. (6.3) indicates.

A.C. impedance, Z_{AC}, was plotted against frequency, ω, in an attempt to find out the Z_{AC}-ω relation (fig. 6.7). It was found that,

$$Z_{AC} \alpha \omega^{-1.3} \tag{6.4}$$

Fig. 6.6 also shows that Z_{AC} was independent of temperature. Eqn. (6.4) implies that Z_{AC} can be approximated to capacitive impedance, i.e. the interface junction impedance was the dominant characteristic. Thus, measurements made depended on the current-voltage characteristic of the junction and not that of the films. The weak dependence of temperature of the A.C. current agreed well with that observed for the D.C. current-voltage result whereas the current-frequency relation shows that the current is conducted along two or more electrical paths although the transport mechanism remained the same in both cases.

6.1.3 Capacitance-Frequency Measurement Results

Capacitance-frequency measurements as a function of temperature were made to supplement the A.C. current-voltage measurement.

The capacitance was independent of temperature and remained constant up to 600 kHz where it began to decrease (fig. 6.8a). In the frequency region 600-1000 kHz

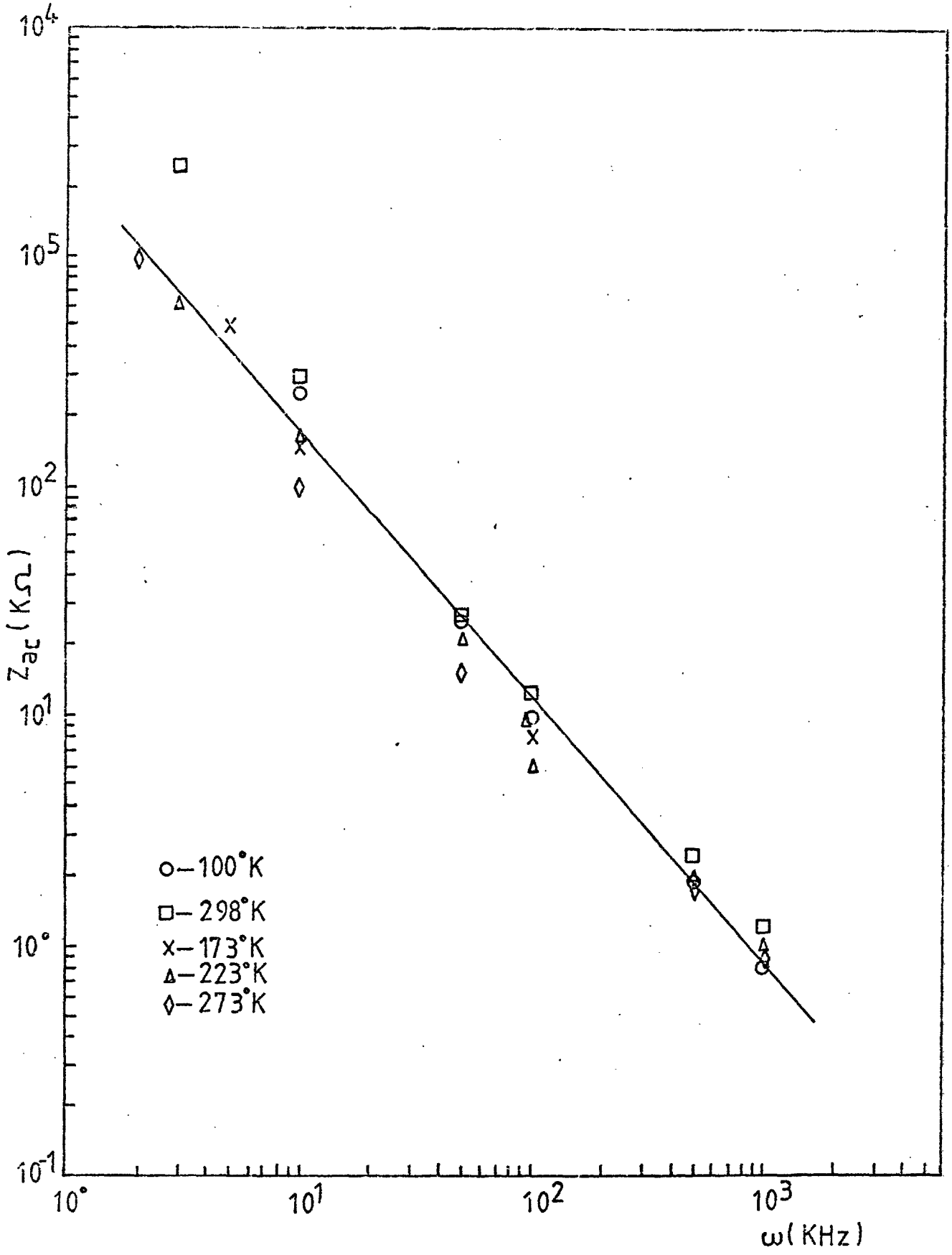

Fig.6.7 A.C. Impedance–Frequency Relation

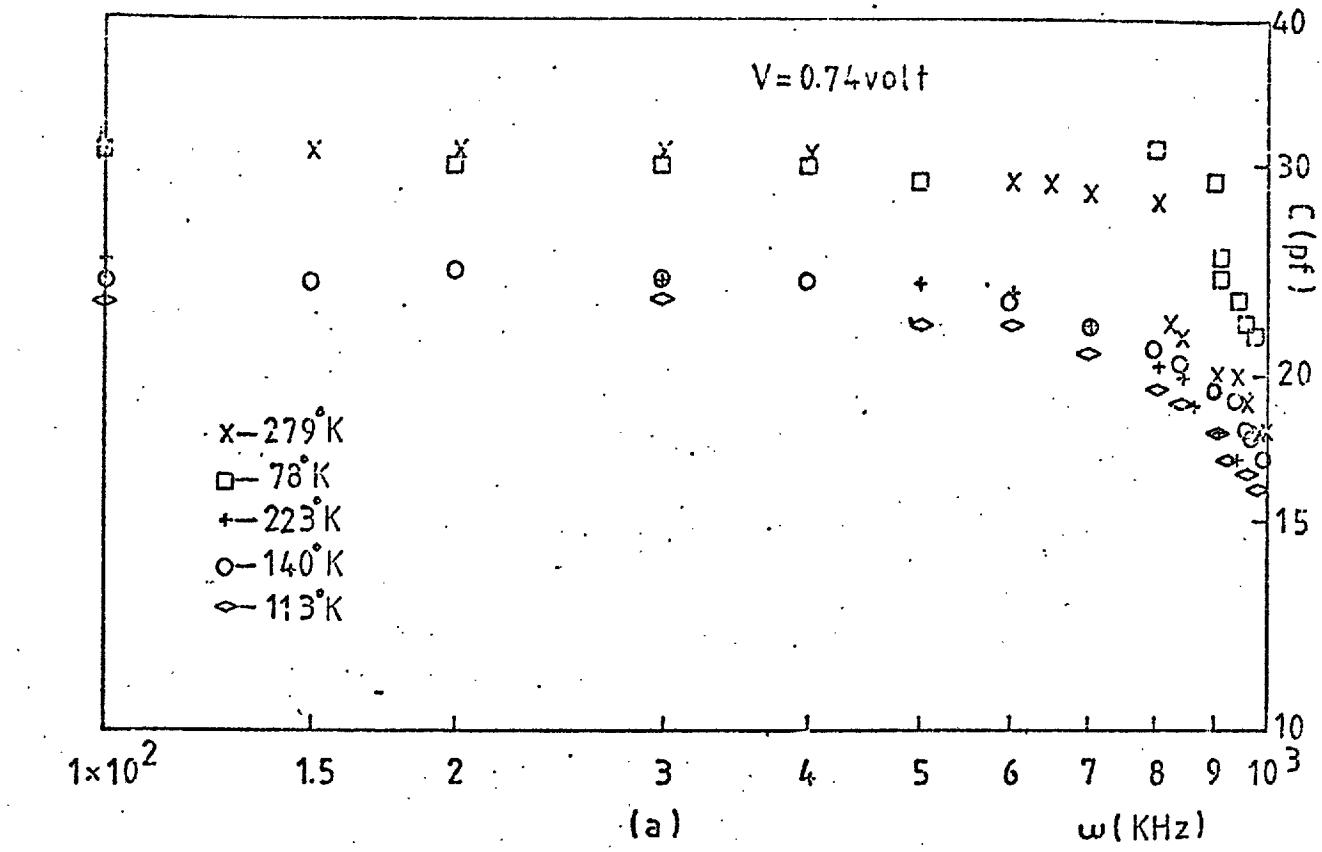

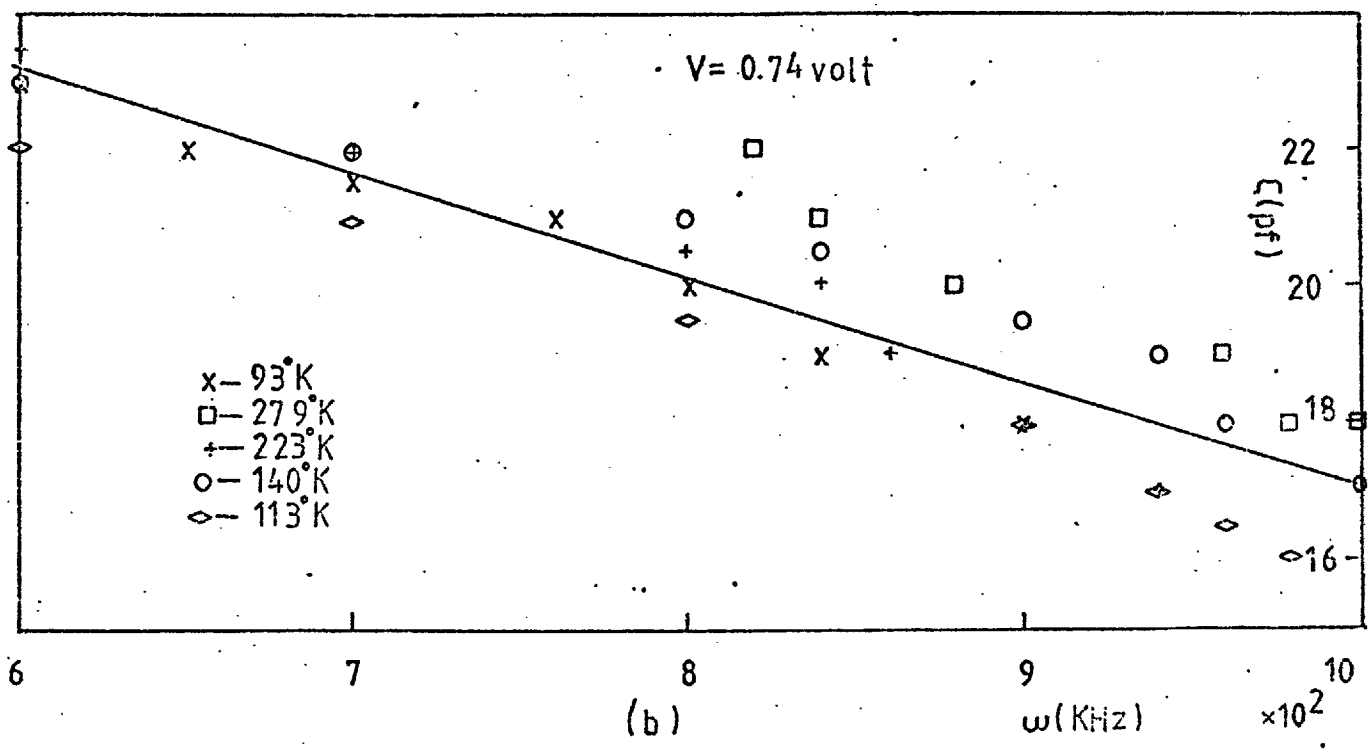

Fig. 6.8(a) Frequency — Capacitance Relation (log–log)

(b) Part of (a) in linear–linear plot

the dependance was with a gradient of the order of 1.5×10^{-2} pF/kHz (fig. 6.8b). At higher frequency measurements ($\omega \geq$ 600 kHz, say), the capacitance of the coaxial cables used may be significant as the cable capacitance is about 100 pF/m. Hence, a one meter long coaxial cable would have a loading impedance of the order of 17 kΩ for ω = 600 kHz to 10 kΩ for ω = 1 MHz. From fig. 6.7 the A.C. impedance at 1 MHz is found to be about 1 kΩ giving a maximum probable error of about 10%. Since the coaxial cable used was normally no more than half a meter long, this error can be neglected in comparison to the scatter of the data. In view of this result the frequency response is due to the device over this frequency range and is the same as a low pass filter characteristic with a complex impedance (fig. 6.9; cf. section 6.5).

6.2 PHOTOVOLTAIC RESULTS

Photovoltaic measurements were made to investigate the shape of the depletion regions in each side of the function. The effect of the chopping frequency of the light source and temperature on the photoresponse was also investigated.

(i) Chopping frequency and interface space charge

The best response was generally observed at chopping frequencies between 40-80 Hz (fig. 6.10) giving a response time of 25 ms-12.5 ms. Photoresponse under forward bias was found to have the fastest response time, (12.5 ms), compared to the photoresponse for reverse bias

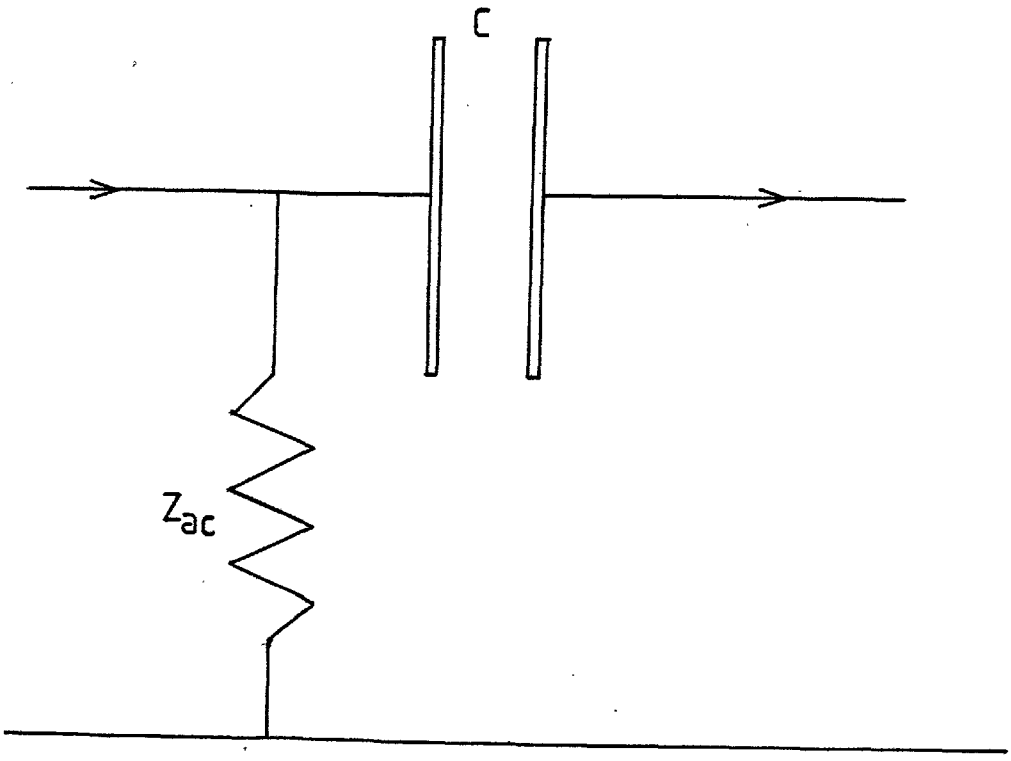

Fig. 6.9: Equivalent Circuit of C-ω Results - a low peak filter

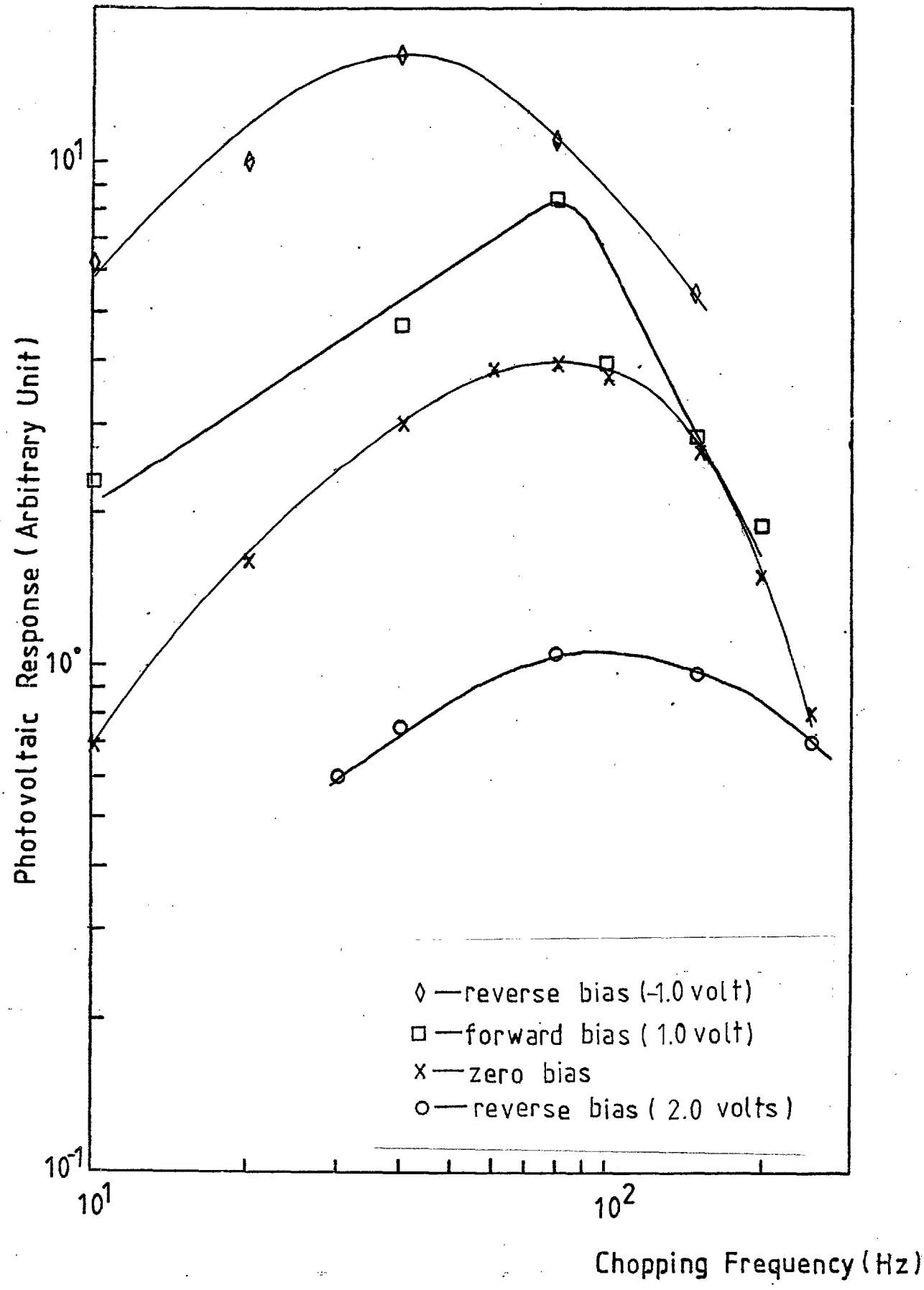

Fig.6.10 Chopping Frequency vs Photoresponse

of about 25 ms. Thus, photogenerated carriers were collected fastest when heterojunctions were forward biased.

The nature of the space charge can be determined from the zero bias photovoltaic response which showed window effect (fig. 6.11) as is expected for a junction which is double depleted (cf. Sadek, 1975, fig. 4.4). The type of band bending (i.e. depletion or accumulation) was investigated using the photovoltaic results obtained for a device in forward and reverse bias and the results agree with those obtained for zero bias. The response peaked at a wavelength of 0.79 μm corresponding to photon energy of 1.6 eV. Since CdSe and CdTe have a band gap of 1.5 eV and 1.7 eV respectively, the photoresponse peak would arise from the interface junction which ideally would have a band gap of about 1.6 eV. Window effect observed has a response shape not as well defined as that produced by single crystal heterojunction (Milne and Feucht, 1972). The response range was 0.7 μm (1.77 eV) - 1.0 μm (1.2 eV). While the cut-off at high energies is to be expected from the size of the band gap of n-CdSe, at the lower energy end of the range a response was observed below the band gap of CdTe with two small peaks occurring at ∿1.27 (±0.01)eV and ∿1.03 (±0.14)eV. These peaks were more pronounced for chopping frequencies between 20-80 Hz, and within the temperature range 288°K - 308°K. It is probable that they may be attributed to the release of trapped carriers or photoexcited carriers trapped by localised states within the band gap of the heterojunction.

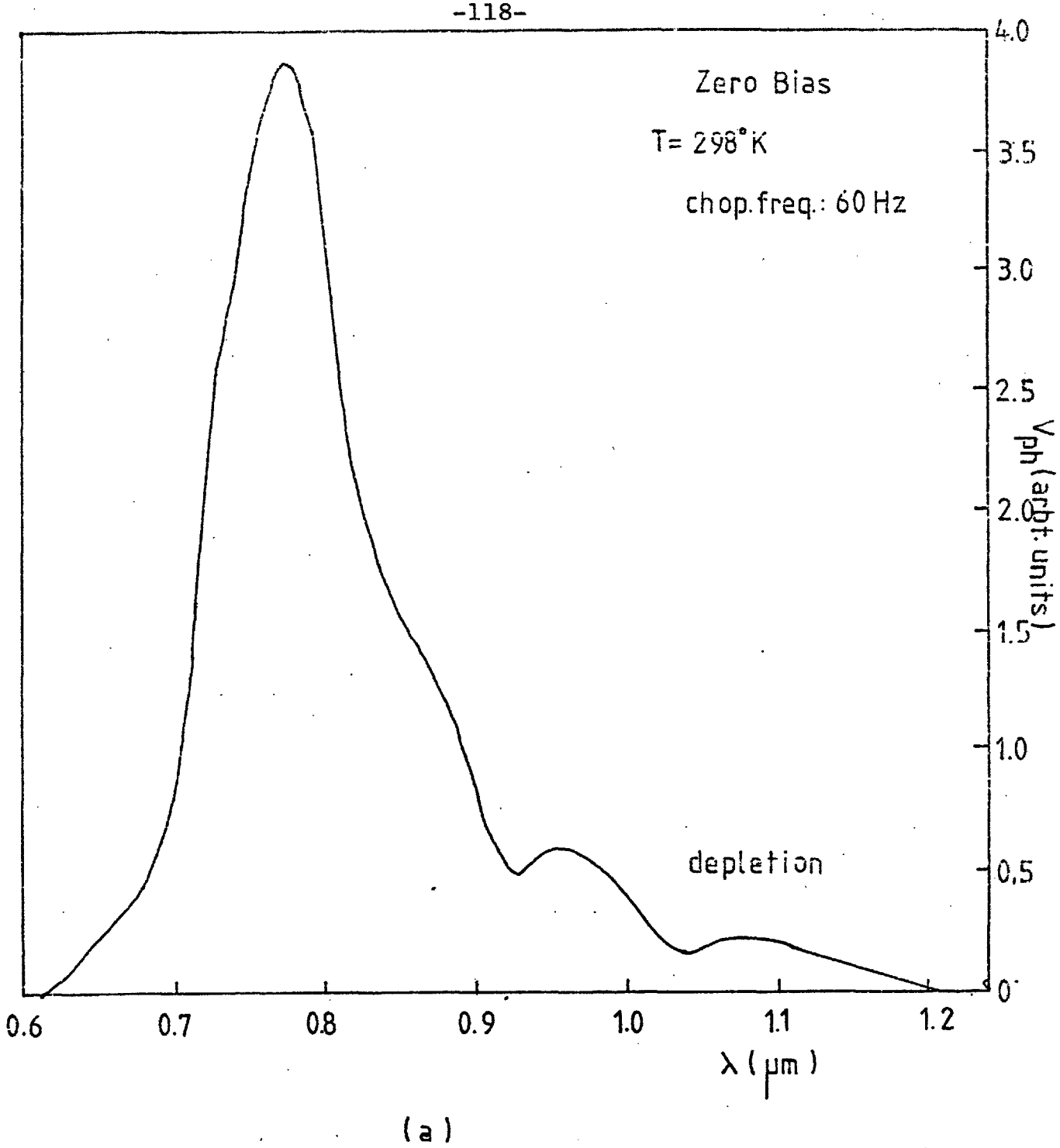

Fig.6.11 Typical Zero Bias Photovoltaic Results

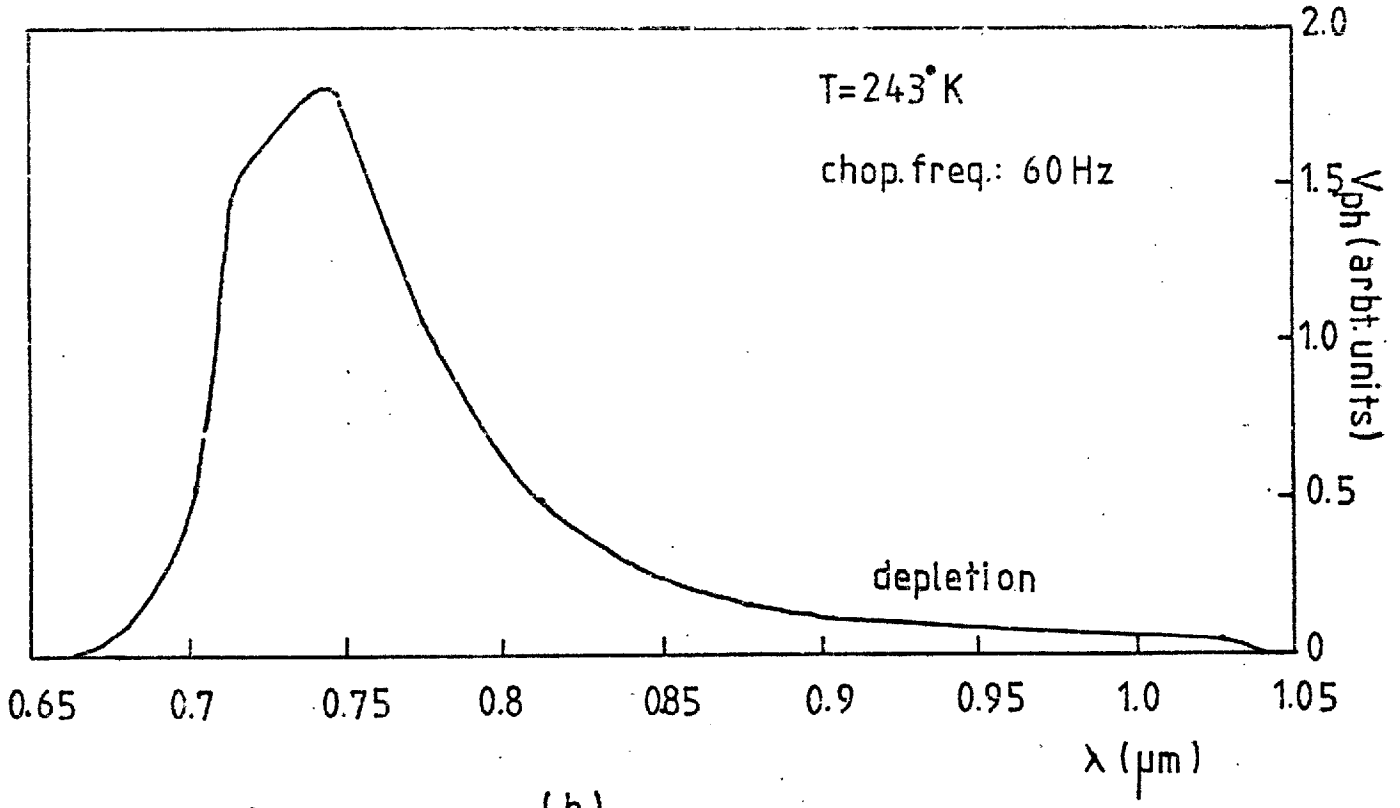

(b)

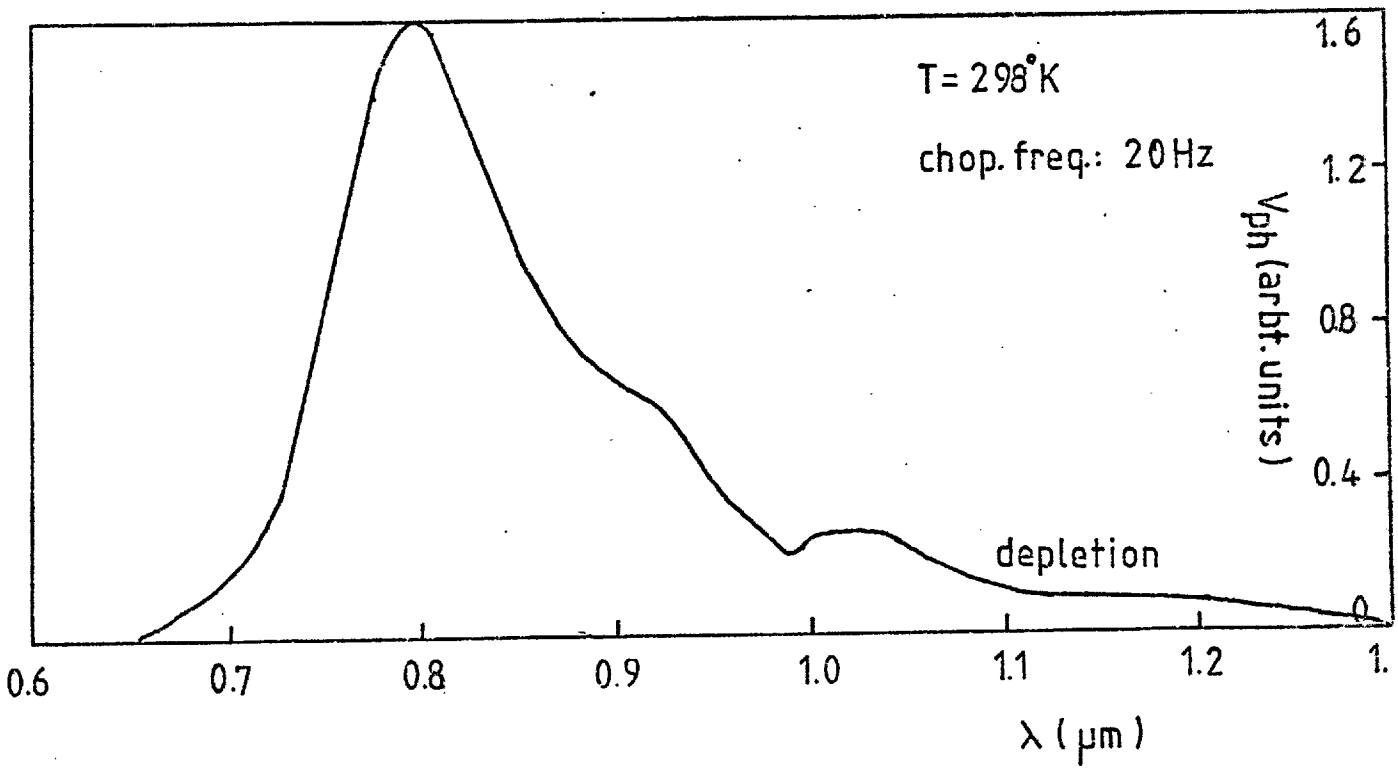

(c)

Fig. 6.11 Typical Zero Bias Photovoltaic Results

(ii) Applied voltage dependence

(a) Forward bias

The results showed that depletion occurred at the interface junction for temperature below $0^{\circ}C$, whereas above this temperature double accumulation was observed (fig. 6.12a). The change from accumulation to depletion began on the CdTe side as it has the smaller band gap. The change was also dependent on the bias voltage but the change with respect to bias voltage was inconsistent and no definite relation could be obtained. An empirical relation is found between the photovoltage, V_{ph}, and the forward bias applied voltage, V_a (fig. 6.12b) i.e.

$$V_{ph} \propto V_a^2 \tag{6.5a}$$

or since the photocurrent, $I_{ph} \propto V_{ph}$

$$I_{ph} \propto V_a^2 \tag{6.5b}$$

The photoresponse range was the same as for zero bias.

(b) Reverse bias

Double depletion at the interface was observed (fig. 6.13a) except at temperature less than $223^{\circ}K$ where accumulation was observed in one measurement. Generally, the reverse bias response was greater in magnitude than either forward bias or zero bias. The results can be represented by an empirical formula (fig. 6.13b) of the form:

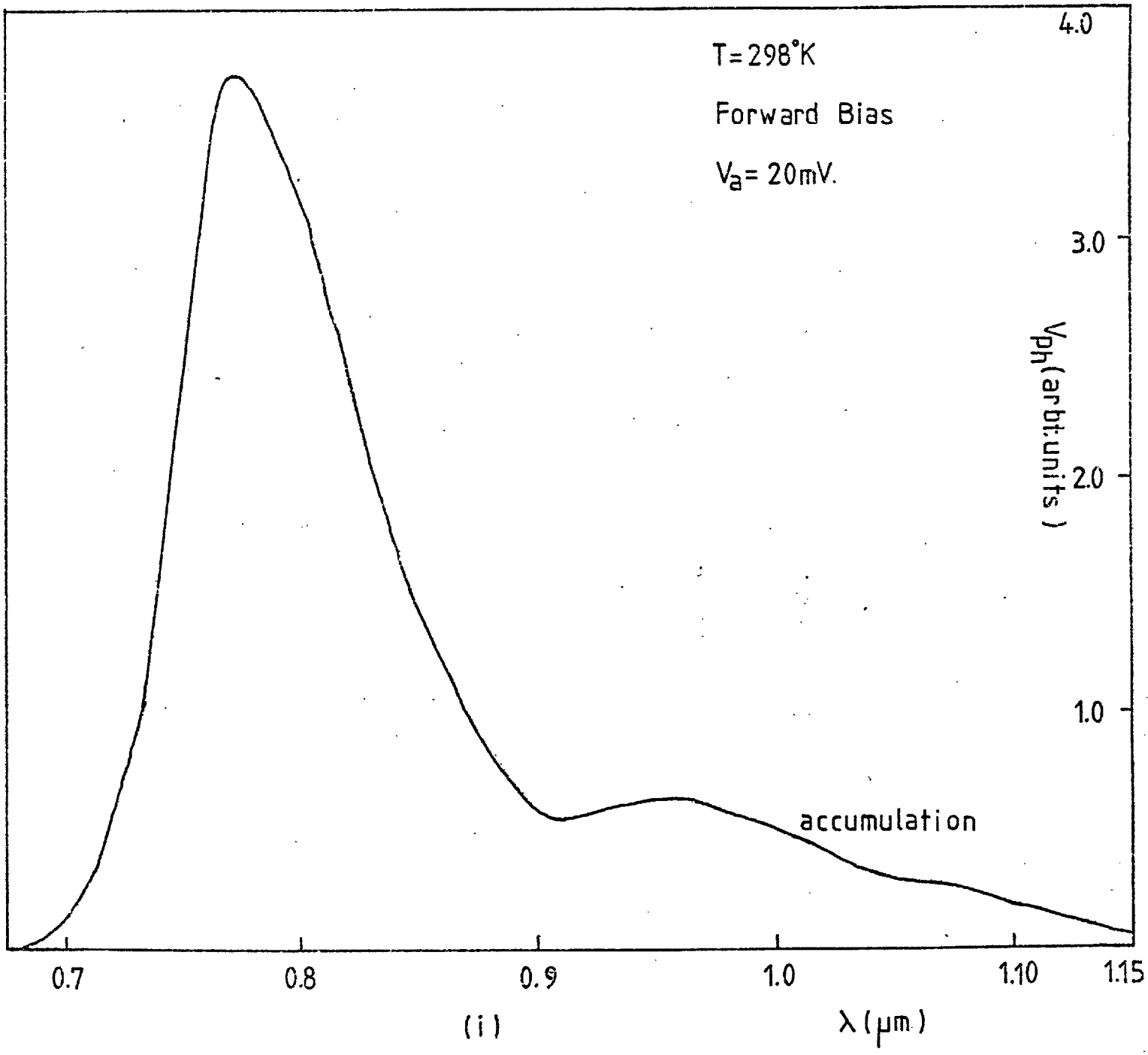

Fig. 6.12a Typical Forward Bias Photovoltaic Results

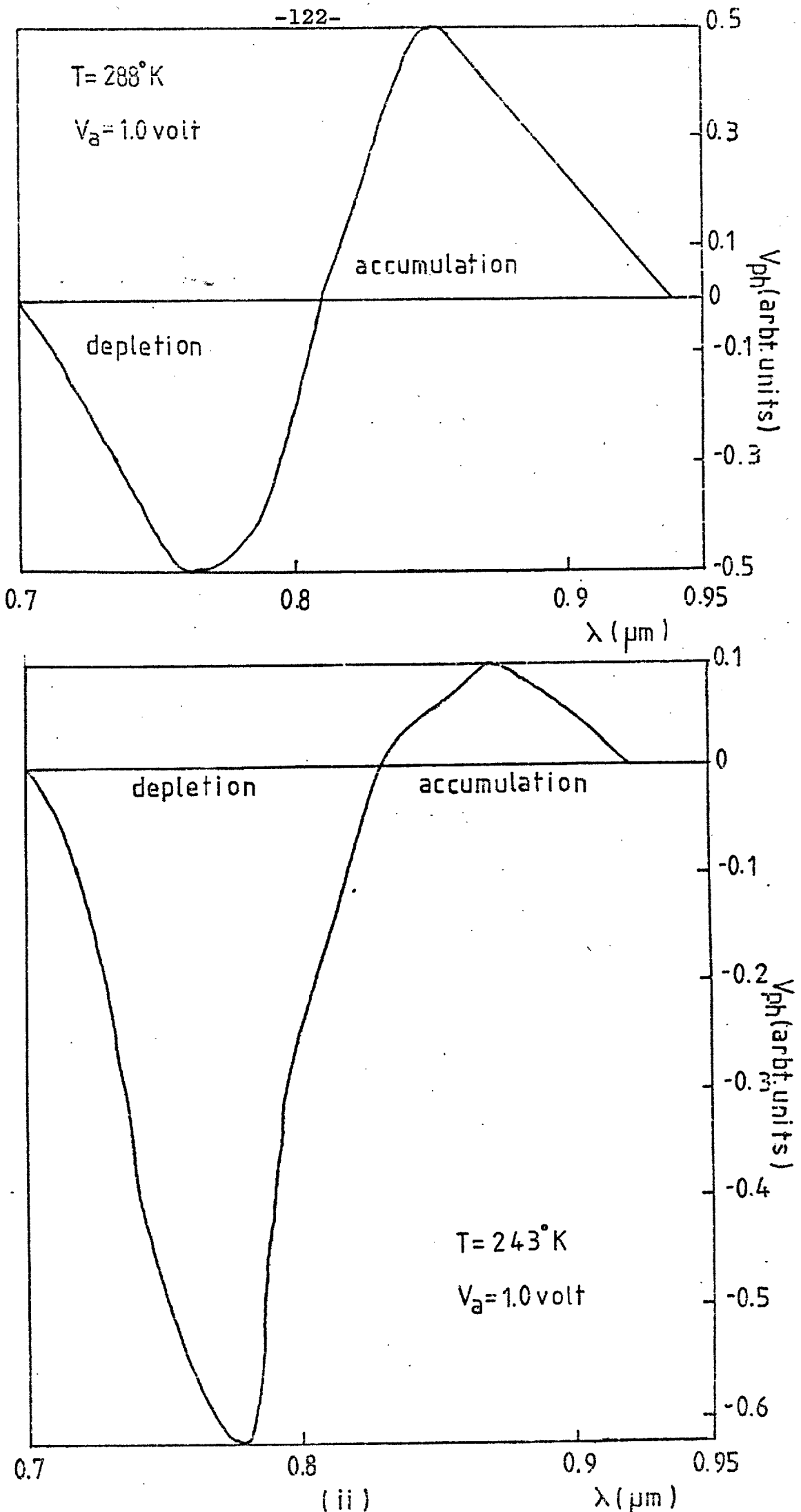

Fig.6.12a Typical Forward Bias Photovoltaic Results

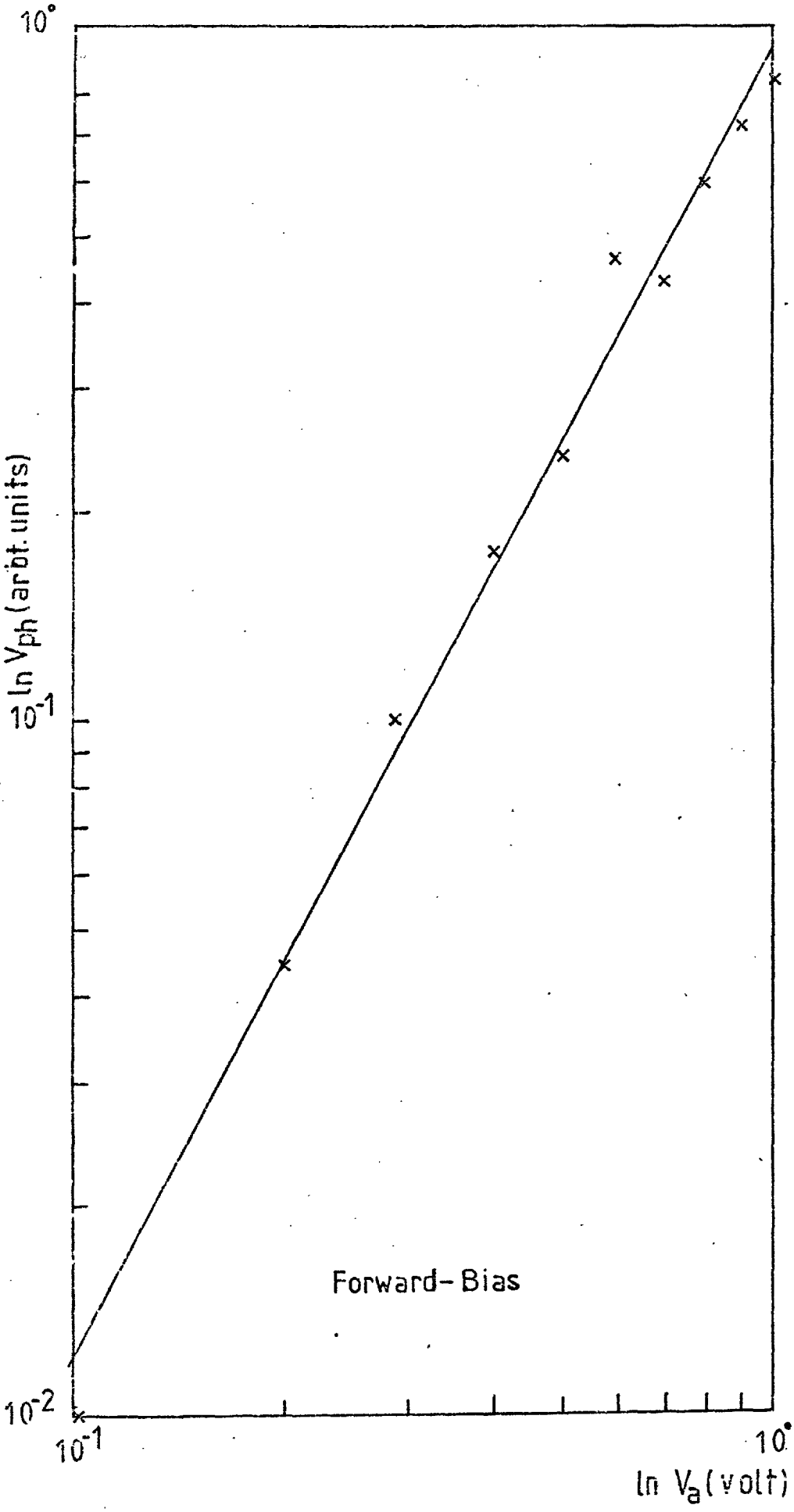

Fig.6.12b Photovoltage-Bias Voltage Relation

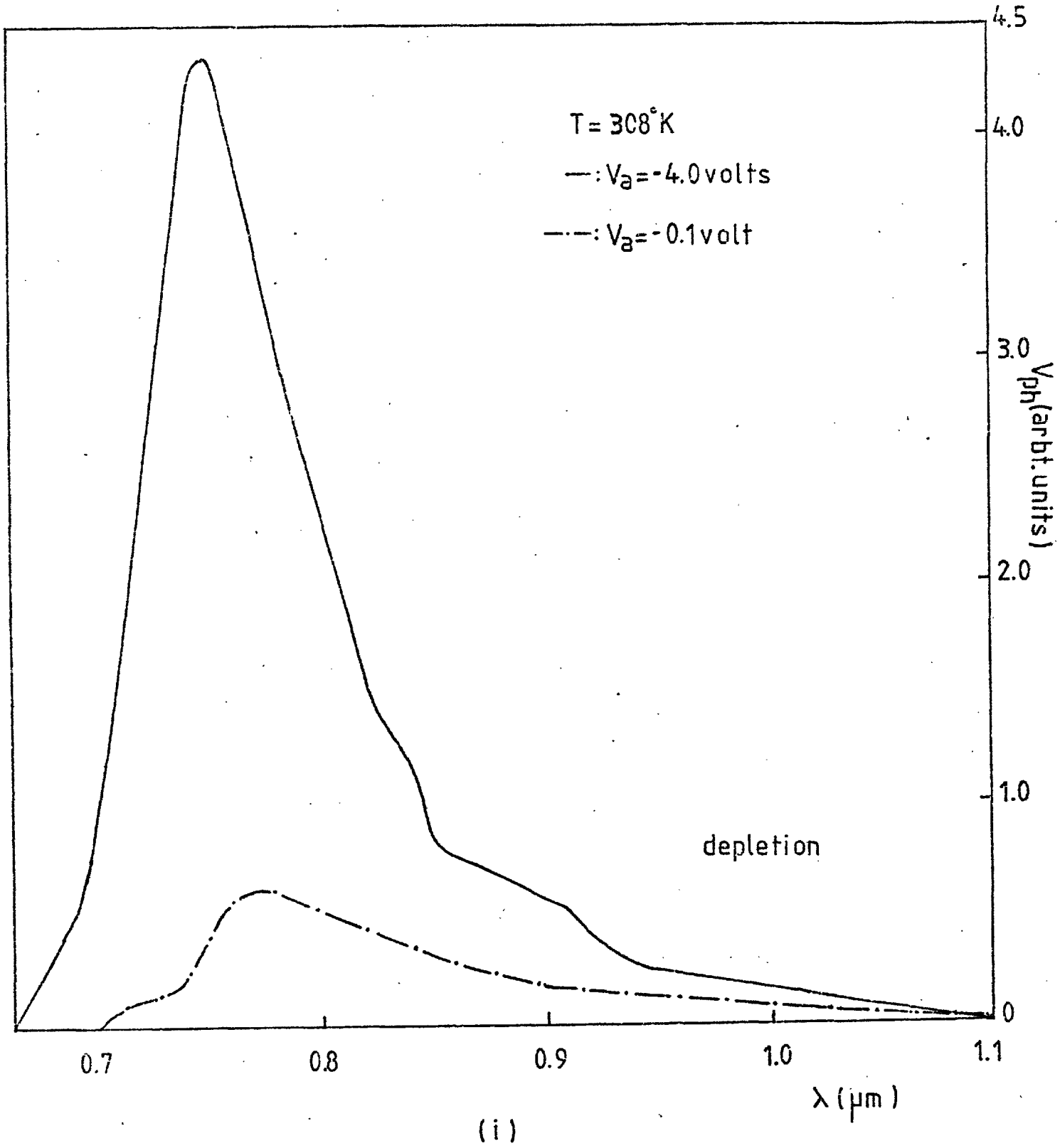

Fig.6.13a Typical Reverse Bias Photovoltaic Results

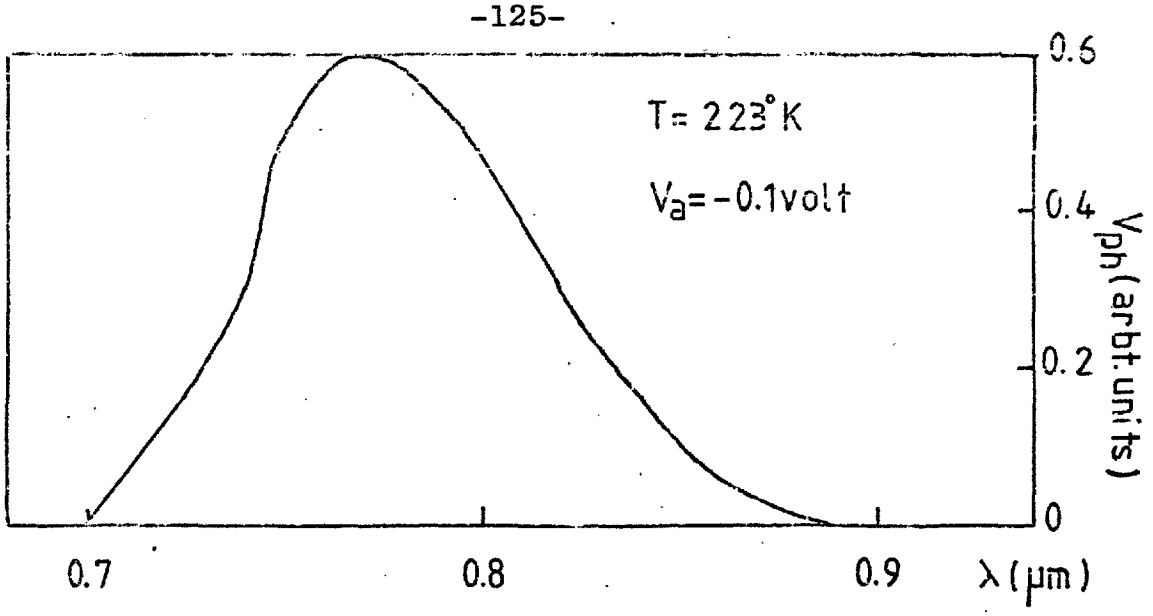

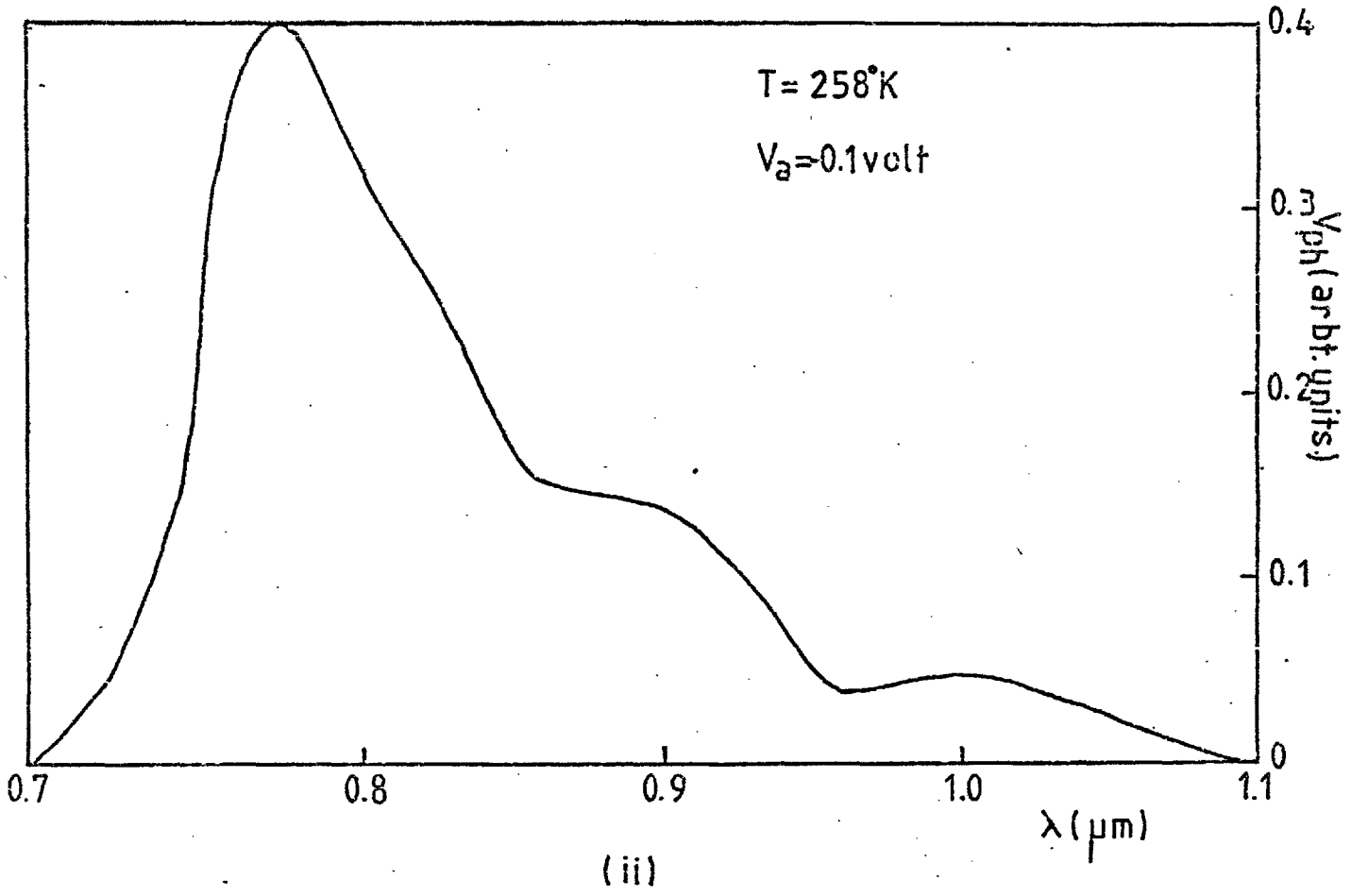

(ii)

Fig. 6.13a Typical Reverse Bias Photovoltaic Results

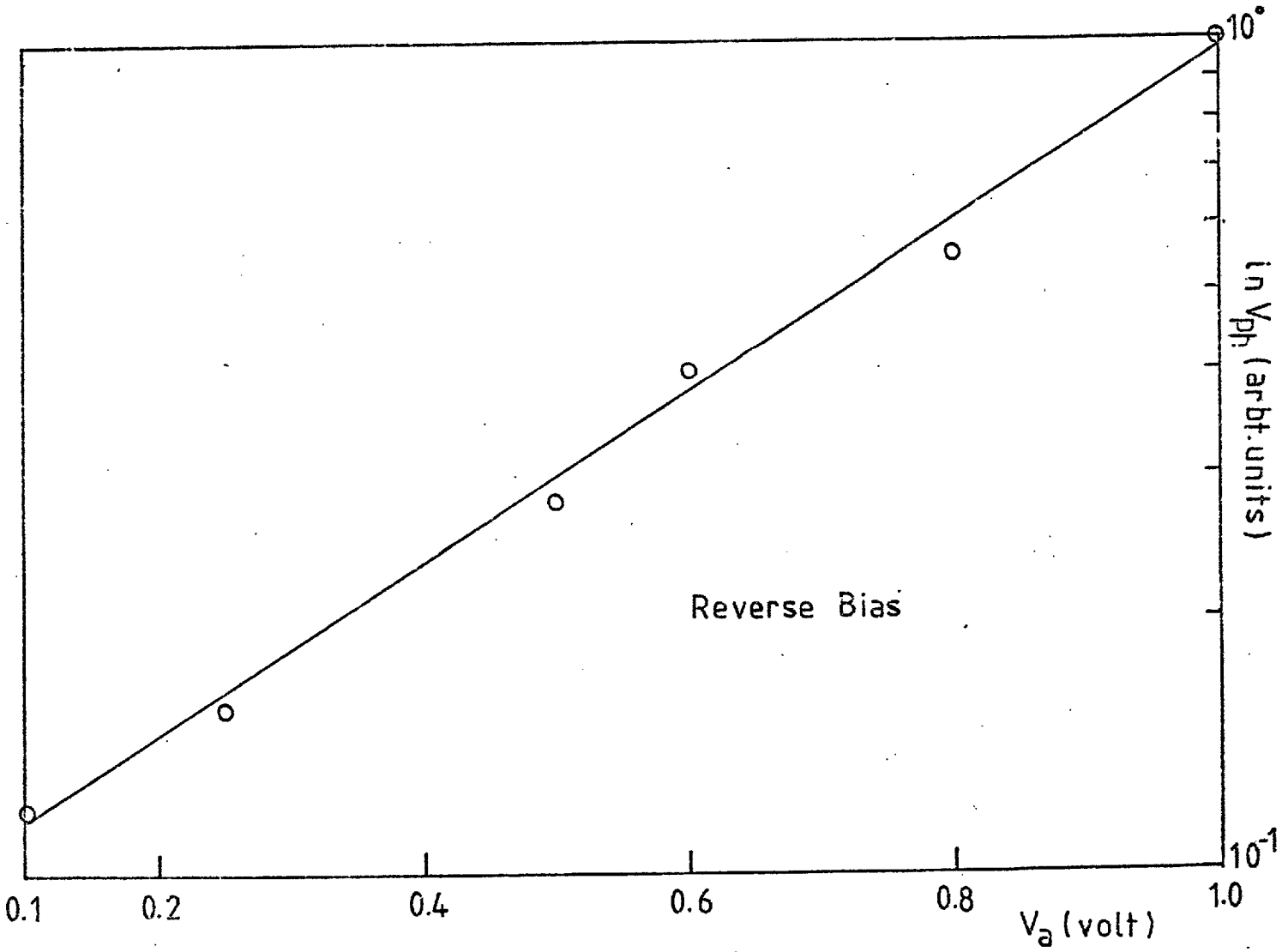

Fig.6.13b Photovoltage– Bias Voltage Relation

$$V_{ph} \propto \exp -(|V_a|/V_o) \qquad (6.6a)$$

where V_o was a constant, and since, again, $I_{ph} \propto V_{ph}$,

$$I_{ph} \propto \exp -(|V_a|/V_o) \qquad (6.6b)$$

The wavelength range for the production of photovoltage was approximately the same as for zero bias. The lower energy response due to traps was also observed in this case but was too diffuse to be analysed.

It is clear that in the two cases above, different current rate limiting factors are probably involved for the two bias conditions (cf. eqns. (6.5) and (6.6)). Photoconduction in forward bias is probably space charge limited as eqn. (6.6) show that photocurrent is a function of bias voltage squared. However, reverse biased photocurrent has a similar conduction mechanism to that observed in D.C. voltage case (cf. section 6.1). The observation of an accumulation in forward bias, and the dependence of the change to depletion depending on temperature and bias voltage, indicates that fermi level is probably pinned at the interface, and the fermi level within the crystallites alone change with temperature and applied bias. The conduction mechanism under reverse bias may be dominated by a tunnelling process.

(iii) Temperature dependence

Fig. 6.14 shows that thermal emission is observed,

$$V_{ph} \alpha \exp(-\Delta E/kT) \qquad (6.7a)$$

or as $I_{ph} \alpha V_{ph}$,

$$I_{ph} \alpha \exp(-\Delta E/kt) \qquad (6.7b)$$

The thermal activation energy, ΔE, which can be evaluated from the gradients of fig. 6.14, has a value of 0.4 (±0.1) eV and 0.16 (±0.01) eV. Thus, it implied that during photoactivation process, thermal emission process was involved as well. Width of space charge at the junction was estimated by taking the difference of the values of the wavelengths corresponding to $^1/e$ of the peak : 1.4×10^{-7} m (forward bias), 1.8×10^{-7} m (reverse bias), 1.6×10^{-7} m (zero bias). Temperature independence of V_{ph} was observed above room temperature.

6.3 THERMALLY STIMULATED CURRENT MEASUREMENT RESULTS

Thermally stimulated current measurements have been used to determine the trap distribution in the heterojunction, in order to assess the effect of trapped electrons in the fields. A bias voltage of (+ or -) 1.5 volts was applied across the sample for 105 mins in the dark, and T.S.C. was measured for zero bias. Three main current peaks were observed:-

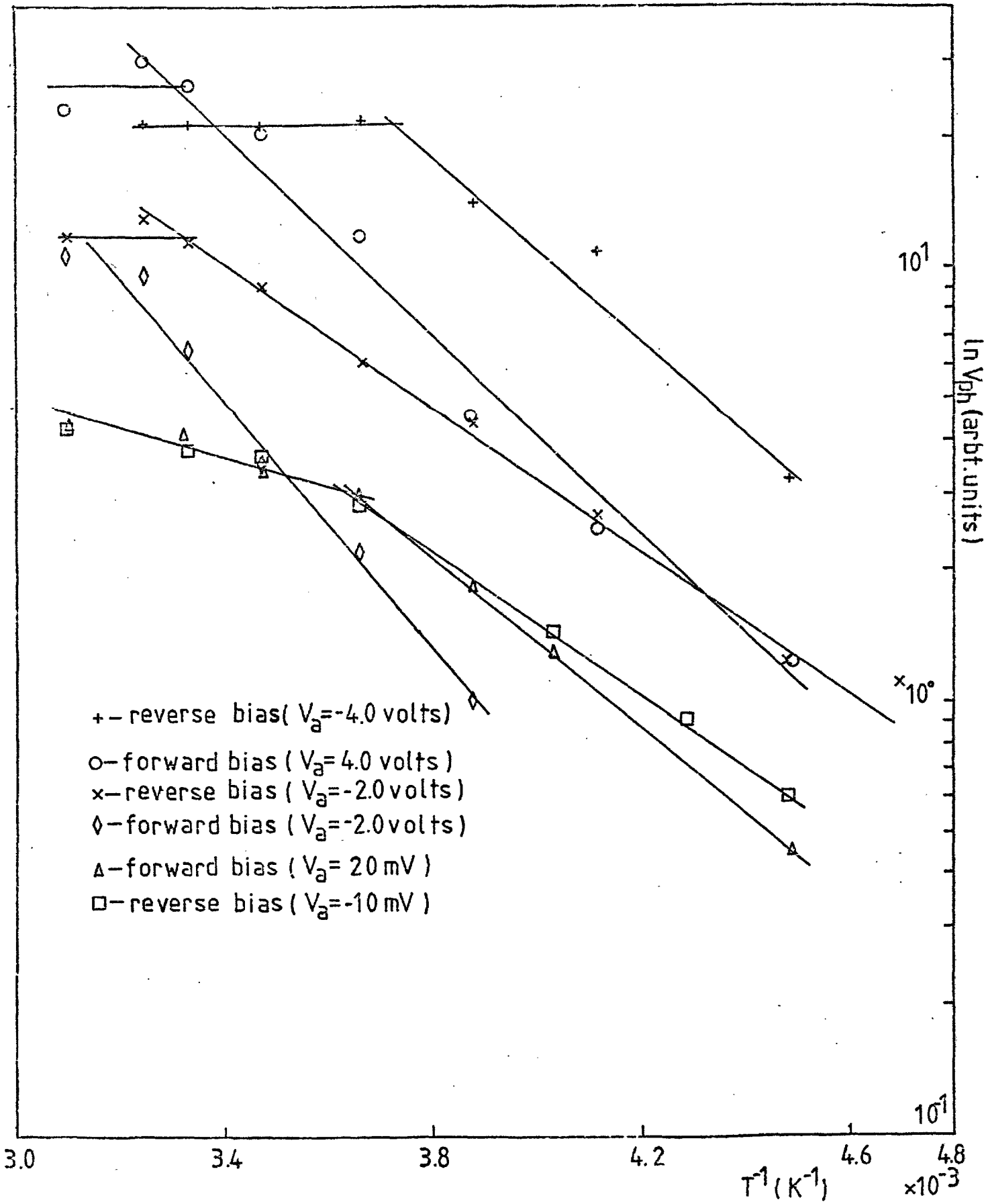

Fig.6.14 Photovoltage–Temperature Relation

(i) A low temperature peak

A broad peak was observed with a maximum at temperature ∿203K and further measurement revealed that at least two traps were contributing to the peak (fig. 6.15a). The trap density was estimated from the area beneath the peak (∿6 x 10^{15} cm^{-3}). Initial rise method (see below) (Garlick and Gibson, 1948) gave activation energy ∿0.15 ± 0.05 eV (Fig. 6.16a). However, the peak was diffuse and small, and it was not possible to derive much information about the traps from this peak.

(ii) A room temperature peak

T_{max} was 291°K for this peak and the response was bigger than that observed for the low temperature peak and using the initial rise method (Garlick and Gibson, 1948):

$$I_s \alpha \exp(-\Delta E/kt) \qquad (6.8)$$

where ΔE is the trap depth/potential. ΔE could be obtained from the gradient (fig. 6.16b) and an average value of 0.55 (±0.02) eV was obtained. The trap density was found to be of the order of 2 x 10^{17} cm^{-3}.

By applying a conditional equation proposed by Simmons and Taylor (1974), we obtain

$$\Delta T = 2kT^2_m/\Delta E \qquad (6.9)$$

where ΔT is the temperature width of the half height of the peak. The condition is derived from the transcendental function of the thermal emission current equation. An approximate agreement between LHS and RHS of eqn. (6.9)

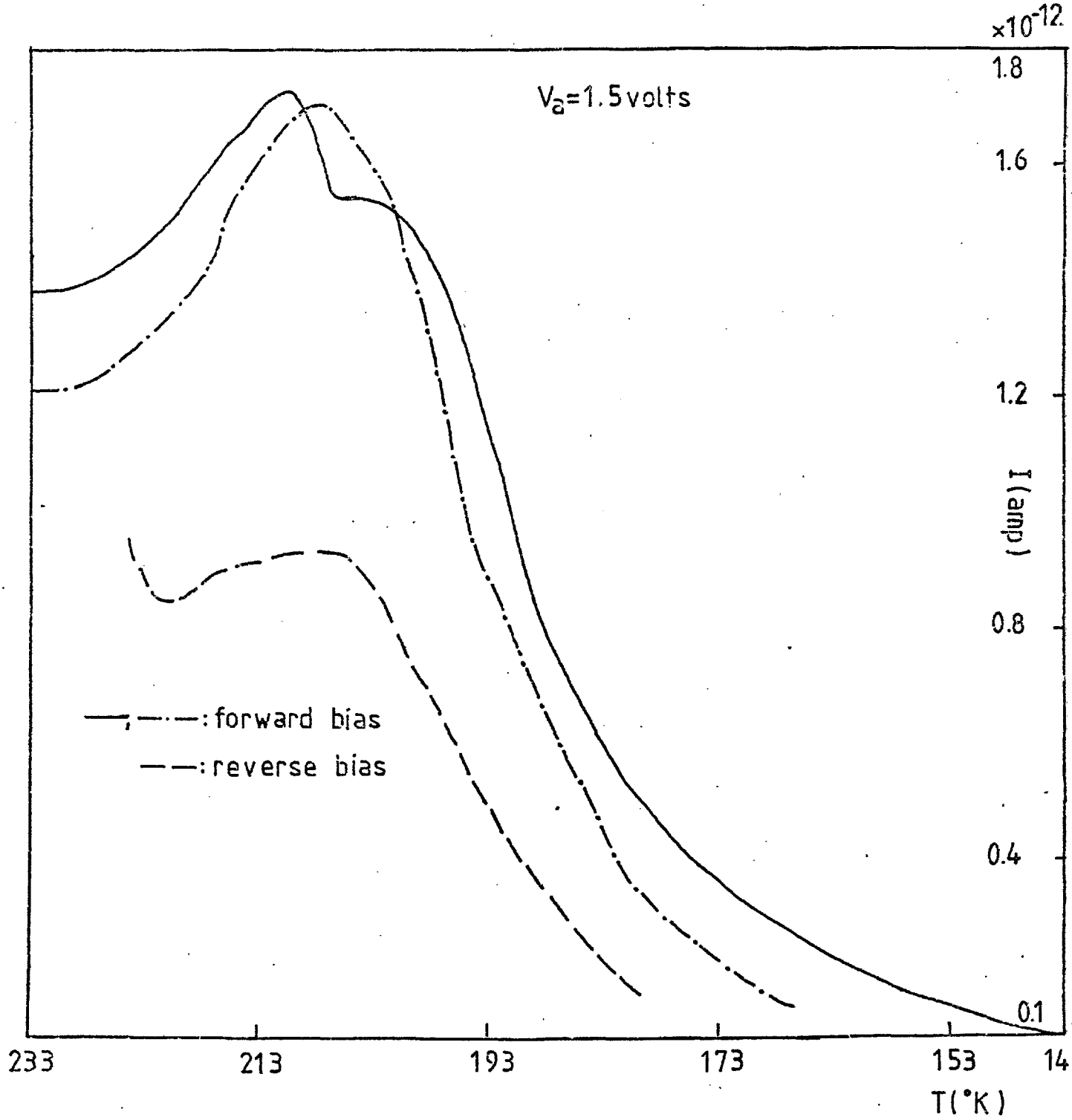

Fig.6.15a T.S.C. Result — Low Temperature Peak

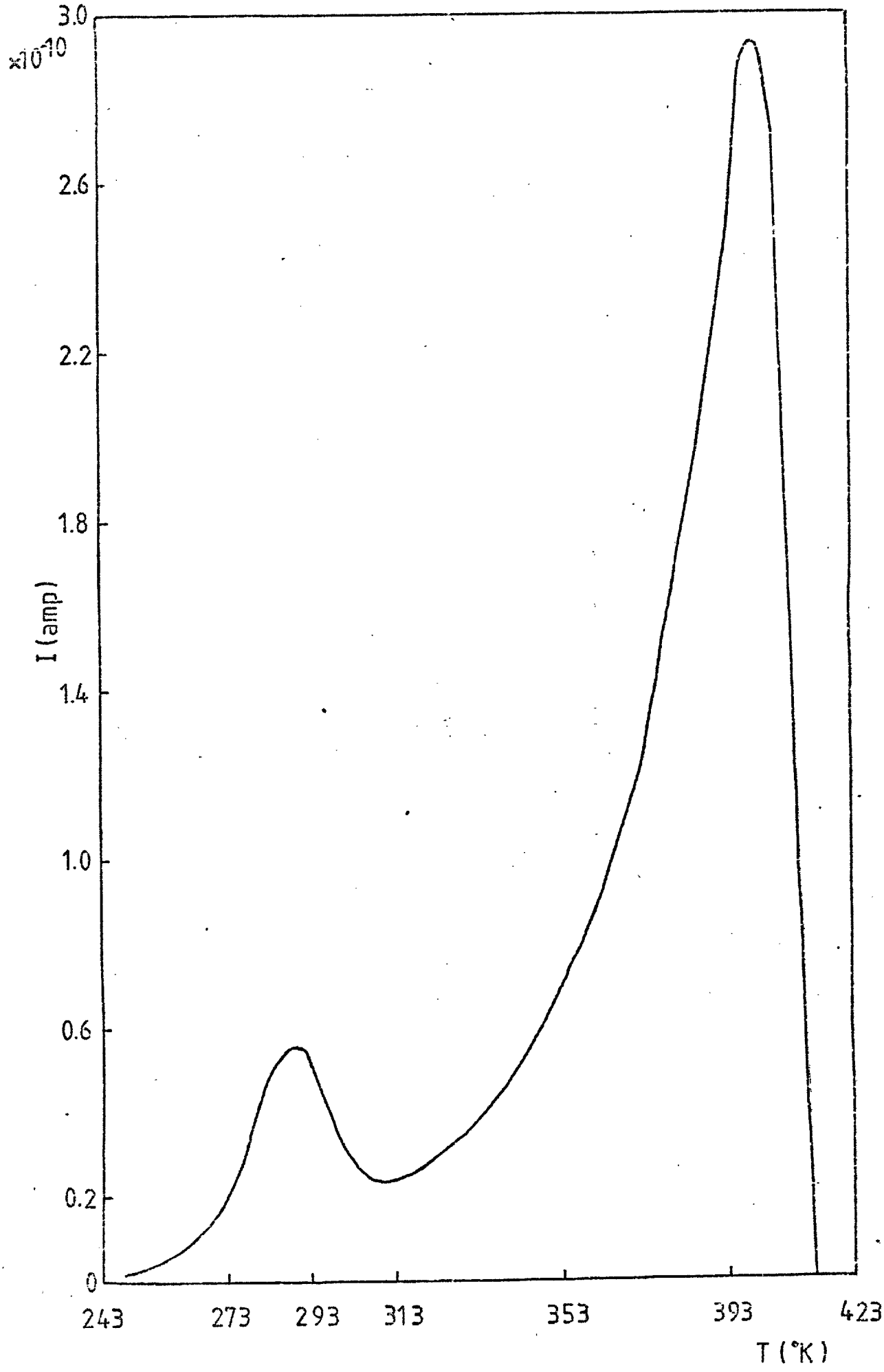

Fig. 6.15b T.S.C Room and High Temperature Peaks

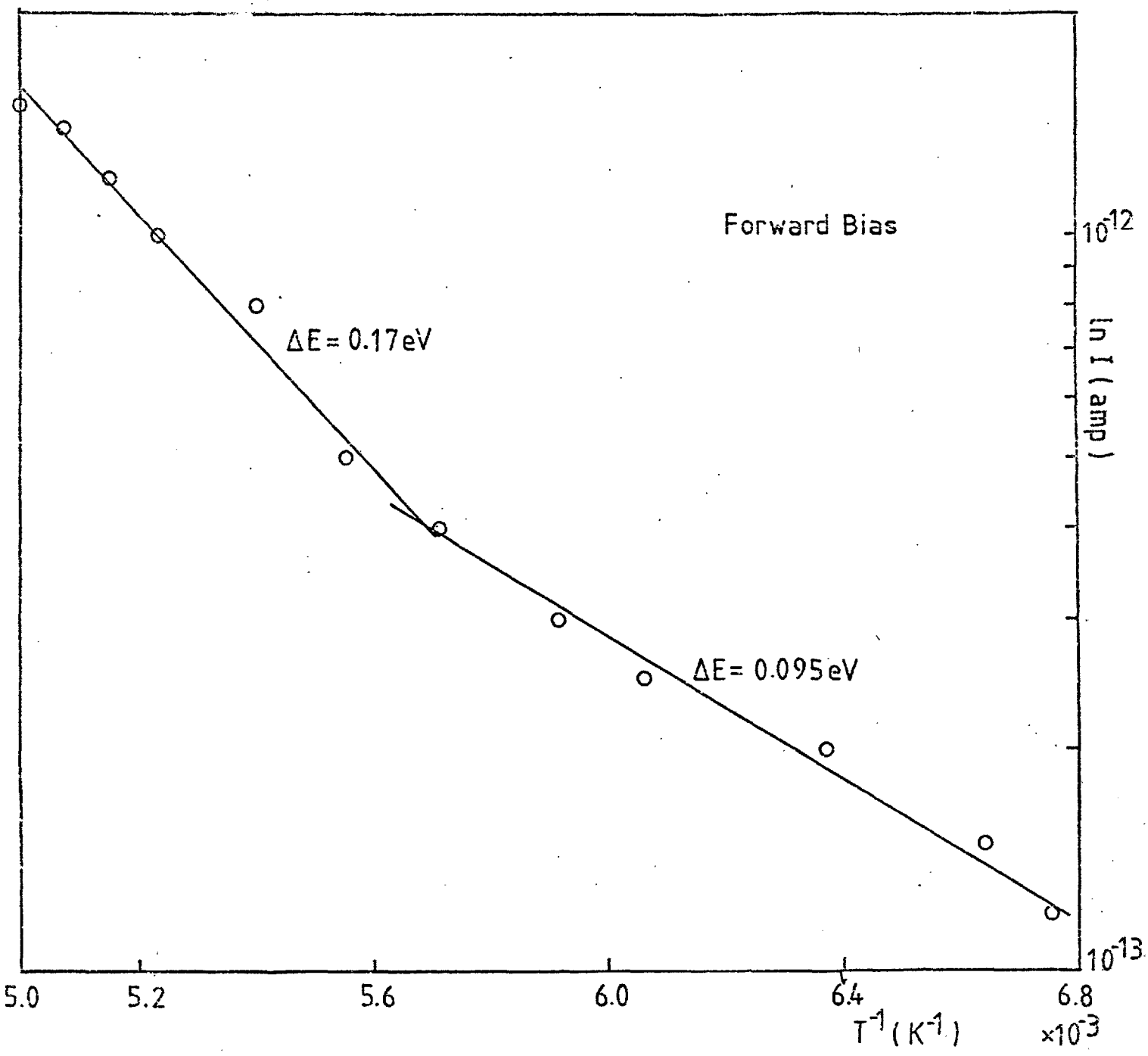

Fig.6.16a Activation Energies of Low Temperature Peak

would indicate that this is a discrete trap. For room temperature peak, consider $\Delta E = 0.55$ eV, ΔT was found to be $27^{o}K$, and $T_m = 292.5^{o}K$,

Then,

$$2kT_m^2/\Delta E = 26.8$$

Thus,

$$\Delta T \simeq 2kT_m^2/\Delta E$$

i.e. the peak contained a discrete trap.

(iii) High temperature peak.

This trap gave rise to the largest response of the three observed and peaked at $400^{o}K$ (fig. 6.15b), with an approximate trap density $\sim 10^{18}$ cm^{-3}. The trap depth, using eqn. (6.9), was of the order of 0.32 eV (fig. 6.16c), which was shallower than the two other peaks at lower temperatures. This is not possible hence the trap depth must be distorted. Also application of eqn. (6.10) revealed that $T \neq 2kT_m^2/\Delta E$, i.e. the trap is not discrete or the trap potential is distorted by the high localised field due to high trap density.

The high temperature peak appeared to be due to the dominant trap as it leads to the highest trap density and does not fully discharge until a temperature of $400^{o}K$ is reached. This result implies that most of the traps were still filled at room temperature.

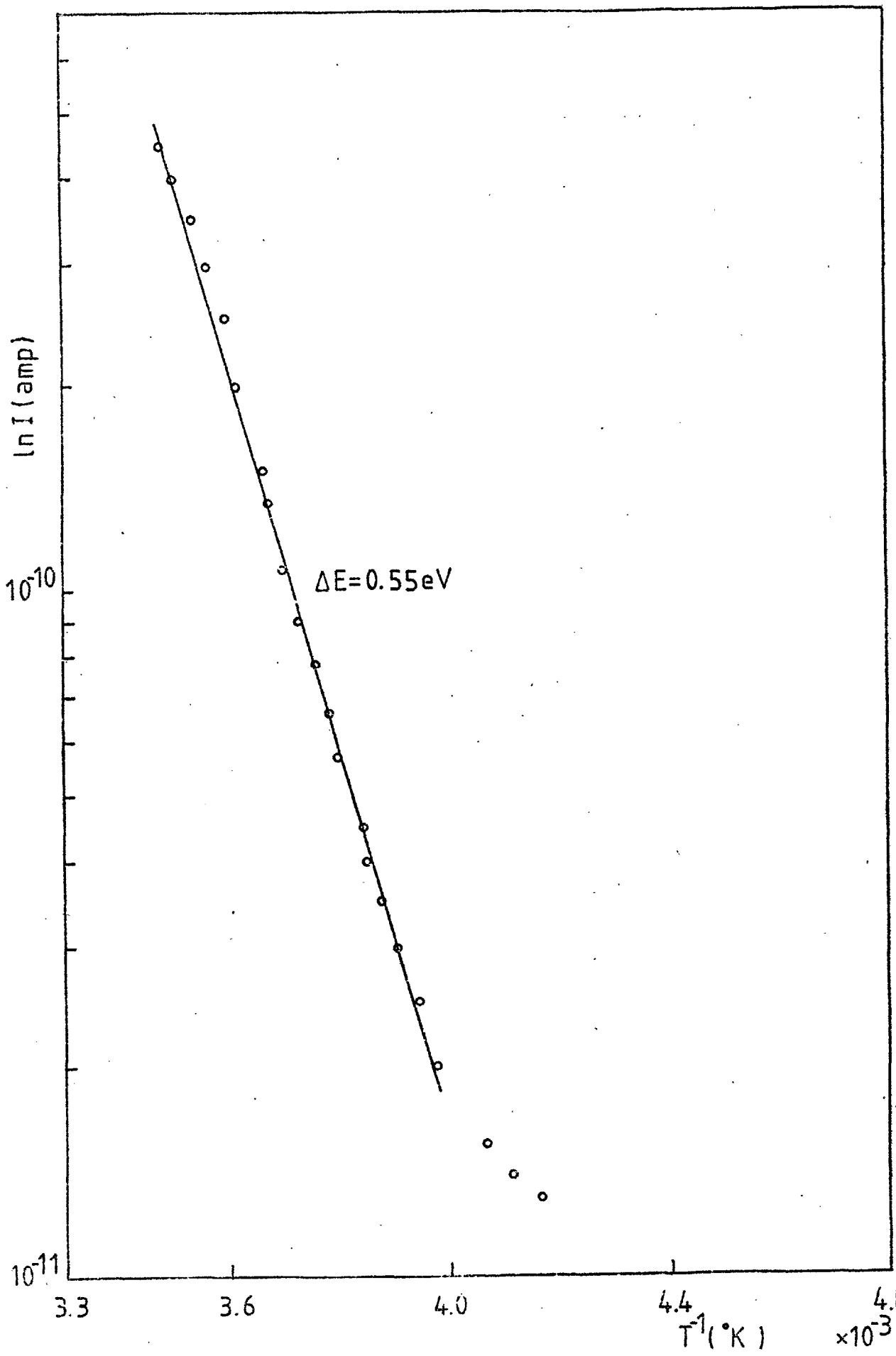

Fig. 6.16b Activation Energy of Room Temperature Peak

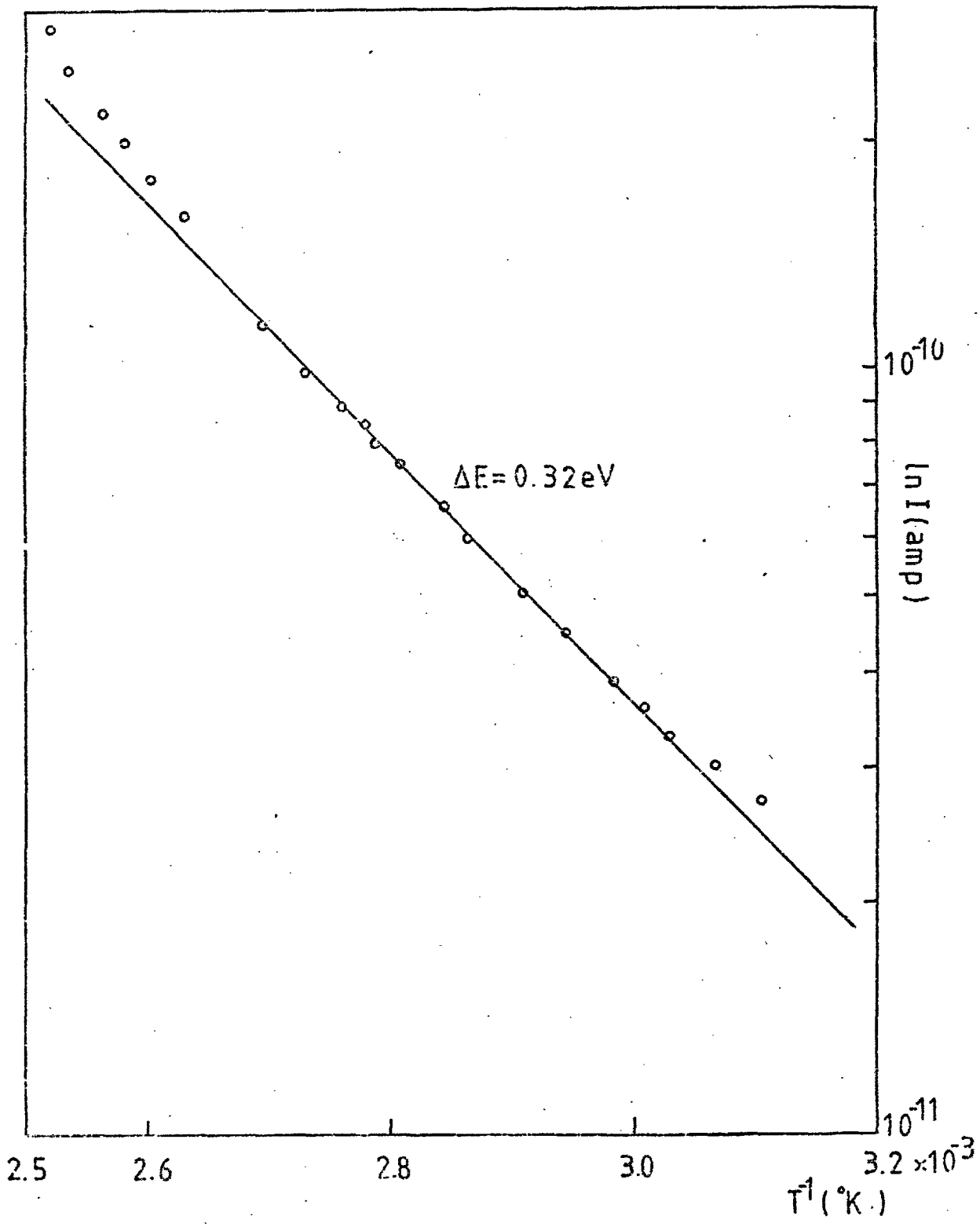

Fig.6.16c Activation Energy of High Temperature Peak

6.4 MICROSTRUCTURE OF THE HETEROJUNCTION FILM

The heterojunction was cut normal to its surface in order to observe the layer structure under the scanning electron microscope (Cambridge Scientific Instruments Ltd.- Stereoscan 600). The micrographs show two distinct layers (fig. 6.17a) of thickness about 1 μm and 2 μm respectively. The layers consisted of columnar crystals which did not extend in all cases across the film. The width of the crystallites range from 0.12 μm to 0.3 μm. The columnar structure is similar to those observed by Pawlewicz et al. (1976) in sputtered CdTe films.

X-ray diffraction of the heterojunction film using a cylindrical texture camera showed that CdTe had a zincblende structure, whereas CdSe existed as a mixture material with both cubic and wurzite structures (fig. 6.17b).

6.5 DISCUSSION

Eqn. (6.1) obtained from d.c. current-voltage results applied also to the photovoltaic effect in reverse bias. With a weak temperature dependent relation, eqn. (2.58) bore a closed resemblance to eqn. (6.1). To derive eqn. (2.58), Riben and Feucht (1966b) have applied the principle used by Chynoweth et al. (1961) and Classen (1961) to calculate the excess current observed in an Esaki junction. In this work, the tunnelling equation by Chynoweth et al. (1961) is used because although it is almost identical to eqn. (2.58), it is essentially temperature independent.

a

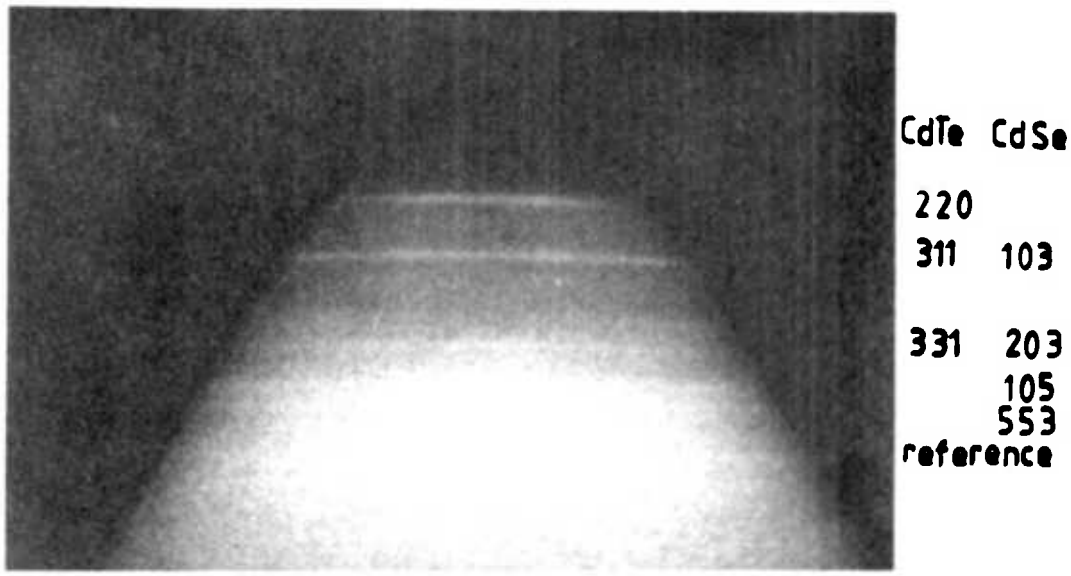

b

Fig.6.17 a) Cross-Section of a pCdTe-nCdSe Heterojunction

b) Texture X-ray Diffraction Pattern of pCdTe-nCdSe Heterojunction

Writing the tunnelling equation in the form:

$$J = J_o \exp(V_a / V_o) \tag{6.9}$$

where

$$J_o = BN_t \exp(-V_p / V_o)$$

$$V_o = 2(\alpha e^{3/2} K_n W_n)^{-1} \quad , \; n = 1,2$$

$$\alpha = 4(2m^*)^{\frac{1}{2}}/(3eh)$$

W is the width of the junction

$$K_2 = [1+(Na_2\varepsilon_2)/(N_{d1}\varepsilon_1)]^{-1} \quad , \; K_1 = 1 - K_2$$

and,

B is constant.

B can be evaluated by substituting experiment results into eqn. (6.9). For N_t, the trap density of high temperature peak is used. V_o is obtained from d.c. current-voltage results and qV_D = 2.17 eV, is obtained in the following way (Hipwood, 1977; fig. 4.4),

$$V_D = \phi_2 - \phi_1$$

$$\therefore \quad V_D = [\chi_2 + E_{g2}-(E_{f2}-E_{c2})] - [\chi_1 + (E_{c1}-E_{F1})]$$

as $\Delta E_c \equiv \chi_2 - \chi_1$,

$$\therefore \quad V_D = \Delta E_c + E_{g2} - kT \, \ell n\left[\frac{N_{D1}N_{A2}}{N_{c1}N_{V1}}\right] \tag{6.10}$$

assuming that all donors/acceptors are ionised at room temperature and Boltzman statistics apply. Values of B

are listed in table 6.1, and it can be seen that they fall into three groups with: $B \sim 6 \times 10^{-21}$ amp-cm; $B \sim 10^{-19}$ am-cm and $B \sim 10^{-14}$ amp-cm. This result may depend on the possibility of a number of parallel conduction paths (figs. 6.1 and 6.2). B is then a constant for one of the electrical paths and each path has a different value of B.

Thus, eqn. (6.9) depicts a heterojunction dominated by tunnelling of carriers through the junction potential with possibly one or more electrical paths in each crystallite. Since the current-voltage characteristics are symmetrical (figs. 6.1, 6.2 and 6.5a), that is the tunnelling current is about the same under both forward and reverse bias. This means that the potential on either side of the junction is approximately the same.

Eqn. (6.9) can also be used to evaluate the junction width, using the relation:

$$V_o = 2/(\alpha e^{3/2} KW)$$

For simplicity, the assumption that $K_1=K_2=K=0.5$ has been made during evaluation of W and B. Table 6.4 lists the values of W obtained. Most values of table 6.1 are about two orders of magnitude smaller than the values obtained from the photovoltaic measurement, which are 1.4×10^{-7}m(forward bias), 1.8×10^{-7}m (reverse bias), and 1.6×10^{-7}m (zero bias). Theoretical values of the junction width can be obtained by using eqn. (2.1), derived from Anderson's theory (Anderson, 1960). Taking the donor and acceptor densities

to be 10^{23} m^{-3} (Cheah, 1976) and bias voltage of 1 volt; the junction widths are: 1.3×10^{-7}m (forward bias); 2.1×10^{-7}m (reverse bias); and 1.7×10^{-7}m(zero bias). The theoretical values are in excellent agreement with the photovoltaic results. However, if the interface states are assumed to dominate and are localised within the theoretical junction width, $\sim 10^{-7}$m, then the T.S.C. high temperature peak would give a trap density of $\sim 10^{24} m^{-3}$. Substituting the trap density into eqn. (2.1) gives the junction width as 1.7×10^{-8}m (forward bias); 2.7×10^{-8}m (reverse bias); and 2.2×10^{-8}m (zero bias). Some results from table 6.4 agree with the above calculated junction widths but in general they are an order of magnitude smaller. Part of the discrepancy can be due to the approximation made during the evaluation of the probability of tunnelling. Price (1962) has shown that the tunnelling probability calculated using free electron approximation has a larger value. This in fact means that the factor in the exponential term of the tunnelling probability (Chynoweth et al, 1961)

$$P \simeq \exp(-\alpha E^{3/2}/F)$$

should be larger in order to have a smaller tunnelling probability. Thus the junction width would be correspondingly larger. Another consideration is the ideal conditions for which eqn. (2.1) is derived whereby single crystal condition is assumed. The junction width calculated by eqn. (6.9) could be termed the tunnelling width because the equation describes where the tunnelling takes place,whereas eqn. (2.1)

describes where the space charge would extend. The same principle lies behind the evaluation of junction width from photovoltaic results. Since to tunnel a carrier would require to be activated to a point where the potential barrier is thin enough for tunnelling to occur.

In order to conform to the conduction process described above, the junction potential would need to be narrow appreciably as it gets near the junction but also should diffuse as it gets further away from the junction. Eqn. (2.26) describes an exponential potential which may not be narrow enough near the junction (fig. 6.18). Another approach is to consider the trapped charge at the interface as a sheet of monopole charge with trapping density $N_t m^{-3}$. The electrostatic field due to the charged surface would be,

$$F_{IS} = (qN_t)/(4\pi\varepsilon_o\varepsilon_1 x^2) \qquad (6.11)$$

(N.B. since $\varepsilon_1 \sim \varepsilon_2$, F_{IS} is approximately the same on either side of the interface.)

Thus, the potential of the charged surface is,

$$\frac{dV}{dX} = qN_t/(4\pi\varepsilon_o\varepsilon_1 x^2)$$

$$V_1 = \frac{qN_t}{4\pi\varepsilon_o\varepsilon_1} \int_o^{x_1} \frac{1}{x^2}\, dx$$

$$\therefore \quad V_1 = \frac{qN_t}{4\pi\varepsilon_o\varepsilon_1} \quad \frac{1}{x_1} \qquad (6.12)$$

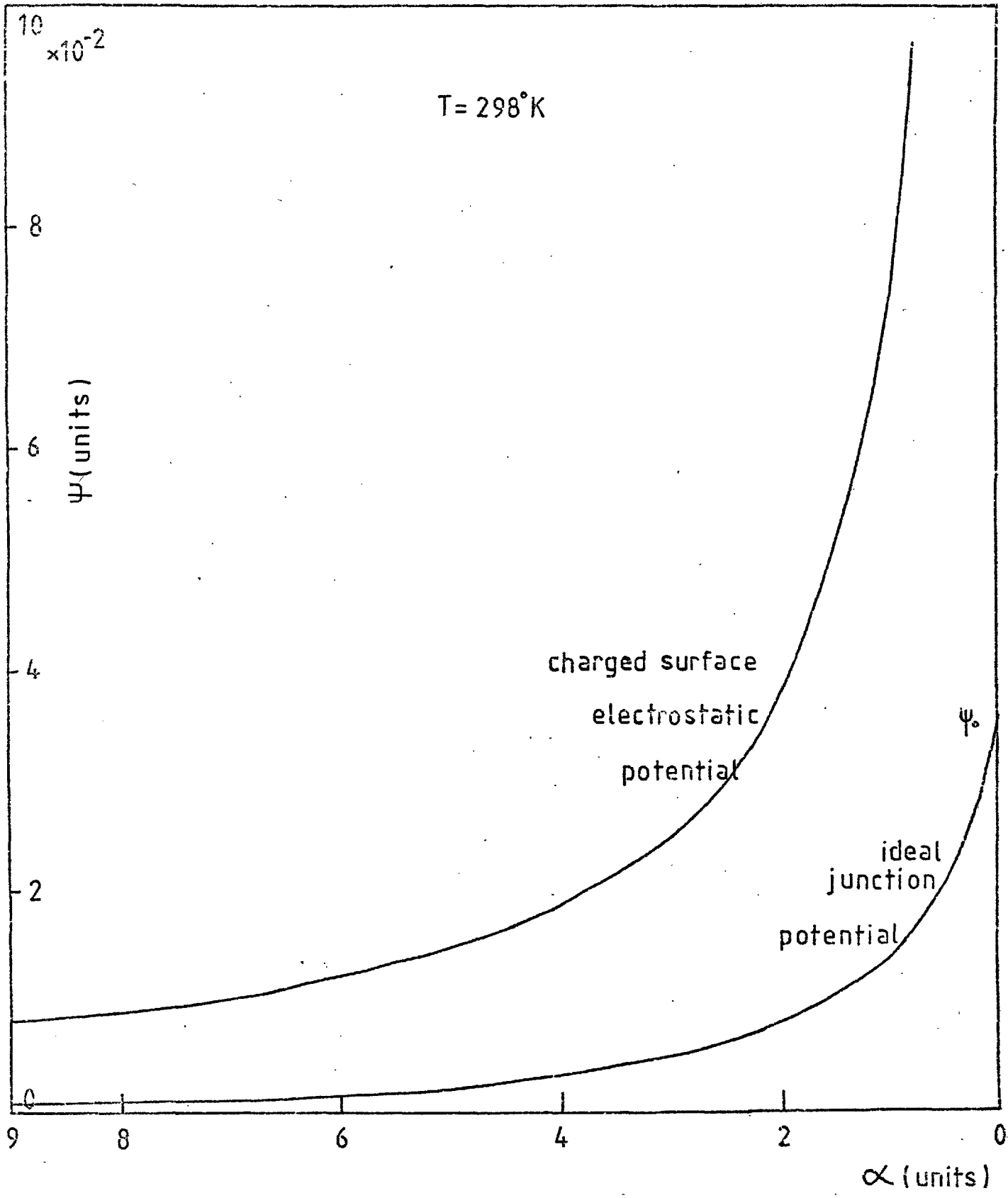

Fig. 6.18 Theoretical Potential Profiles at the Interface

This potential compared to the junction potential derived from eqn. (2.26) which is describing the potential without interface states shows that the electrostatic potential of a sheet charge is bigger than that derived from eqn. (2.26) (fig. 6.18). Hence from this simple approach one can approximate when interface states dominate the heterojunction characteristic with a junction potential not too different from that of a charged surface. Further support for the charged surface approximation validity comes from TSC results which show that the trapped carriers of interface states are not released until a temperature of $400^{o}K$ and above is reached. Thus, at room temperature, the majority of the trapped carriers remain at the interface.

The effect of interface states can also be observed in the a.c. current-voltage and capacitance-frequency results. They showed that the junction impedance is not inversely proportional to the frequency, ω, but inversely proportional to $\omega^{1.3}$, and has a low pass filter characteristic. This implies that the impedance (fig. 6.9) in parallel with the capacitance is frequency dependent.

This agrees with the a.c. current-voltage equations derived from theory (section 2.34b). From eqns. (2.51) and (2.52), if interface states dominate, then they can be approximated to,

$$J_{11}(t) \sim \omega C_f(Q_1) \quad (\psi_{D1} - \psi_{a1}) \tag{6.13a}$$

$$J_{21}(t) \sim \omega C_f(Q_2) \quad (\psi_{D} - \psi_{a1}) \tag{6.13b}$$

Thus, the a.c. current-voltage would be linear and the impedance is inversely proportional to ωC_f. Since C_f is also frequency dependent, Z_{AC} would not be inversely proportional to ω, as observed, and the exponential relation of frequency-current in eqn. (6.2) can be due to the first term of eqns. (2.51) and (2.52), and/or C_f. The complexity of C_f (eqn. 2.48) prevents further theoretical analysis.

Although the interface states dominate the heterojunction characteristic, donors/acceptors within crystallites can still be distinguished from both TSC and photovoltaic results where photoexcited carriers are trapped by the donors/acceptors, later thermally released into conduction/valence band or vice versa. Fig. 4.2 shows some donors/acceptors that might be held responsible, e.g. Cd_i'' in n-CdSe with activation energies 0.24 - 0.45 eV (Manfredottic et al, 1973), and V_{cd}', V_{cd}'' and Au_{cd}' in p-CdTe with activation energies 0.15, 0.6 and 0.3 eV respectively.

The heterojunction is therefore considered to have a junction with a high density of interface states. Tunnelling occurs at the interface and fermi level is pinned at the interface due to the high density of traps. Forward biasing the heterojunction could turn the depletion region of the junction into accumulation. The sharp rise in potential near the junction (fig. 6.18) would mean that changing from depletion to accumulation or vice versa could be slower than at a point further away from the junction. When the junction has changed into accumulation, tunnelling can still take place through inter-band tunnelling (fig. 6.19). But as more carriers are tunnelling through the junction, a

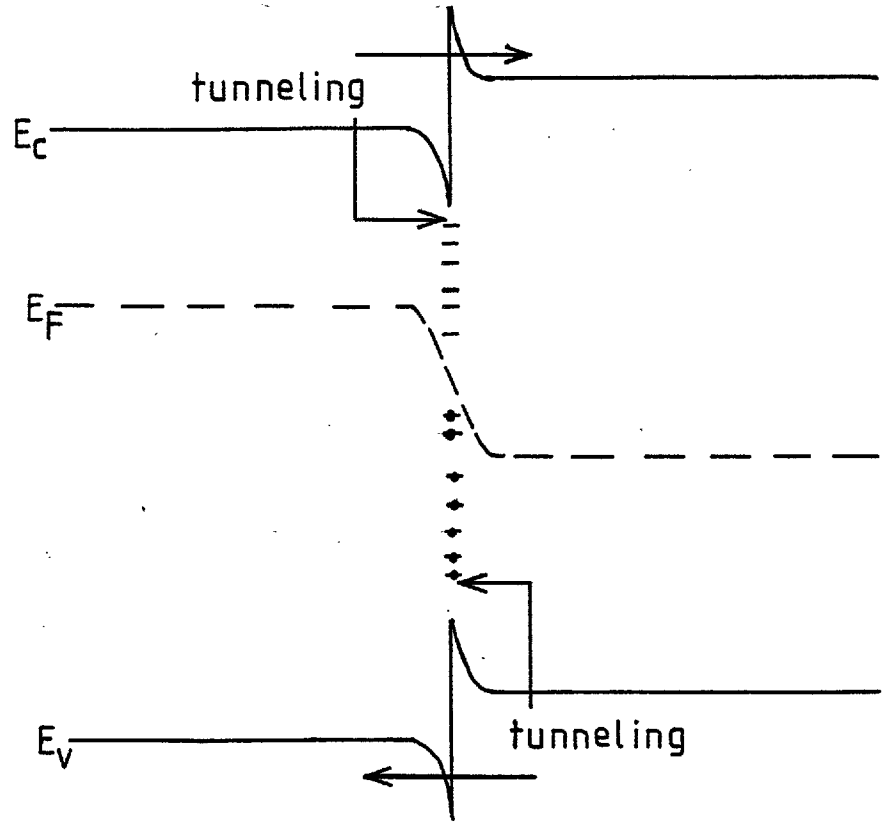

Fig. 6.19: Possible Tunneling Paths when the Heterojunction is Forward Based

space charge limited condition can occur at the proximity of the contacts to the heterojunction. This is observed in the forward biased photovoltaic results.

Nó effect of grain boundaries is observed, possibly due to the fact that most grain boundaries run orthogonally to the heterojunction surface, i.e. they are parallel to the direction of the current flows. Under these circumstances, grain boundaries do not generally affect the transport properties of the material significantly (Mataré, 1971).

CHAPTER 7

CONCLUSION

The transport mechanism of the pCdTe-nCdSe heterojunction is dominated by interface states which encourage carriers to tunnel into the interface where they recombine. The tunnelling process can be adequately described by the model proposed by Riben and Feucht (1966b), though in some cases Anderson's model also gives good agreement with the results. This result is surprising, as the heterojunction was fabricated by sputtering and consists of a thin film on an amorphous substrate. It is to be expected that the heterojunction would exhibit a complex conduction mechanism due to various electronic and structural defects, and the conduction of such a junction might not be dominated by thermal emission over the barrier. In this case, Anderson's theory would not be expected to give good agreement between theory and experiment. The fact that such agreement is observed could be due to the fact that the majority of the grain boundaries are parallel to the direction of the current flow, and, hence, exert little effect on the transport mechanism (Mataré, 1971). An energy band diagram of the heterojunction is proposed (fig. 7.1).based on the results obtained.

The dominance of the interface states was demonstrated by a comparison of the theoretical built-in potential for a junction without interface states and the electrostatic potential for a charged surface. The potential of a charged

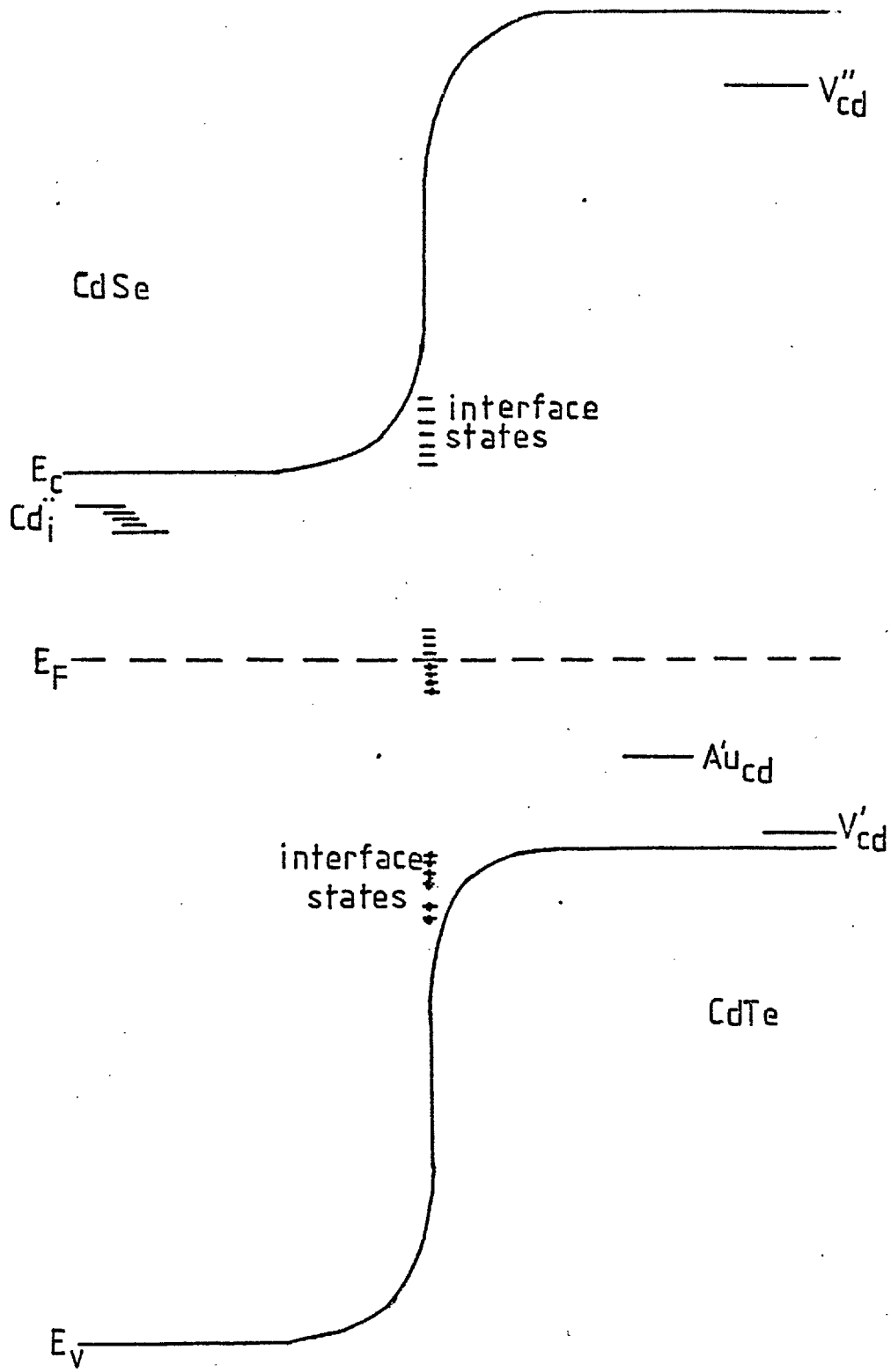

Fig. 7.1 Proposed Energy Band Diagram of

pCdTe–nCdSe Heterojunction

surface dominates (fig. 6.17).

With regard to the heterojunction as a potential solar cell, it was not possible to obtain experimentally the efficiency of photovoltage conversion, and the photovoltaic generated is disappointing. A bias voltage of at least one volt was required to get a maximum photovoltage of about 50 mV. This is not an encouraging result, and, certainly, heterojunctions of this type are not likely to produce commercially viable solar cells. To increase the photovoltage output, the tunnelling current has to be reduced to a minimum, and it is possible that this can be achieved through better crystallinity or, even, introducing localised impurity at the interface, neutralising the traps.

Heterojunction theory in general still has to come to terms with interface states. The existence of interface states in many heterojunctions has reduced the scope of the potential applications of heterojunctions severely. In fact, at the present time most workers are interested in heterojunctions with a small lattice mismatch, e.g. GaAs-$GaAs_xP_{1-x}$ heterojunctions. However, Mott (1967) and Hampshire (1975) have, respectively, pointed out that formation of localised states at the interface is inevitable even with perfect lattice matching and good agreement in thermal expansion coefficients. This is because at the interface, solutions of the Schrodinger's wave equation on both sides can be commutable, forming localised states. Thus, it seems that a more practical approach to the fabrication of good heterojunctions may be to attempt to reduce the activity of the interface states by the addition of suitable ion or atoms

to the interface region. Success in such an endeavour would increase the number of heterojunction applications substantially. One possible way to do this is to use ion implantation of doping atoms into heterojunctions constructed of one or two thin films. Since ion implantation can place dopants within well defined regions below the surface of a film, active interface states may well be deactivated by the appropriate doping.

References

(1) Anderson, R.L. (1960). I.B.M. J. Res. Development, 4, 283

(2) Aven, M. and Prener, J.S. (1967). 'Physics and Chemistry of II-VI Compounds'. North-Holland

(3) Barry, R.W., Ha-l, P.M., and Harris, M.T. (1968). 'Thin Film Technology', D. Van Nostrand Co. Inc.

(4) Bube, R.H. (1960). 'Photoconductivity in Solids'. J. Wiley and Sons

(5) Chan, D.S.H., and Hill, A.E. (1976). Thin Solid Films, 35, 337-349

(6) Cheah, K.W. (1976). M.Sc. Reports, London University

(7) Chopra, K.L., Bobb, L.C., and Francombe, M.H. (1963). J. Appl. Physics, 34, 6

(8) Chynoweth, A.G., Feldmann, W.L. and Logan, R.A. (1961). Phy. Rev., 121, 3

(9) Classen, R.S. (1961). J. Appl. Physics, 32, 2372

(10) Crookes, W. (1891). Proc. Roy. Soc. London, 50, 88

(11) Cserveny, S.I. (1968). Int. J. Electron. 25, 65

(12) De Noble, D. (1959). Philips Res. Rep., 14, 361-430

(13) Denton, G.A., Friedman, G.M., and Schetzina, J.F. (1975) J. Appl. Physics, 46, 7

(14) Dolega, W. (1963). Z. Naturforch, 18, 653

(15) Donnely, J.P. and Milnes, A.G. (1967). I.E.E. Trans. Electrons Devices, ED-14, 63

(16) Francombe, M.H. (1963). 10th Trans. Nat. Vac. Symp. America Vac. Soc., 316

(17) Garlick, G.F. and Gibson, A.F. (1948). Proc. of Phys. Soc. of London, 60

(18) Glew, R.W. (1977). Thin Solid Films, 46, 1

(19) Hampshire, M.J. (1975). Phys. Stat. Sol., 27, 247

(20) Hipwood, L.P. (1977). Ph.D. Thesis, London University

(21) Holt, D.B. (1966). J. Phys. Chem. Solids, 27, 1053

(22) Holt, D.B. (1974). Thin Solid Films, 24, 1-53

(23) Jakubowskî, A. (1976). Bulletin de L'Academie, Polonaise de Sciences, Série des Science Technique, vol. xxiv, numéro 6

(24) Jerhot, J. and Śnejdar (1970). Czech J. Phys. B20

(25) Jerhot, J. and Śnejdar, V. Thin Solid Films, 26, 1, 329

(26) Many, A., Goldstein, Y., and Grover, N.B. (1965). 'Semiconductor Surfaces', Nth-Holland

(27) Mataré, H.F. 'Defect Electronics in Semiconductors'. Wiley-Interscience, 1971

(28) Mott, N.F. (1967). Adv. in Phys., 16, 49

(29) Pashinkin, A.S. et al. (1962). Sov. Phys. - Cryst., 7, 247

(30) Pawlewicz, W.T., Allen, R.P., Barrus, H.G., and Laegrerd, N. (1976). Int. Symp. on CdTe Phys. Prop. and Appl.

(31) Perlman, S.S. (1964). Advan. Energy Convers., 4, 184

(32) Perlman, S.S. and Feucht, D.L. (1964). Solid State Electronics, 7, 911-923

(33) Price, P.J. (1962). Int. Conf. Phys. Semicond., Exeter, 99

(34) Politt, K.R., Robb, J.C., and Thomas, D.W. (1978). Nature, 272

(35) Ray, B. 'II-VI Compounds'. (1969) Pergamon Press

(36) Rediker, R.H., Stopek, S., and Ward, J.H. (1964). Sol. St. Elec., 7, 621-629

(37) Riben, A.R., and Feucht, D.L. (1966)
(a) Sol. St. Elec., 9, 1055-65
(b) Int. J. Elec. 20, 6, 583-599

(38) Rybka, V., Krajčí, P., and Švcík, Z. (1975), Phys. Sta. Sol., (a), 28, 455

(39) Sadek, S. (1975). Ph.D. Thesis, London University

(40) Simmons, J.G., and Taylor, G.W. (1974). Sol. St. Elec., 17, 125-130

(41) Stark, F. (1909). Z. Electrochem., 15, 509-512

(42) Tansley, T.L. Phys.
(1966) (a) Phys. Sta. Sol., 18, 105
(1971 I) (b) Proc. Int. Conf. on the Phys. and Chem. of Semicon. Heterojunctions, vol. II
(1971 II) (c) 'Semiconductors and Semimetals', vol. 7A

(43) Van Ruyven, L.J.
(1964) Phys. Sta. Sol., 5, K109
(1972) Ann. Rev. Nat. Sci., vol. 2, 501

(44) Van Ruyven, L.J., and Williams, F.F. (1967). Am. J. Phys., 35, 705-709

(45) Vossen, J.L. (1971). R.C.A. Rev., 32

(46) Walsh, P.J., Hall, J.E., Nicolaides, R. et al. (1970). J. Non-Crystalline Solids, 2, 197

(47) Gummel, H.K., and Scharfetter, D.L. (1967). J. App. Phys. 38, 2148

(48) Milnes, A.G., and Feucht, D.L. (1972). ' Hetrojunctions and Metal-Semiconductor Junctions' Academic Press.

(49) Newman, P.C. (1965). Elect. Letts., 1, 265.